



HAL
open science

Effect of microstructure on the formability of β titanium alloys

Cai Hu

► **To cite this version:**

Cai Hu. Effect of microstructure on the formability of β titanium alloys. Materials. INSA de Rennes, 2021. English. NNT : 2021ISAR0022 . tel-04457259

HAL Id: tel-04457259

<https://theses.hal.science/tel-04457259>

Submitted on 14 Feb 2024

HAL is a multi-disciplinary open access archive for the deposit and dissemination of scientific research documents, whether they are published or not. The documents may come from teaching and research institutions in France or abroad, or from public or private research centers.

L'archive ouverte pluridisciplinaire **HAL**, est destinée au dépôt et à la diffusion de documents scientifiques de niveau recherche, publiés ou non, émanant des établissements d'enseignement et de recherche français ou étrangers, des laboratoires publics ou privés.

THESE DE DOCTORAT DE

L'INSTITUT NATIONAL DES SCIENCES
APPLIQUEES RENNES

ECOLE DOCTORALE N° 602
Sciences pour l'Ingénieur
Spécialité : Génie Mécanique

Par

Cai HU

Effect of microstructure on the formability of β titanium alloys

Thèse présentée et soutenue à Rennes, le « 23/11/2021 »
Unité de recherche : Laboratoire de Génie Civil et Génie Mécanique
Thèse N° : 21ISAR 27 / D21 - 27

Rapporteurs avant soutenance :

Pascale BALLAND Professeur des Universités, Université Savoie Mont Blanc
Franck TANCRET Professeur des Universités, Université de Nantes

Composition du Jury :

Président :	Hervé LAURENT	Professeur des Universités, Université Bretagne Sud
Examineurs :	Pascale BALLAND	Professeur des Universités, Université Savoie Mont Blanc
	Franck TANCRET	Professeur des Universités, Université de Nantes
	Laurence MOREAU	Maître de Conférences, Université de Technologie de Troyes
	Hervé LAURENT	Professeur des Universités, Université Bretagne Sud
	Philippe CASTANY	Maître de Conférences, INSA Rennes
Dir. de thèse :	Lionel LEOTOING	Maître de Conférences, INSA Rennes

DOCTORAT
BRETAGNE SCIENCES
LOIRE POUR L'INGENIEUR

INSA | INSTITUT NATIONAL
DES SCIENCES
APPLIQUÉES
RENNES

Effect of microstructure on the formability of β titanium alloys

HU Cai



Collaborated with



Funded by



To my parents

To all my friends

To my future wife

Acknowledgements

I would like to express my deep and sincere gratitude to all my supervisors: Lionel LEOTOING, Philippe CASTANY, Dominiques GUINES and Thierry GLORANT. Thanks to the help of Lionel and Dominiques on the Marciniak tests, simulation. Thanks to Philippe for SEM, EBSD, and the preparation of specimens. Thanks to Thierry for allowing me to do research and providing invaluable guidance throughout this work. Thanks to all of you for the discussions, review and modification of all my drafts, pointing out the mistakes I made during my research with your profound knowledge, vision, sincerity, and patience, which have deeply inspired me. It is my great honor to work and study under your supervision.

The reporters of my PhD defense Pascale BALLAND, Franck TANCRET gave me a lot of professional suggestions on my thesis. Other members of the jury Hervé LAURENT, Laurence MOREAU also shared ideas about my work with me. Thanks for the appreciation for my PhD work from all of you.

I would like to thank all the professors, lecturers, technicians, colleagues, etc. at INSA Rennes who helped me in many aspects. You also contribute to this work. Thanks to Dominique FOURE for improving my french. Thanks to Aurore GOUIN and Justine GROMAIRE for helping with administrative affairs. Thanks to Amelie FILON for the course I took. Thanks to Thierry COZIC for solving computer problems. Abir Abdelkefi, Alaa Kobeissi, Jiabin LIANG, Marwan JORA and Zhihao WANG also gave me a lot of help on my PhD work.

I would also like to say thanks to all my friends for their kind support and care, not only in academics but also in life. Because of you that I have experienced a wonderful time during my residence in France.

I am extremely thankful to my parents for giving birth to me. Their unconditional love, caring and immense sacrifices for educating me for my future.

Finally, I would like to thank the financial support from China Scholarship Council (CSC).

Résumé

Les alliages de titane sont utilisés dans différents secteurs industriels, notamment dans l'aéronautique et le biomédical. Leur utilisation croissante est principalement due à des caractéristiques mécaniques spécifiques élevées, une très bonne résistance à la corrosion et une bonne conservation de leurs performances à haute température. À température ambiante, les alliages de titane peuvent présenter des microstructures différentes et sont généralement classés suivant trois catégories : les alliages α (structure hexagonale compacte), les alliages β (structure cubique centrée) et les alliages $\alpha+\beta$. Les propriétés mécaniques telles que la ductilité ou encore la formabilité sont largement dépendantes de leur microstructure.

Ce travail porte sur l'étude du comportement mécanique des alliages de titane β métastables de plus en plus utilisés dans les applications aéronautiques, en remplacement des alliages de titane $\alpha+\beta$. L'objectif principal est d'étudier l'influence de la microstructure, en particulier la texture, sur la formabilité de ces matériaux. Les alliages β métastables Ti21S et Ti5553 ont été sélectionnés.

Différentes microstructures ont été obtenues en faisant varier le taux de laminage et les traitements thermiques appliqués. Une analyse de ces microstructures incluant de la fractographie, le suivi de la taille des grains et de la texture a été menée. Une caractérisation mécanique (écrouissage et formabilité) de ces différentes microstructures est tout d'abord effectuée à partir d'une campagne d'essais de traction uniaxiale.

Les résultats obtenus montrent que le taux de laminage et la précipitation α affectent la formabilité. Un modèle numérique de type Marciniak et Kuczyński (M-K) est ensuite proposé afin de prédire des courbes limites de formage complètes pour les différentes microstructures étudiées. La valeur du défaut géométrique du modèle M-K est calibrée à partir des résultats des essais de traction uniaxiale.

Une campagne expérimentale avec un dispositif de mise en forme de type Marciniak est enfin menée pour la nuance Ti21S afin de parcourir différents chemins de déformation et de discuter le caractère prédictif du modèle proposé.

Abstract

Titanium alloys are widely used in industries (aeronautics, biomedical . . .) due to their high specific mechanical characteristics, very good corrosion resistance and high temperature performances. At room temperature, titanium alloys can exhibit different microstructures and are generally classified into three categories: α alloys (hexagonal compact structure), β alloys (centered cubic structure) and $\alpha+\beta$ alloys. Mechanical properties such as ductility or formability are largely dependent on their microstructure.

This work focuses on the study of the behaviour of β metastable titanium alloys increasingly used in aeronautical applications as a replacement for $\alpha+\beta$ titanium alloys. The main objective is to study the influence of microstructure, in particular texture, on the formability of such materials. The metastable alloys Ti21S and Ti5553 are selected for this study.

Different microstructures controlled by the rolling rate and heat treatments are obtained. An analysis of these microstructures including fractography, analysis of grain size and texture is carried out. First, a mechanical characterization (hardening and formability) of these different microstructures is carried out thanks to a campaign of uniaxial tensile tests.

The results show that both the rolling ratio and the α precipitation impact the formability. A numerical model based on the Marciniak and Kuczyński (M-K) theory is proposed for the prediction of the whole forming limit curves, for the different studied microstructures. The value of the geometrical imperfection of the M-K model is calibrated from the uniaxial tensile tests.

Finally, an experimental campaign on a Marciniak-type set-up permits to follow various strain paths for the Ti21S grade and discuss the predictive character of the proposed model.

Contents

Acknowledgements	1
Résumé	3
Abstract	5
List of Figures	11
List of Tables	17
Notations	19
Introduction Générale	21
General introduction	25
1 Applications, microstructures and mechanical properties of titanium alloys	29
1.1 Introduction	31
1.2 Applications of titanium alloys in aviation industry	32
1.3 Classification of titanium alloys	35
1.3.1 Introduction of the classification	35
1.3.2 α alloys ($x \approx 0$)	35
1.3.3 Near α alloys ($0 < x < 0.3$)	36
1.3.4 $\alpha+\beta$ alloys ($0.3 < x < 1.5$)	36
1.3.5 Metastable β alloys ($1.5 < x < 3$)	36
1.3.6 β alloys ($x > 3$)	37
1.3.7 Discussion	37
1.4 Microstructure	38
1.4.1 Phases	38
1.4.2 Texture	43
1.4.3 Fractography	46
1.5 Mechanical properties of titanium alloys	48

1.5.1	Effect of heat treatment on mechanical properties	48
1.5.2	Influence of phase arrangement	51
1.5.3	Anisotropy	51
1.5.4	Anisotropic yield criterion	54
1.5.5	Hardening laws	56
1.5.6	Conclusion	57
1.6	Experimental FLC	57
1.6.1	Nakazima and Marciniak tests	58
1.6.2	Factors affecting forming limit curve	59
1.7	Predicted FLC	62
1.7.1	Models for predicting FLC	62
1.7.2	Marciniak-Kuczynski model	63
1.7.3	FLC for titanium alloys	66
1.7.4	Conclusion	66
1.8	Conclusion	68
2	Microstructure and mechanical properties	69
2.1	Introduction	71
2.2	Experimental procedure	71
2.2.1	Materials, thermomechanical treatments and tensile tests . .	71
2.2.2	EBSD	73
2.2.3	Method of plotting forming limit points	74
2.2.4	Method for calculating Lankford coefficients r	76
2.3	Microstructure of Ti21S and Ti5553 alloys	79
2.3.1	Grain size of Ti21S and Ti5553 alloys	79
2.3.2	Texture of Ti21S and Ti5553 alloys	79
2.3.3	Conclusions	84
2.4	Tensile tests of Ti21S and Ti5553 alloys	85
2.4.1	Tensile results of Ti21S and Ti5553 alloys	85
2.4.2	Forming limit points and r -values of Ti21S and Ti5553 alloys	90
2.4.3	Conclusions	92
2.5	Fracture analysis of Ti21S and Ti5553 alloys	93
2.5.1	Fractographs of Ti21S	93
2.5.2	Fractographs of Ti21S+	95
2.5.3	Fractographs of Ti5553	96
2.5.4	Conclusions	96
2.6	Conclusions	97

3	Prediction of forming limits at necking	99
3.1	Introduction	101
3.2	Numerical M-K model	101
3.2.1	Definition of the FE M-K model	101
3.2.2	Failure criterion of M-K model	102
3.2.3	Comparison of numerical and analytical predictions of forming limits from M-K model	104
3.2.4	Effect of the initial imperfection factor f_0	105
3.2.5	Identification of Ludwik's hardening law	106
3.2.6	Conclusions	107
3.3	Anisotropy characterization of Ti21S	110
3.3.1	Lankford coefficients of Ti21S 0	110
3.3.2	Anisotropy parameters of Ti21S 0	111
3.3.3	Validating the anisotropy of Ti21S 0 by simulation	111
3.4	Predicted FLCs of Ti21S, Ti21S+ and Ti5553	113
3.4.1	Methodology	113
3.4.2	Predicted FLCs of Ti21S L,0, Ti21S L, Ti21S T, Ti21S+ and Ti5553	113
3.4.3	Predicted FLCs of Ti21S L,0, Ti21S L,50 and Ti21S L,75	116
3.4.4	Conclusions	118
3.5	Conclusions	119
4	Characterization of the formability of Ti21S titanium alloy by Marciniak test	121
4.1	Introduction	123
4.2	Presentation of Marciniak test	123
4.2.1	Marciniak test device	123
4.2.2	Marciniak test specimen	124
4.2.3	Experimental validation of the Marciniak test dimensions for titanium alloys	125
4.3	Simulation and optimization of the Marciniak test	127
4.3.1	Finite element model of Marciniak test	127
4.3.2	Parametric study	130
4.3.3	Effect of fillet radius of blank holder r_b	131
4.3.4	Effect of different fillet radius of punch r_p	135
4.3.5	Effect of the shape of specimen	138
4.3.6	Effect of different thicknesses of intermediate part E_i	139
4.3.7	Conclusions	142
4.4	Marciniak test	143

4.4.1	Experimental characterization of the formability on Ti21S alloy	143
4.4.2	Difficulty of detecting the forming limit	143
4.4.3	Modified fitting method	145
4.4.4	Results of Ti21S	147
4.4.5	Discussion and conclusions	150
4.5	Conclusions	151
	Conclusions et Perspectives	152
	Conclusions and Perspectives	154
	Appendix	157
	Bibliography	161

List of Figures

1.1	The cost index of some common structure materials	31
1.2	Applications of titanium in U.S	32
1.3	Application of Ti21S in the nozzle area of Boeing 777	33
1.4	Ti5553 alloy in the Boeing 787 main landing gear	34
1.5	Superplastically formed TA6V engine nacelle component for the Boeing 757 from a single sheet	34
1.6	Three-dimensional phase diagram of Ti alloys	36
1.7	The comparison of mechanical properties of $\alpha+\beta$ titanium alloy and β titanium alloy	37
1.8	Different heat treatments according to the temperature in the phase diagram of $\alpha+\beta$ alloys and metastable β titanium alloys	38
1.9	TTT diagram of Ti21S	39
1.10	Processing route of Ti21S	39
1.11	SEM microstructure of Ti21S	40
1.12	Tensile true-stress-true-strain curves for the solution treated and the precipitated microstructures	41
1.13	TTT diagram of Ti5553	41
1.14	Microstructures of Ti5553	42
1.15	Tensile curves of Ti5553 with pure β phase, $\alpha+\beta$ phases and TA6V	43
1.16	Stereographic projection of orientation relationship from β to α transformation	44
1.17	Main rolling texture fiber of bcc materials in ODF	44
1.18	ODF of the section $\varphi_2=45^\circ$ with a strong γ fiber	45
1.19	Young's modulus parallel to the tensile axis of single crystal in 28 orientations obtained from both considered β -phase single crystal elastic constants	46
1.20	Fracture surfaces of Ti5553 of powder metallurgy (PM) and ingot metallurgy (IM)	47
1.21	Fracture surfaces of Ti5553 after solution treated at 830°C plus aged at 520°C	48
1.22	Processing routes HT1 and HT2 on Ti5553 alloys	50

1.23	Tensile curves of Ti5553 and Ti-12Nb alloy under HT1 and HT2 treatment	50
1.24	Effect of texture on the anisotropy of Young's modulus in Ti-6Al-4V alloys	52
1.25	Effect of tensile directions on the anisotropy of yield strength and ductility RA in Ti-6Al-4V alloys	53
1.26	Effect of r-value on the yield surface	53
1.27	The influence of texture and r-value on the necking and fracture behaviour on tensile test by using TA6V	55
1.28	Edge cracking on the radius	57
1.29	Four points to detect forming limit curves	58
1.30	Nakazima and Marciniak tests	59
1.31	Forming limit curves by different testing methods	60
1.32	Strain paths from different methods	60
1.33	Influence of strain path on the forming limit curve	61
1.34	Influence of temperature on the forming limit curve	61
1.35	Influence of punch speed on the forming limit curve	62
1.36	The classification of theoretical models for predicting forming limit curves	63
1.37	Representation of the M-K model	64
1.38	Predicted FLC for Ti-6Al-4V for different strain rates from theoretical M-K model	66
1.39	Comparison of predicted FLC from M-K model and the Marciniak test results for TNW700 titanium alloy	67
1.40	Experimental results of FLC for several titanium alloys	67
2.1	Tensile specimen	72
2.2	Mechanical and heat treatment applied to Ti21S and Ti5553 alloys	73
2.3	Specimen geometries and the corresponding strain paths of FLC . .	75
2.4	Detecting forming limit strain from ISO 12004-2	76
2.5	Comparison of limit points from ISO 12004-2 and modified method proposed by Chu	77
2.6	Position of the five selected points on the specimen Ti21S L,0 . . .	77
2.7	Strain range of 50%-75% of maximum strain for the specimen Ti21S L,0-1	78
2.8	Evolution of ε_2 and ε_3 of the 5 points chosen on specimen Ti21S L,0 and its averaged strain evolution curve	78
2.9	EBSD IPF maps of Ti21S and Ti5553 alloys (X direction is along rolling direction)	80
2.10	Distribution of grains diameter of Ti21S alloy	81

2.11	Distribution of grains diameter of Ti5553 alloy	81
2.12	Inverse pole figure of Ti21S (a) 0% reduction rate, (b) 50% reduction rate, (c) 75% reduction rate (X0 corresponds to the rolling direction)	82
2.13	Inverse pole figure of Ti5553 (a) 0% reduction rate, (b) 50% reduction rate, (c) 75% reduction rate (X0 corresponds to the rolling direction)	83
2.14	$\varphi_2=45^\circ$ section of ODF of Ti21S (a) 0% reduction rate, (b) 50% reduction rate, (c) 75% reduction rate	84
2.15	$\varphi_2=45^\circ$ section of ODF of Ti5553 (a) 0% reduction rate, (b) 50% reduction rate, (c) 75% reduction rate	85
2.16	Comparison of tensile curves of Ti21S alloys: (a) L direction, (b) T direction	86
2.17	Comparison of tensile curves of Ti21S 0 and Ti21S+ 0: (a) L direction, (b) T direction	87
2.18	Comparison of tensile curve of Ti5553 alloys: (a) L direction, (b) T direction	88
2.19	Average forming limit points and r -values for Ti21S and Ti5553 alloys	91
2.20	Ti21S 0 SEM images	93
2.21	Ti21S 50 SEM images	94
2.22	Ti21S 75 SEM images	94
2.23	Ti21S+ 0 SEM images	95
2.24	Ti5553 SEM images	96
3.1	(a) M-K analytical model and (b) 1/8 of the M-K model and its dimensions	101
3.2	Finite element model of the M-K model	102
3.3	Identify the necking of Ti21S L,0	103
3.4	The effect of different critical increment ratios on predicted FLC of aluminium alloy AA6111-T4	103
3.5	Validation of finite element model by comparing numerical and analytical results	105
3.6	Effect of different initial imperfection f_0 on predicted forming limit curve of AA6056 aluminium alloy	106
3.7	Definition of fitting zone	107
3.8	The fitting of Ti21S L,0, Ti21S+ L,0 and Ti5553 L,0	108
3.9	The fitting of Ti21S L,0, Ti21S L,50 and Ti21S L,75	109
3.10	r -value of Ti21S 0	110
3.11	Finite model for validation r -value of Ti21S 0	111
3.12	Method of calculating r -value in simulation	112
3.13	Comparison of the r -value of Ti21S 0 from simulation and experiment	112

3.14	Schematic of plotting the whole FLC by using different S values . . .	114
3.15	Comparison of experimental point and predicted FLC assuming (a) isotropic Ti21S, (b) anisotropic Ti21S L and Ti21S T	115
3.16	Comparison of experimental point and predicted FLC of (a) Ti21S+, (b) Ti5553	117
3.17	Comparison of experimental point and predicted FLC of Ti21S L,0, Ti21S L,50 and Ti21S L,75	118
4.1	Marciniak test device	124
4.2	Dimensions (in mm) of Marciniak device	124
4.3	Dimensions of Marciniak test specimen with three thicknesses (0.8mm, 1.5mm and 2mm)	125
4.4	Specimen painted with a speckle pattern	126
4.5	Forming limit curve and the corresponding specimen of Marciniak test	126
4.6	Uniaxial and plane strain TA6V specimens before and after Marciniak tests	126
4.7	Marciniak test parts of the model	127
4.8	Three thickness zones and mesh of Marciniak specimen	128
4.9	Plastic strain - stress curves of TA6V and Ti40	128
4.10	Mises stress distribution on the TA6V specimen when the maximum reaches 1131 MPa	129
4.11	Mises stress distribution on the specimen Ti40 when the maximum reaches 627 MPa	130
4.12	Definition of center (C), bending center (B,c) and bending edge (B,e)	131
4.13	Distribution of Mises stress for Ti40 uniaxial specimens with different fillet radius of blank holder r_b	132
4.14	Evolution of the equivalent plastic strain (PEEQ) with different fillet radius of blank holder r_b . Red vertical line indicates the punch displacement when the maximum Mises stress is reached	133
4.15	Effect of the fillet radius of blank holder on the G value	134
4.16	Distribution of Mises stress for Ti40 uniaxial specimens with different fillet radius of punch r_p	136
4.17	Evolution of equivalent plastic strain (PEEQ) with different fillet radius of punch r_p . Red vertical line indicates the punch displacement when the maximum Mises stress is reached	137
4.18	Effect of the fillet radius of punch on the G value	138
4.19	Section of the new specimen shape with curved surface	138
4.20	Distribution of Mises stress for Ti40 uniaxial specimens with curved surface	139

4.21	Distribution of Mises stress for Ti40 uniaxial specimens with different thicknesses of intermediate part E_i	140
4.22	Evolution of the equivalent plastic strain (PEEQ) with different thicknesses of intermediate part E_i . Red vertical line indicates the punch displacement when the maximum Mises stress is reached . . .	141
4.23	Effect of intermediate thickness on the G value	142
4.24	Marciniak specimens of Ti21S	144
4.25	Section and the fitting on the Marciniak specimen 3u	145
4.26	Comparison of the standard fitting curve fitted with the specimens which have high level strain distribution and low level strain distribution along the section	146
4.27	Distribution of major strain after Marciniak test (specimen 3u) and its fitting curve with the modified method	147
4.28	Marciniak test results of all experimental points on Ti21S	148
4.29	Comparison between the predicted FLC and all the points on Ti21S	148
4.30	Marciniak test of Ti21S uniaxial specimen and its strain path . . .	149
4.31	Marciniak test of Ti21S plane strain specimen and its strain path .	149
4.32	Marciniak test of Ti21S equibiaxial specimen and its strain path . .	150
4.33	ODF of Ti21S 0	157
4.34	ODF of Ti21S 50	158
4.35	ODF of Ti21S 75	158
4.36	ODF of Ti5553 0	159
4.37	ODF of Ti5553 50	159
4.38	ODF of Ti5553 75	160

List of Tables

1.1	Application of specific titanium alloys in selected parts of aviation industry	33
1.2	Mechanical properties of Ti5553	42
1.3	The phases, heat treatment and yield strength of some β titanium alloys	49
1.4	Tensile properties of Ti5553	50
1.5	Predicted plastic anisotropy by textures	54
1.6	Hardening laws of metallic materials	56
2.1	Definition of parameters in detecting limit strain	75
2.2	Statistics of average grain size and standard deviation of Ti21S and Ti5553 alloys	79
2.3	Mechanical properties of Ti21S and Ti5553 alloys (1 of 2)	89
2.4	Mechanical properties of Ti21S and Ti5553 alloys (2 of 2)	90
3.1	Fitting parameters by Ludwik's law	107
3.2	Fitting parameters by Ludwik's law of Ti21S with different rolling reduction rates	110
3.3	Anisotropy parameters of Ti21S 0	111
3.4	Properties of the materials used in simulation of isotropic Ti21S L,0, anisotropic Ti21S L, anisotropic Ti21S T, Ti21S+ and Ti5553 .	114
3.5	Minimum S value and imperfection f_0 used in predicted FLC of isotropic Ti21S L, anisotropic Ti21S L, anisotropic Ti21S T, Ti21S+ and Ti5553	116
3.6	Properties of the materials used in simulation of Ti21S L,0, Ti21S L,50 and Ti21S L,75	116
3.7	Minimum S value and imperfection value f_0 used in predicted FLC of Ti21S alloys with different reduction rate	118
4.1	Dimensions of Marciniak specimens	125
4.2	Ultimate tensile strength (UTS), Young's modulus (E) and Poisson ratio (ν)	129

4.3	G value and displacement of the punch (H) when ultimate tensile strength is reached with different fillet radius of blank holder r_b . . .	134
4.4	G value and displacement of the punch (H) when ultimate tensile strength is reached with different fillet radius of punch r_p	135
4.5	G value and displacement of the punch (H) when ultimate tensile strength are reached with different thicknesses of intermediate part E_i	142

Notations

DIC	Digital Image Correlation
FLC	Forming Limit Curve
FLD	Forming Limit Diagram
M-K	Marciniak and Kuczynski
SPF	Superplastic forming
YS	Yield strength
UTS	Ultimate tensile strength
E	Young's modulus
A	Elongation
x	Ratio of equivalent molybdenum $[Mo]_{eq}(\%)$ and equivalent aluminium $[Al]_{eq}(\%)$
d	Interparticle spacing of α phase
r	Lankford coefficients
σ_{ij}	Stress components
F, G, H, L, M, N	Constants related to the component of the stresses in Hill48 criterion
R_{ij}	Anisotropy parameters
r_{θ}	Lankford coefficients with the angle θ to the rolling direction.
$\bar{\sigma}$	Equivalent stress
$\bar{\epsilon}$	Equivalent strain
$\bar{\epsilon}_p$	Equivalent plastic strain
n	Strain hardening coefficient
K, K_1, K_2	Strength coefficient

A, B, C	Material parameters in hardening laws
σ_0	Initial yield stress
ε_0	Initial strain
f_0	Imperfection factor in M-K model
e_0^a, e_0^b	Thickness of the sheet corresponding to the homogeneous region (zone a) and the region of the groove (zone b)
$\Delta\varepsilon_{ij}^k$	Strain component increment
$\Delta\bar{\varepsilon}_p^k$	Equivalent plastic strain increment
W_l, W_r	Width of left fit window (W_l) and right fit window (W_r)
φ_2	One of the Euler angle
u, v	Displacement along the longitudinal direction u and transversal direction v of the numerical M-K model
S	Ratio of displacement in two different directions (v/u)
σ_m	Maximum true stress
ε_m	Plastic strain when the stress reaches its maximum value σ_m
R, R_m, R_e, R_c	Radius of the machining on the specimen
W	Width of the Marciniak specimen
r_p, r_b	Fillet radius of punch (r_p), Fillet radius of blank holder (r_b)
H	Displacement of the punch in simulation
E_c, E_i, E_m	Thickness in the center, intermediate and clamping part corresponding
ν	Poisson ratio
$\bar{\varepsilon}_c$	Equivalent plastic strain in the center part of the Marciniak specimen
$\bar{\varepsilon}_{B,c}$	Equivalent plastic strain in the bending center of the Marciniak specimen
$\bar{\varepsilon}_{B,e}$	Equivalent plastic strain in the bending edge of the Marciniak specimen
a, b, c, d	Constants in fitting equations

Introduction Générale

De nombreuses propriétés intrinsèques sont à l'origine d'une utilisation performante des alliages de titane pour diverses applications. Dans l'industrie aéronautique, leurs caractéristiques mécaniques spécifiques élevées, à la fois pour la résistance et la rigidité, sont des atouts considérables lorsque des réductions de masse sont requises. Les procédés de mise en forme des tôles métalliques sont très répandus pour la production de composants divers. La faible formabilité de certains matériaux, comme pour certains alliages de titane à température ambiante, peut limiter leur utilisation. Les alliages de titane présentent différentes microstructures suivant la taille et l'agencement des deux phases α et β . La microstructure affecte les propriétés mécaniques des tôles et notamment la formabilité pour les alliages de titane. Sous certaines conditions, les alliages β peuvent présenter une bonne formabilité qui peut diminuer après vieillissement en raison de la précipitation de la phase α qui améliore la résistance mécanique au détriment de la ductilité.

Afin d'optimiser les paramètres des procédés de mise en forme, des outils de prédiction des limites de formabilité doivent être définis. Ces outils nécessitent une bonne connaissance du comportement rhéologique des matériaux. Compte tenu du lien existant entre la microstructure et le comportement mécanique des alliages de titane, il est indispensable d'évaluer et d'optimiser la contribution de la microstructure sur l'aptitude du matériau à supporter des niveaux de déformation élevés. Peu d'études existent dans la littérature scientifique concernant la caractérisation de la formabilité des alliages de titane et l'effet de la microstructure n'est jamais quantifié.

Le Diagramme Limite de Formage (DLF) est l'outil habituellement utilisé pour évaluer la formabilité des tôles métalliques. Malgré quelques inconvénients, cet outil reste très répandu compte tenu de sa simplicité d'utilisation. Il a fait l'objet de nombreux travaux scientifiques, dans le cadre d'approches expérimentales, analytiques ou numériques. Un grand nombre d'outils prédictifs a été proposé pour tracer des Courbes Limites de Formage (CLFs). Ces CLFs doivent couvrir une

large plage d'états de déformation. La plupart de ces outils sont basés sur la théorie de Marciniak et Kuczynski (M-K). Cette approche suppose la présence initiale d'un défaut géométrique, responsable de l'apparition d'une striction. Les principales difficultés liées à la mise en œuvre de cette approche restent la calibration du défaut géométrique et la modélisation du comportement mécanique du matériau (écrouissage, anisotropie, ...). L'utilisation de la théorie M-K pour prédire les CLFs des alliages de titane reste très limitée dans la littérature.

Les tests de mise en forme de type Nakazima et Marciniak sont classiquement utilisés pour la détermination des CLFs expérimentales des tôles métalliques. Cependant, cette procédure de caractérisation est très longue et nécessite la mise à disposition de nombreuses éprouvettes de forme différente afin de suivre plusieurs chemins de déformation. Pour ces raisons, beaucoup d'efforts sont consacrés à la mise en œuvre d'outils prédictifs fiables des limites de formabilité. Ainsi, le recours aux caractérisations expérimentales n'est pas systématique pour construire des DLF mais il reste indispensable pour évaluer le potentiel des outils prédictifs pour les nouveaux matériaux. Le principal objectif de ce travail consiste à étudier l'effet de la microstructure sur la formabilité des alliages de titane β métastables qui sont de plus en plus utilisés pour des applications aéronautiques, en remplacement des alliages $\alpha+\beta$ classiques. Cette étude s'appuie sur un travail expérimental réalisé à partir d'essais conventionnels de traction et de mise en forme pour deux alliages de titane de type β et disponibles sous différentes microstructures : le Ti21S et le Ti5553. Une modélisation numérique du modèle M-K est proposée afin d'effectuer une comparaison de limites de formabilité prédites et obtenues expérimentalement.

Dans le premier chapitre, une revue bibliographique est proposée. Après une présentation succincte des principales applications et de la classification des alliages de titane, un point est réalisé sur la microstructure et sur les propriétés mécaniques macroscopiques de ces alliages. La dernière partie de ce chapitre est consacrée à la caractérisation expérimentale et à la prédiction des CLFs, avec un focus sur les alliages de titane.

Le chapitre 2 est consacré à la présentation des résultats de caractérisation de la microstructure et des propriétés mécaniques des alliages Ti21S et Ti5553. Différentes microstructures sont obtenues en modifiant la microstructure d'origine par laminage à froid avec des taux de réduction de 0%, 50% et 75% en épaisseur du matériau brut de réception, suivi d'un traitement de mise en solution. Une analyse EBSD (Electron Back Scattered Diffraction/Diffraction d'électrons rétrodiffusés) est effectuée pour étudier la taille des grains et les textures pour chaque condition. Des essais de traction conventionnels sont réalisés pour toutes les conditions afin de caractériser les différents comportements élastoplastiques ainsi que

les déformations limites associées à un état de traction uniaxiale. La méthode de corrélation d'images (DIC: digital image correlation) est employée pour calculer les champs de déformation sur la surface des éprouvettes. Suivant la microstructure, différentes valeurs de limites de formabilité sont mesurées. L'analyse des faciès de rupture par microscopie (SEM: scanning electron microscope) à la fin du chapitre fournit des éléments complémentaires quant au lien existant entre formabilité et microstructure.

Dans le chapitre 3, un modèle prédictif numérique des limites de formabilité est proposé. Il est basé sur la modélisation par la méthode des éléments finis du modèle M-K. Les différents comportements élastoplastiques identifiés à partir des résultats des essais de traction sont implémentés dans les simulations. La valeur du défaut géométrique est également calibrée à partir des essais uniaxiaux. Le caractère anisotrope de l'alliage Ti21S est évalué et son influence sur la prédiction des limites de formage est discutée.

Le chapitre 4 présente les résultats expérimentaux obtenus pour le Ti21S à partir d'un dispositif d'essai de type Marciniak. Au préalable, une optimisation de certaines dimensions du dispositif est réalisée afin de maximiser les chances d'observation de la striction et de la rupture dans la zone d'étude des éprouvettes. Compte tenu de la faible ductilité des alliages étudiés, cette précaution s'est avérée essentielle. Une comparaison entre des CLFs prédites et expérimentales est réalisée à la fin du chapitre afin de discuter la validité de l'outil prédictif.

General introduction

Titanium alloys find a wide range of uses due to the combination of very favourable characteristics. In aeronautical industry, their high specific mechanical properties (strength and stiffness) are strong assets for mass reduction requirements. Sheet metal forming processes are very common for the manufacturing of diverse components. The low formability of some materials, like some titanium alloys at ambient temperature, can significantly limit their applications. Titanium alloys exhibit different microstructures by controlling the size and arrangement of the two phases α and β . The microstructure affects the mechanical properties, including the formability of the sheets made from titanium alloys. Under some conditions, β alloys can exhibit good formability which can be reduced after aging because of the precipitation of the α phase which improves the mechanical strength and decreases the ductility.

In order to optimize the forming process parameters, predictive tools for the forming limits need to be defined. These tools require a very good knowledge of the rheological behaviour of the material. Due to the link between microstructure and mechanical behaviour of titanium alloys, it is essential to evaluate and optimize the contribution of the microstructure on the ability of the material to reach high deformations. Few studies can be found in the literature concerning the characterization of formability of titanium alloys and the effect of microstructure is never quantified.

The usual tool to evaluate the sheet metal formability is the Forming Limit Diagram (FLD). Despite some disadvantages, the method remains widely used due to its simplicity and it has been the subject of extensive experimental, analytical and numerical research works. In order to plot Forming Limit Curves (FLCs) which cover a wide range of strains states, many predictive tools have been proposed. Most of them are based on the Marciniak and Kuczynski (M-K) theory. This approach assumes a pre-existing geometrical defect which induces the onset of necking. The main difficulties with the use of this method remain the calibra-

tion of the geometrical defect and the modelling of the mechanical behaviour of the material (hardening, anisotropy ...). The applications of the M-K theory to predict FLCs for titanium alloys are very seldom in the literature.

The Nakazima and Marciniak forming tests are widely used for the determination of experimental FLCs for sheet materials. However, the experimental characterization is a very time consuming procedure and requires a lot of specimens with different geometries in order to follow various strain paths. Therefore, significant efforts have been made on developing reliable predictive models for the forming limits of sheet materials. Consequently, experimental tests are not systematically used to build FLDs but they remain essential to discuss the predictive capability of the proposed tools for new materials. The objective of this work is to investigate the effect of the microstructure on the formability of metastable β titanium alloys which are increasingly used in aeronautical applications, replacing common $\alpha+\beta$ titanium alloys. This study is based on an experimental database built from conventional tensile tests and forming tests for two β titanium alloys Ti21S and Ti5553, for different microstructures. A numerical modelling of the M-K model is proposed in order to compare predictive and experimental forming limits.

In chapter 1, a bibliographical review is proposed. After a short presentation on the applications and classification of titanium alloys, a focus is made on the metallurgical microstructure and macroscopic mechanical properties of these alloys. The last part of this chapter is dedicated to the experimental characterization and prediction of FLCs, more specifically for titanium alloys.

Chapter 2 presents the results of the characterization of the microstructure and mechanical properties of Ti21S and Ti5553 alloys. Different microstructures are obtained by modifying the original microstructure by cold-rolling with reduction rates of 0%, 50% and 75% in thickness of the as-received material, followed by solution treatment. EBSD is conducted to observe the grain sizes and textures for each condition. Conventional tensile tests for all the conditions are conducted to characterize the different elastoplastic behaviours and limit strains for the strain path associated to uniaxial stretching. Digital Image Correlation (DIC) method is used to calculate the strain fields at the surface of the specimens. Different values of forming limits are measured, depending on the microstructure. The analysis of the fracture surfaces by SEM at the end of the chapter provides additional information about the link between formability and microstructure.

Chapter 3 presents a predictive numerical model of the forming limit curves based on the modelling of the M-K model with the finite element method. The elastoplastic behaviour of the different materials is identified from the results of the uniaxial tensile tests and implemented in the simulations. The value of the geometrical imperfection is also calibrated from the uniaxial tensile tests. The

anisotropic behaviour of the Ti21S alloy is characterized and its influence on the prediction of the forming limits is discussed.

Finally, the chapter 4 presents the results of experiments on Ti21S specimens with a conventional Marciniak setup. At first, an optimization of some dimensions of the Marciniak device is proposed in order to observe the onset of necking and fracture in the gauge area of the specimens. Considering the low ductility of titanium alloys, this precaution is essential. A comparison between predictive and experimental FLCs is shown at the end of this chapter in order to discuss the validity of the predictive tool.

Chapter 1

Applications, microstructures and mechanical properties of titanium alloys

1.1 Introduction

Titanium alloys have become increasingly competitive materials, because of their high strength-to-weight ratio, resistance to embrittlement at low temperature, low-thermal expansion, high corrosion resistance and heat resistance.

Titanium is widely distributed which content exceeds 0.4% of the earth's crust, and its global proven reserves are approximately 3.4 billion tons, ranking the 10th among all elements, the 4th richest structural metal.

One of the major barriers which limited its application is the price [1]. Compared to other common alloys, the price of titanium alloys is over twenty times higher than steel, over five times than aluminium and magnesium alloys. Figure 1.1 shows the comparison if we consider the different index: cost/kg, cost/dm³, cost/specific strength.

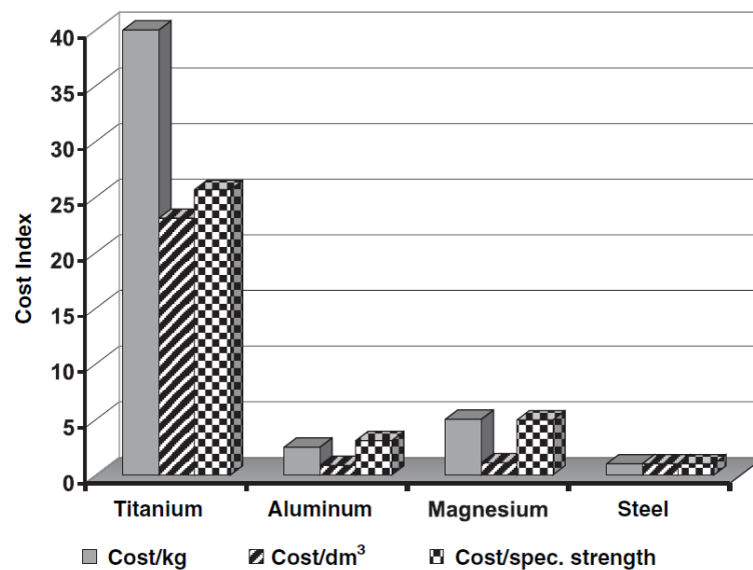


Figure 1.1: The cost index (cost/kg, cost/dm³, cost/specific strength) of some common structure materials (2003, steel=1) [1]

Titanium alloys have their importance in various fields such as aviation industry, transportation, biological technology, etc. But the application in aviation industry is the most significant. It is also attributed to the term "Light alloys" when talking about its usage in aviation industry.

This chapter proposes a general introduction to main industrial applications of titanium alloys. Then, the most frequently encountered microstructures and the associated mechanical properties are presented. Finally, a literature review on the formability of titanium alloys is presented. The experimental, theoretical and numerical methods for characterizing forming limit curves (FLCs) are introduced.

1.2 Applications of titanium alloys in aviation industry

The aviation industry consumes the largest part of titanium [2]. The applications of titanium in U.S recently are schematically showed in Figure 1.2 [3]. Almost 84% of the titanium is used in the field related to the aviation industry. Titanium alloys are widely used to reduce fuel consumption [4].

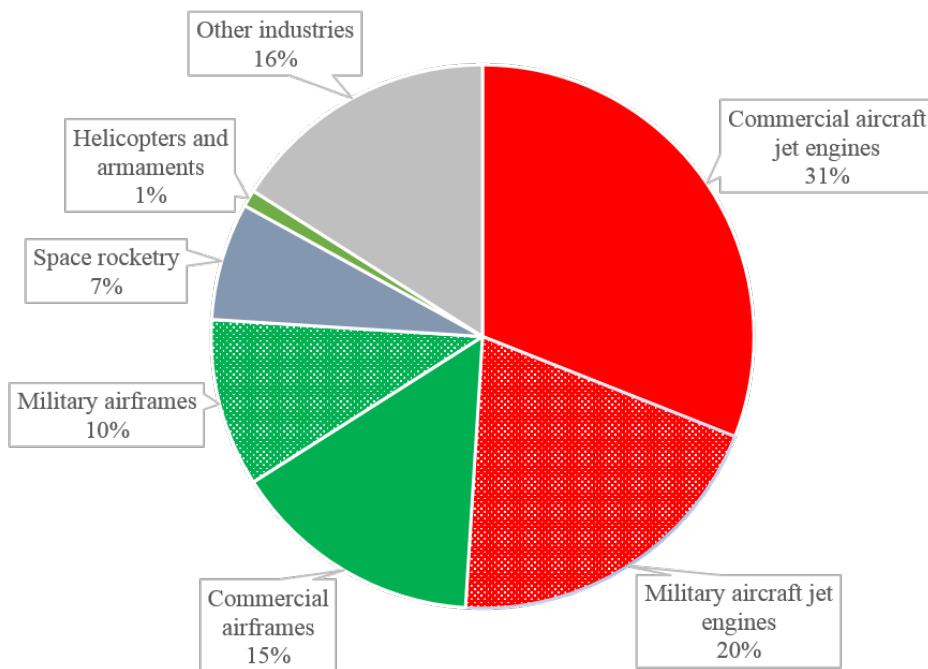


Figure 1.2: Applications of titanium in U.S [3]

Titanium alloys can be used not only in air-frame structures but also in gas turbine engines. The metastable β titanium alloys are one of the important parts used in the aviation industry due to their excellent mechanical properties, which are attributed to their microstructures [5]. It has successfully gained the attention of researchers all over the world these years. The application of specific titanium alloys in some specific parts of aviation industry is shown in Table 1.1.

Boeing Company uses Ti21S for parts of the nozzle (Figure 1.3) for better resistance to corrosion from the hydraulic fluid. This part is vulnerable due to the hydrogen embrittlement if it is made by other materials. Ti5553 alloy is used in the 787 main landing gear (Figure 1.4) [3]. Airbus A330 plans to use this material in his PW4168 engine [10]. Ti5553 is also suitable for connected components of the wing and the pylon for carrying the engine on the aircraft [11]. These materials are used because of their high fracture toughness and high resistance to fatigue.

Components in an airplane may be manufactured through casting, machining, forming, etc. Casting is used to fabricate components with very complex shapes

Table 1.1: Application of specific titanium alloys in selected parts of aviation industry

Systems and parts	Materials
Hydraulic tubing	Ti-3Al-2.5V [6]
Fan disks	Ti-6Al-2Sn-4Zr-6Mo [7]
Forgings, fasteners	Ti-5Al-5Mo-5V-3Cr; Ti-3Al-8V-6Zr-4Mo-4Zr [7]
Springs	Ti-3Al-8V-6Cr-4Mo-4Zr; Ti-15V-3Cr-3Al-3Sn [8]
Exhaust system	Ti-35V-15 Cr [7]
Wing box	Ti-6Al-4V [7]
Landing gear	Ti-10V-2Fe-3Al [9][10]; Ti-5Al-5Mo-5V-3Cr [3]
Windows frames	Ti-6Al-4V [10]
Mid-fuselage bulkhead	Ti-6Al-2Zr-2Sn-2Mo-2Cr-0.25Si [10]
Compressor stators	Ti-35V-15Cr [10]

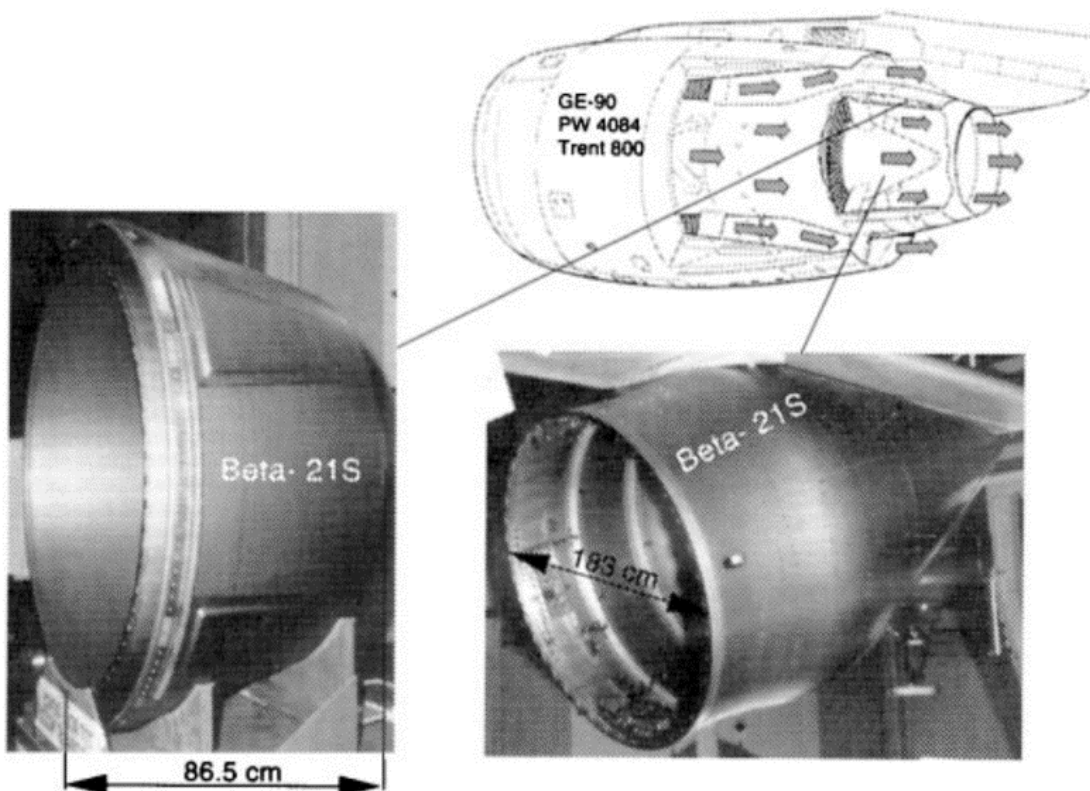


Figure 1.3: Application of Ti21S in the nozzle area of Boeing 777 [10]

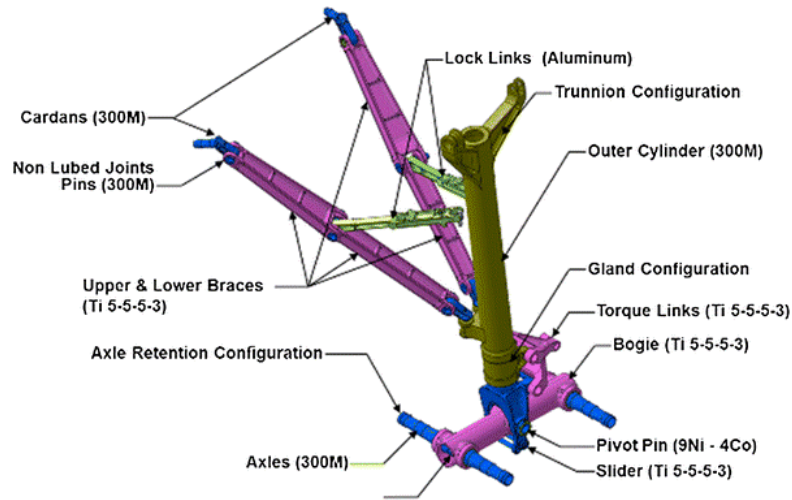


Figure 1.4: Ti5553 alloy in the Boeing 787 main landing gear [3]

and less requirement on the mechanical properties. Machining is often used for small components but it has a relatively lower utilization rate of materials. Forming is an important method for fabricating aeronautic parts. It is a near-net method that can greatly reduce the waste of materials compared to machining.

Superplastic forming (SPF) is a forming method designed for titanium with poor formability at room temperature such as TA6V. A high temperature is applied which is nearly half of the melting point ($0.5T_m$, about 900°C for titanium) [12]. However, the strain rate is very low (from 10^{-1}s^{-1} to 10^{-4}s^{-1}) and the deformation is primarily due to creep [10]. The materials can be deformed beyond their usual limit of formability with this method, approximately 200% to the tensile test. Heating not only can increase the formability of titanium alloys but also can reduce the spring back of the components after taking off the mold. However, it needs a complex heating system and device on the forming dies. The forming temperature depends on the deformation [13]. Figure 1.5 shows the application of a superplastically formed part from a single titanium sheet [14].

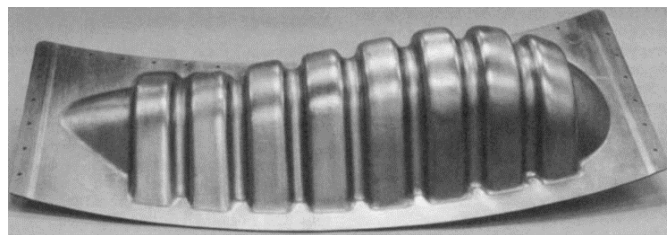


Figure 1.5: Superplastically formed TA6V engine nacelle component for the Boeing 757 from a single sheet [14]

1.3 Classification of titanium alloys

Titanium alloys can be divided into several groups according to their composition. Each group may have different microstructures obtained from different processing procedures. These microstructures may have an effect on the mechanical properties of titanium alloys. The following section will introduce the different types of titanium alloys and microstructures.

1.3.1 Introduction of the classification

Various elements can form a solid solution in titanium alloys. Some of them (Sn, Zr) are considered neutral, some (Al, O, N, C) called α stabilizers can make the α phase (Hexagonal Close Packed) more stable and increase the β transus temperature. Some (Mo, V, Nb, Ta) are isomorphous and can be in solid solution. Others (Fe, Mn, Cr, Co, Ni, Cu, etc.) are eutectoids. The last two types are β stabilizers which decrease the β transus temperature.

The effect of additional elements on the stability of β phase (Body Centred Cubic) can be translated in terms of equivalent molybdenum $[Mo]_{eq}(\text{wt.}\%)$:

$$[Mo]_{eq} = [Mo] + \frac{[V]}{1.5} + \frac{[Cr]}{0.6} + \frac{[Fe]}{0.35} + \frac{[Cu]}{1.3} + \frac{[Nb]}{3.6}$$

Aluminium is an important element for commercial titanium alloys. The percentage of Al in titanium alloys usually reaches 7% to 9%. With the same method as equivalent molybdenum, the equivalent aluminium $[Al]_{eq}(\text{wt.}\%)$ can be calculated :

$$[Al]_{eq} = [Al] + \frac{[Zr]}{6} + \frac{[Sn]}{3} + 10[O + C + 2N]$$

The ratio of these two values ($[Mo]_{eq}$, $[Al]_{eq}$) allows to distinguish the five types of titanium alloys:

$$x = \frac{[Mo]_{eq}}{[Al]_{eq}}$$

With the different functions of alloying elements, titanium alloys can be classified into α alloys, near α alloys, $\alpha+\beta$ alloys, metastable β titanium alloys and β alloys. A schematic graph of classifying titanium alloys is shown in Figure 1.6.

1.3.2 α alloys ($x \approx 0$)

α alloys are single-phase alloys, which are strengthened by the solid solution of other elements in α phase. Wear and corrosion resistance are higher than pure

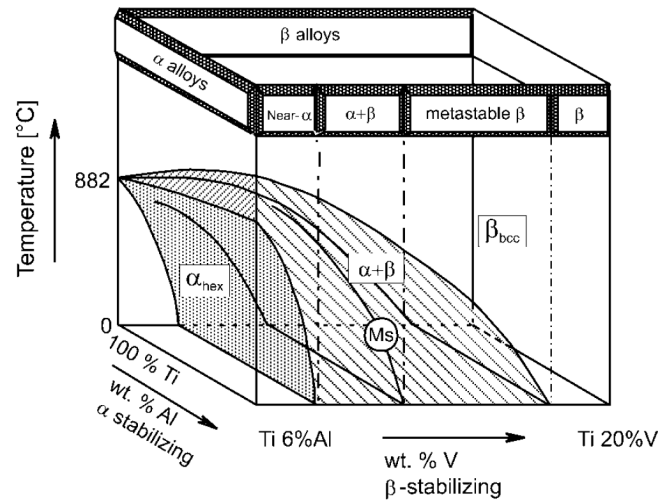


Figure 1.6: Three-dimensional phase diagram of Ti alloys (Ti-Al-V schematically, Ms: martensitic start temperature) [10]

titanium. α alloys have not cold brittleness and are suitable for use in a low-temperature environment. But the microstructure can not be modified by heat treatment. The α alloys have good creep resistance but the strength is not high at room temperature.

1.3.3 Near α alloys ($0 < x < 0.3$)

Near α alloys contain small part of β phase ($< 2\%$). Some elements are added to strengthen the alloys, without sacrificing the creep strength. The heat treatment and processing of these alloys are very similar to α alloys.

1.3.4 $\alpha + \beta$ alloys ($0.3 < x < 1.5$)

$\alpha + \beta$ alloys contain both α and β stabilizers. Various microstructures and mechanical properties can be realized through different mechanical and heat treatments. The annealed microstructure is dual-phase $\alpha + \beta$. They have a good combination of mechanical properties (high fracture toughness and fatigue strength), high strength, good heat resistance, and are heat-treatable. The most used alloys belong to this class: TA6V (Ti-6Al-4V), SP700 (Ti-4.5Al-3V-2Mo-2Fe), Ti6246 (Ti-6Al-2Sn-4Zr-6Mo).

1.3.5 Metastable β alloys ($1.5 < x < 3$)

The β phase of these so-called alloys can be retained from β solution treatment with a fast cooling rate. The strength of the solution treated condition is not very high, but they can achieve high strength through the precipitation of fine α phase

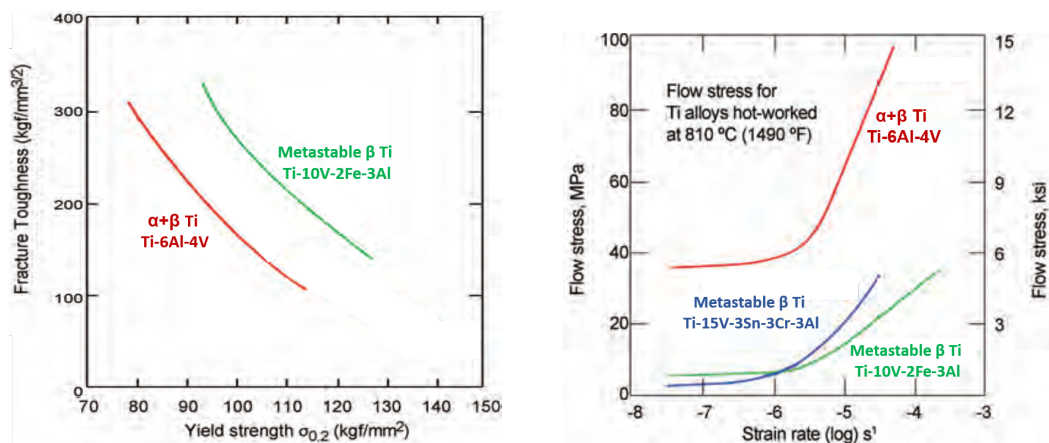
after aging. β metastable alloys show good formability in the solution treated and quenched condition, but it reduces after aging because of the participation of α phase which improves the strength and reduces the ductility [15]. They have a good combination of strength and fracture toughness [16]. Ti17 (Ti-5Al-2Sn-2Zr-4Mo-4Cr), Ti-10-2-3 (Ti-10V-2Fe-3Al), Ti21S (Ti-15Mo-3Nb-3Al-0.21Si), Ti5553 (Ti-5Al-5Mo-5V-3Cr-0.5Fe) belong to this class.

1.3.6 β alloys ($x > 3$)

β alloys contain enough β stabilizer elements like V, Mo, Nb, Fe, Cr, or Ni to get a single β phase. They can be easily deformed at a relatively low temperature. They have good corrosion resistance, high strength at room temperature, but unstable microstructure at high temperature, poor heat resistance and welding performance.

1.3.7 Discussion

The amount of α and β stabilizers decides the type of titanium alloys. Different types of titanium alloys have different characteristics of microstructures and mechanical properties. Metastable β titanium alloys can offer better fracture toughness than $\alpha+\beta$ alloys for the same level of strength. They also have better forming behavior than $\alpha+\beta$ alloys. Figure 1.7 shows these differences [12].



(a) Fracture toughness - strength figure of $\alpha+\beta$ titanium alloy and β titanium alloy (b) Flow stress - strain rate figure of $\alpha+\beta$ titanium alloy and β titanium alloy

Figure 1.7: The comparison of mechanical properties of $\alpha+\beta$ titanium alloy and β titanium alloy [12]

Considering the recently developed materials, two metastable β titanium alloys Ti21S and Ti5553 are chosen for this study. They are introduced in detail in this chapter. Their microstructures and mechanical properties are presented.

1.4 Microstructure

1.4.1 Phases

As long as metastable β titanium alloys are concerned, their microstructure can vary depending on the mechanical processing and heat treatment. The phase transformation of titanium alloys is very complex and the thermal processes are diverse, resulting in many types of microstructure. Figure 1.8 shows an example of different kinds of heat treatment according to the temperature in $\alpha+\beta$ alloys and metastable β titanium alloys [12][17]. The heat treatments for $\alpha+\beta$ alloys and for metastable β titanium alloys are different.

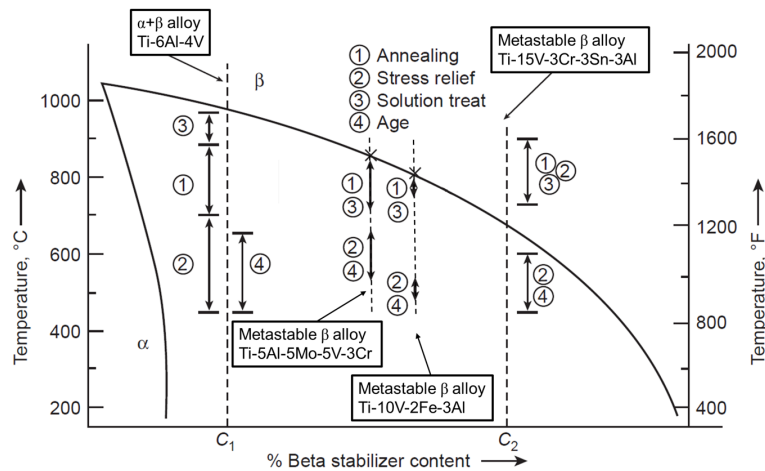


Figure 1.8: Different heat treatments according to the temperature in the phase diagram of $\alpha+\beta$ alloys and metastable β titanium alloys [17].

The commonly used heat treatment method is solution treatment, and then aging at $450 \sim 650^\circ\text{C}$. The α phase will precipitate in the original β matrix to form a fine dispersed second phase, which is a strengthening mechanism of the β alloys. The interface of α and β phases hinder the movement of dislocations, leading to high strength at room temperature. Researchers revealed that rapid solution treatment allows obtaining a small β grain size ($\sim 10 \mu\text{m}$) which can achieve the balance of ductility and strength. They also found that a slower heating rate at aging disperses α phase and makes the material reach high strength [18].

1.4.1.1 Ti21S

Ti-15Mo-3Nb-3Al-0.21Si (Ti21S) is a metastable β titanium alloy, which was introduced by TIMETAL in 1989 for its high oxidation and corrosion resistance. The molybdenum equivalent value of Ti21S is $[Mo]_{eq}(\text{Ti21S})=12.0$. Due to fine α precipitates, it can have high strength both at room temperature and at high

temperature [19][20]. It also has high creep resistance. This material is used in some aircraft engines [21] and also in missile launch canister [22].

The TTT (Time Temperature Transformation) diagram of Ti21S is shown in Figure 1.9 [23][24]. Its β transus temperature is 795–810°C. The cooling speed after solution treatment and the aging temperature is crucial to control the final microstructures. Figure shows different phases generated with different cooling rates: air cooling (AC) and air cooling + furnace cooling (FC). When the aging temperature is below 425°C, the embrittling ω phase will form. When the aging temperature is above 650°C, α phase will mainly nucleate and grow at grain boundaries [25].

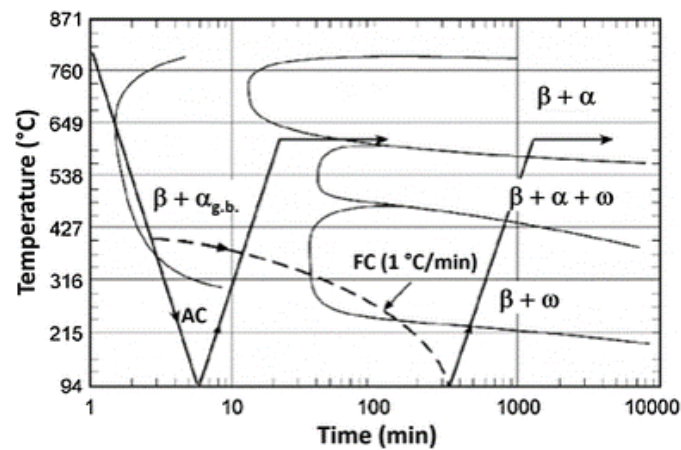


Figure 1.9: TTT diagram of Ti21S, shows the different phases evolution when air cooling (AC) + aging at 593°C and furnace cooling + aging at 593°C [23][24]

According to the TTT figure, the classical treatment of this material is homogenization, deformation (hot rolling or cold rolling), recrystallization and then aging. This processing route is shown in Figure 1.10 [26].

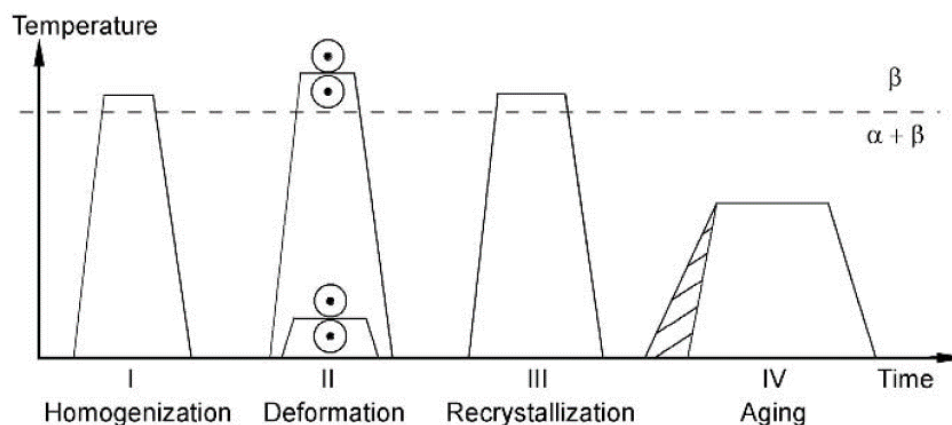


Figure 1.10: Processing route of Ti21S [26]

Mechanical treatment of 50% rolling reduction rate, followed by solution treatment at 850°C for 30 min [19] can make Ti21S alloys totally recrystallized. The α phase is soluted in the β matrix. Water quenching keeps this metastable β phase at room temperature. This condition is called solution treated state. Good formability can be achieved by this method [27].

There is an additional treatment called aging, at 593-690°C for 8 hours [23] to produce α precipitates. This is called precipitated state. The comparison of microstructures in solution treated state and precipitated state are shown in Figure 1.11 [28].

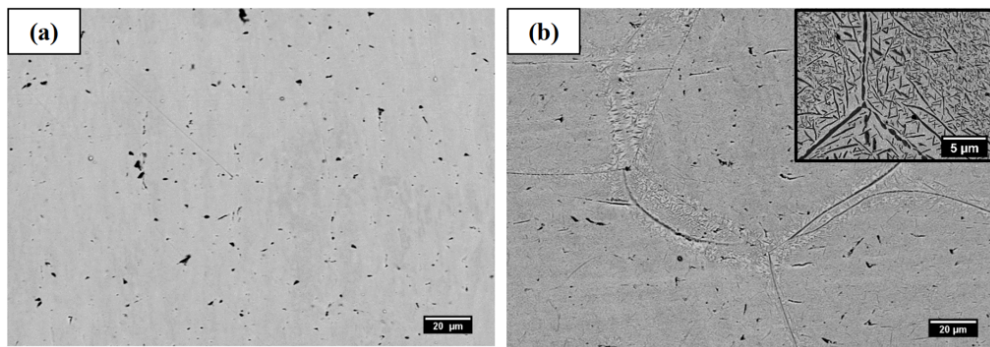


Figure 1.11: SEM microstructure of Ti21S: (a) solution treated state (b) precipitated state [28]

In the SEM figures of Ti21S, the microstructure of solution treated state is full β phase. In the precipitated state, there are fine α phase precipitates in the β matrix. The α phase is dispersed inside the grains but coarse in the grain boundaries.

Researchers studied the tensile properties of Ti21S with different microstructures. Figure 1.12 shows the true stress - true strain curves of Ti21S [28].

The red tensile curves of solution treated and precipitated in Figure 1.12 represent the tensile properties corresponding to the microstructures in Figure 1.11. From the tensile curve of solution treated state, large elongation, relatively low Young's modulus and strength are revealed. This curve also exhibits a low strain hardening rate. However, the precipitated state (precipitated) is on the contrary. High Young's modulus and strength but low elongation can be observed.

1.4.1.2 Ti5553

Ti-5Al-5V-5Mo-3Cr-0.5Fe (Ti5553) is a metastable β titanium which was introduced by VSMPO in the 1990's due to its combination of both good ductility and strength [29]. The molybdenum equivalent value of Ti5553 is $[Mo]_{eq}(Ti5553)=9.6$. Its origin alloy is Ti-5Al-4.5Mo-4.5V-1Cr-1Fe (VT22) [23][30][31].

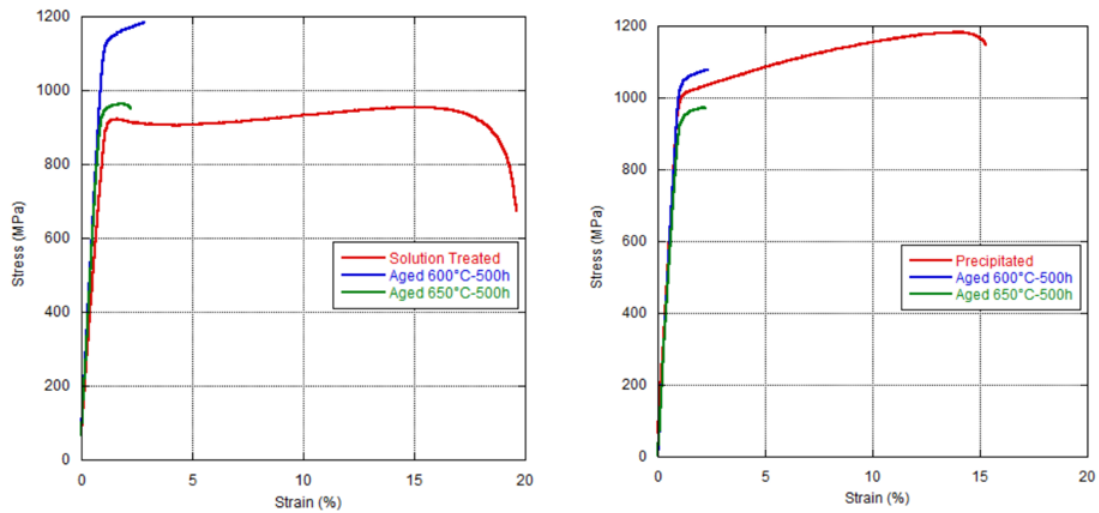


Figure 1.12: Tensile true-stress-true-strain curves for the solution treated (red curve in left figure) and the precipitated (red curve in right figure) microstructures [28]

The TTT (Time Temperature Transformation) diagram of Ti5553 is shown in Figure 1.13 [32]. The mechanism that leads to the increase in strength is related to the onset of fine-scale α precipitates nucleated from dislocations, grain boundaries, voids [30][33]. Its β transus temperature is 820–880°C.

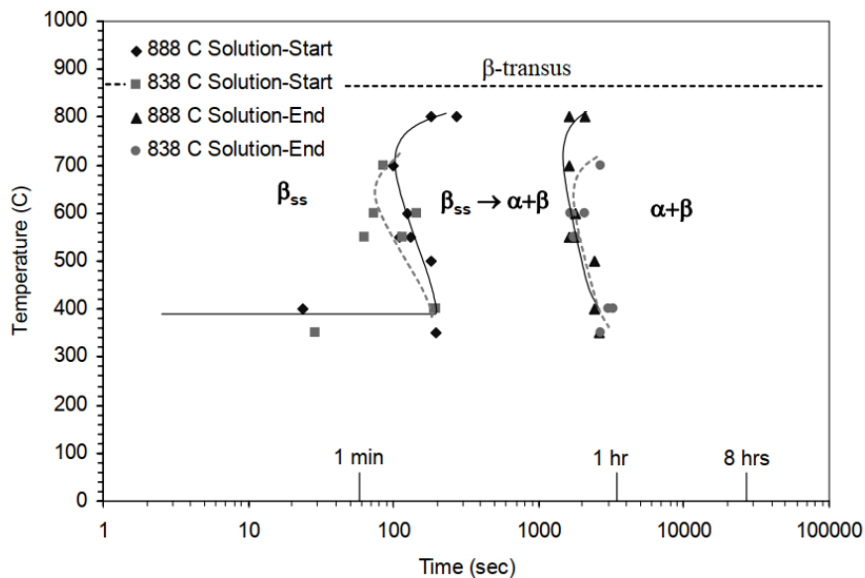


Figure 1.13: TTT diagram of Ti5553 [32]

Ti5553 alloy contains more α stabilizers than Ti21S and it can form a larger fraction of α phase, which makes its microstructures more diverse. A solution treatment just below β transus temperature after deformation and then aging will form bi-modal microstructures, which consist of equiaxed (primary) α phase in

lamellar $\alpha+\beta$ matrix. A solution treatment above β transus temperature after deformation and then aging will result in lamellar microstructures [10]. Figure 1.14 shows the comparison of the microstructure from these two procedures [32]. Ti5553 shows great microstructural temperature sensitivity [34].

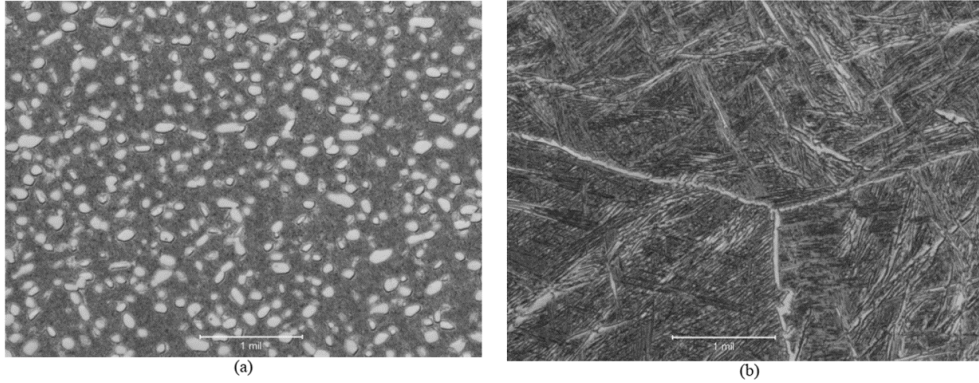


Figure 1.14: Microstructures of Ti5553: (a) bi-modal microstructure from sub-transus solution treatment, followed by aging at 540-600°C; (b) lamellar microstructure from super-transus solution treatment, followed by aging at 540-600°C [32]

Table 1.2 lists the mechanical properties of these two states [26]. The yield strength ($\sigma_{0.2}$), ultimate tensile strength (UTS) and fracture toughness (K_{IC}) are almost the same for β annealed and bi-modal microstructures, but elongation (A) of bi-modal is higher than β annealed.

Table 1.2: Mechanical properties of Ti5553 [26]

Microstructure	$\sigma_{0.2}$ (MPa)	UTS (MPa)	A (%)	K_{IC} (MPa $m^{1/2}$)
β annealed	1100	1145	6.4	66.1
bi-modal	1090	1150	13.4	65.8

The comparison of tensile curve of Ti5553 with pure β phase and with $\alpha+\beta$ phases, as well as TA6V are shown in Figure 1.15 [35]. Evident differences can be found. The Ti5553 with pure β phase from the solution treated state has good elongation and relatively low yield strength. The Ti5553 with $\alpha+\beta$ phases in the figure is obtained from the solution treatment + aging. This phenomenon also can be explained by the effect of α precipitation, which is the same in Ti21S.

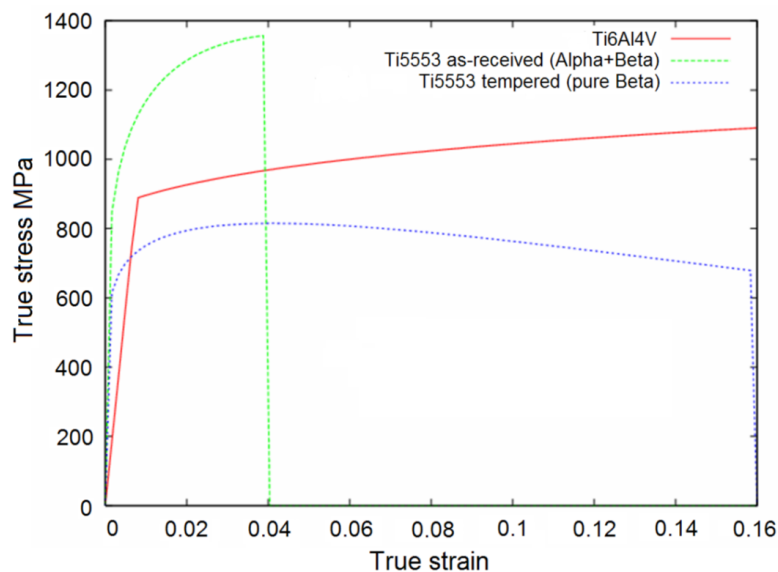


Figure 1.15: Tensile curves of Ti5553 with pure β phase, $\alpha+\beta$ phases and TA6V [35]

1.4.2 Texture

1.4.2.1 Introduction

The textures can be influenced by deformation and recrystallization. The stress applied to every crystal and the slip of dislocation in each crystal are different. It will cause hardening, deformation and rotation of the grains.

In recrystallization, the nucleation of new orientations during heat treatment follows Burger's relationship [36][37]. β to α follows: $\{0001\}\alpha \parallel \{110\}\beta$ and $\langle 11\bar{2}0 \rangle\alpha \parallel \langle 111 \rangle\beta$ (see in Figure 1.16). The closed-packed planes of these two phases and the close-packed directions of these two phases are parallel during this transformation. These structures can be formed by diffusion with the least driving force during recrystallization. The atomic distance of basal plane of $\{0001\}\alpha$ is slightly larger than $\{110\}\beta$. This will cause a slight atomic distortion in the crystal. A little increase of volume during this transformation can be observed. Consequently, this transformation will cause specific microstructures.

The Orientation Distribution Function (ODF) [38] is a convenient method to express textures. Euler space has been widely used for analyzing texture components [39][40]. During the processing of metallic materials, the texture components in Euler space are often gathered into several specific fibers. Plotting the intensity of the orientation distribution along these fibers is more efficient when analyzing the texture. For bcc metals, α -fiber, γ -fiber, and ε -fiber are the most studied. Figure 1.17 shows that the main texture fiber of bcc materials in ODF.

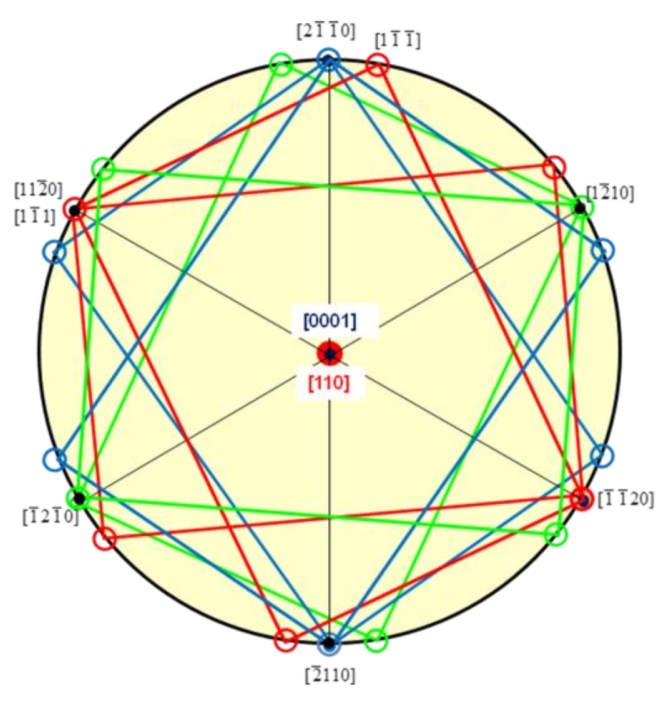


Figure 1.16: Stereographic projection of orientation relationship from β to α transformation

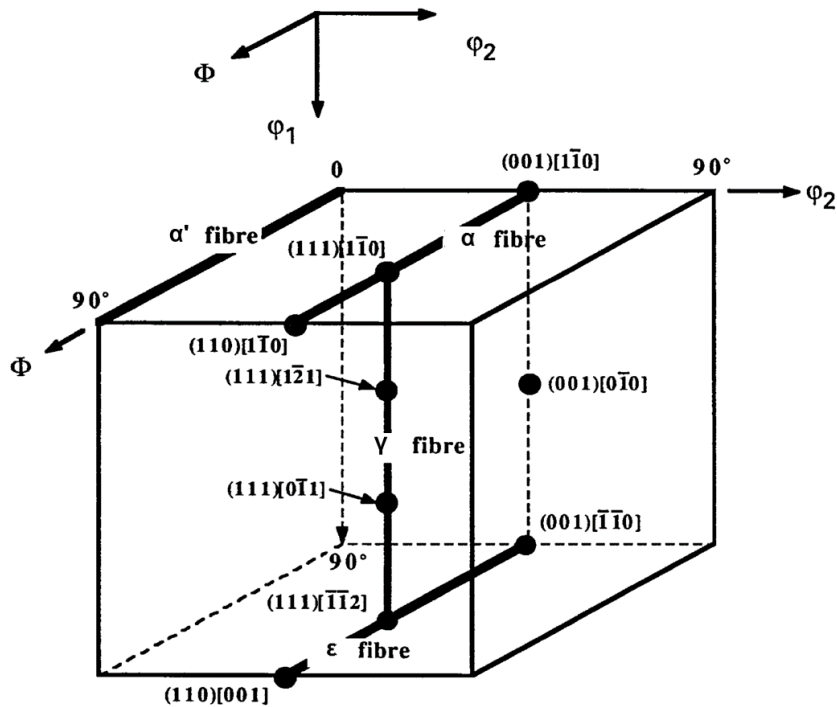


Figure 1.17: Main rolling texture fiber of bcc materials in ODF [41]

1.4.2.2 Effect of mechanical and thermal treatment on textures of titanium alloys

The $\{100\}\langle 110\rangle$ and $\{111\}\langle 112\rangle$ textures are the main deformation textures of β titanium alloys [42][43]. The $\{211\}\langle 110\rangle$ texture is formed during recrystallization after severe cold deformation [44]. Besides, a texture component of $\{554\}\langle 225\rangle$ is found in β titanium after recrystallization, near the direction of $\{111\}\langle 112\rangle$ [45][46]. This texture has a beneficial effect on yield strength [47]. A study of Ti-10V-4.5Fe-1.5Al shows the β phase concentrate on types of recrystallization textures: $\{001\}$ fiber such as $\{001\}\langle 110\rangle$, and γ fiber such as $\{111\}\langle 112\rangle$. These components are also affected by the annealing temperatures [48]. A study of Ti-Nb based β titanium alloy shows a strong recrystallization texture after 90% warm rolling with $\{111\}\langle 112\rangle$ texture component [49]. Figure 1.18 shows the corresponding ODF of the section $\varphi_2=45^\circ$ with a strong γ fiber.

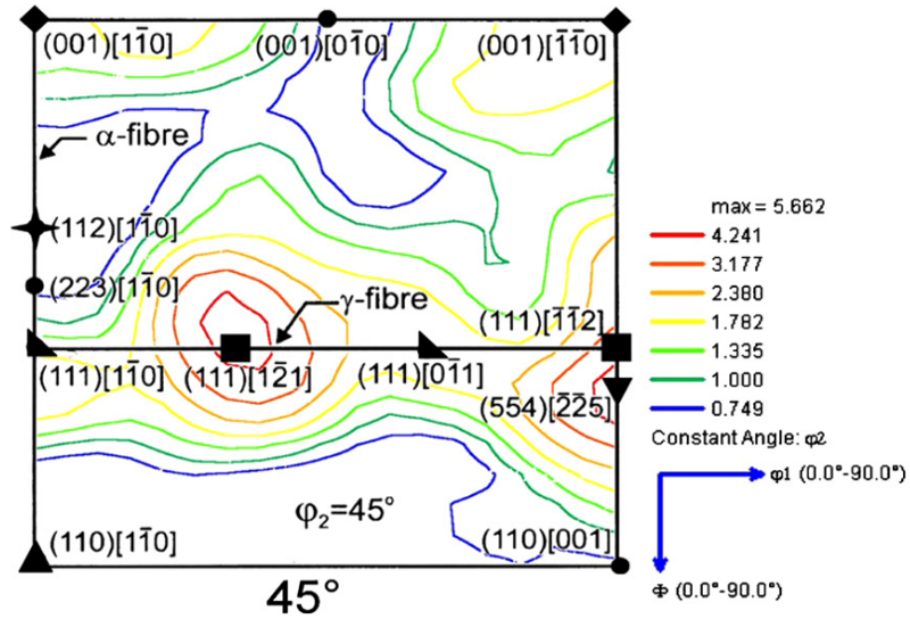


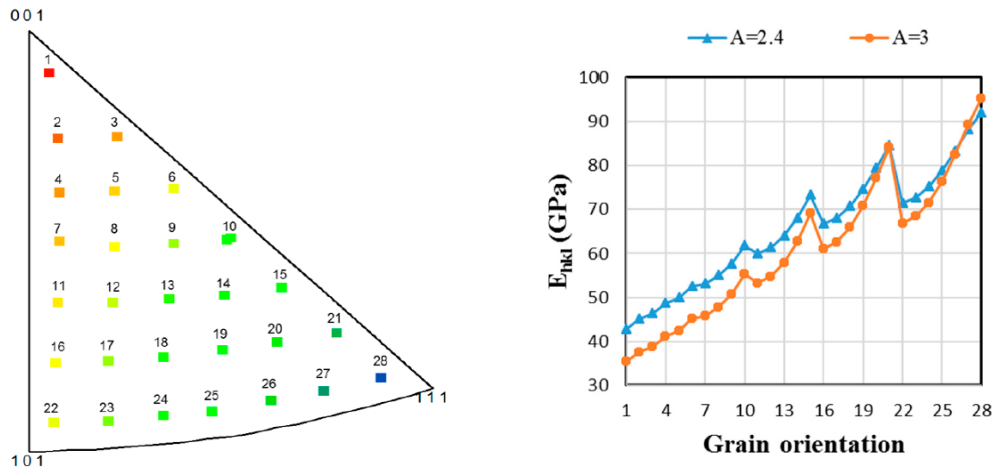
Figure 1.18: ODF of the section $\varphi_2=45^\circ$ with a strong γ fiber [49]

In general, the common texture of titanium alloy after recrystallization belongs to two fibers: α -fiber and γ -fiber. α -fiber is a group of textures whose $\langle 110\rangle$ axis are parallel to the rolling direction. The main components of this fiber are $\{001\}\langle 110\rangle$, $\{112\}\langle 110\rangle$ and $\{111\}\langle 110\rangle$. γ -fiber is a group of textures whose $\langle 111\rangle$ axis are parallel to the sheet's normal direction. The main components of this fiber are $\{111\}\langle 110\rangle$, $\{111\}\langle 112\rangle$ and $\{111\}\langle 123\rangle$.

1.4.2.3 Effect of textures on titanium alloys

The textures can cause anisotropic behaviour in strength, Young's modulus, elongations. This is due to the critical value of the shear stress for slip on crystallographic plane [50]. The Schmid factors are different in grains which affect the activation of slip systems. That is to say, the plastic anisotropy of polycrystals is determined by the different values of the Schmid factor in each direction [51][52][53][54][55].

The anisotropy can be controlled by the temperature and time of the solution treatment after severe deformation through texture control [56]. The effect of texture components on Young's modulus can be calculated by an elasto-viscoplastic self-consistent (EVPSC) model with different Zener factors, as shown in Figure 1.19 [57].



(a) The numbering of 28 orientations of single crystals (b) Young's modulus of these 28 orientations

Figure 1.19: Young's modulus parallel to the tensile axis of single crystal in 28 orientations obtained from two different β -phase single crystal elastic constants (SEC) ($A = 2.4$ and $A = 3$) [57]

1.4.3 Fractography

Fractography is a method of observing and analyzing the macrostructure and microstructure of the fracture surface. This method is often used to analyze the fracture mechanism and related microstructures of the material. Figure 1.20 shows an example of fractograph which indicates the cleavage facet, river pattern, tear ridge and dimples in Ti5553 alloys.

The β titanium alloys with β solution treatment after deformation and followed by aging show a mix-mode fracture after the tensile test. It contains intergranular

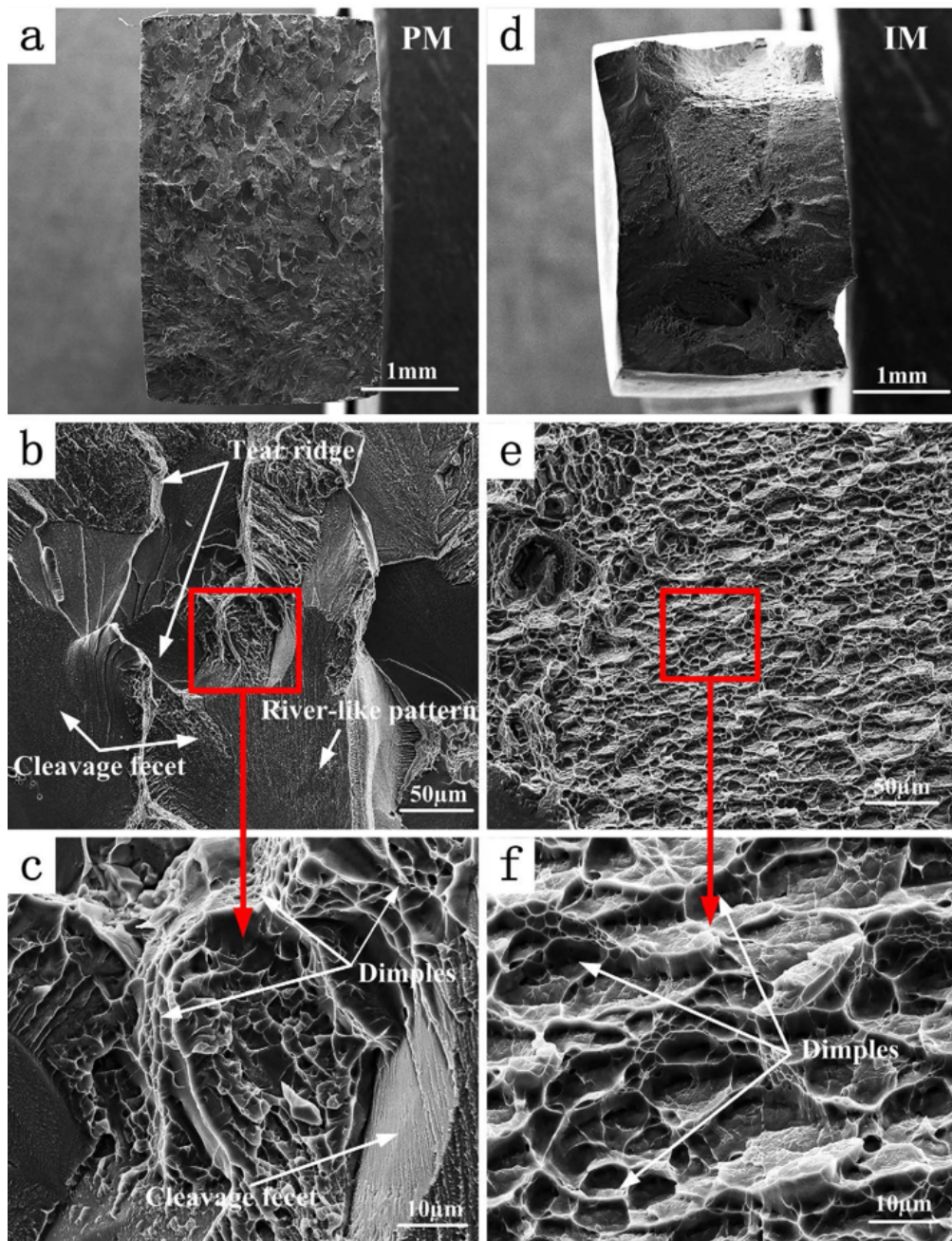


Figure 1.20: Fracture surfaces of Ti5553 of powder metallurgy (PM) and ingot metallurgy (IM): (a) macroscopic scale of PM; (b) and (c) microscopic observations show the cleavage facet, river pattern, tear ridge and dimples; (d) macroscopic scale of IM; (e) and (f) microscopic observations show the dimples [58]

and ductile fracture [16][59]. The α precipitation from aging process results in small dimples; however, the precipitation at grain boundaries leads to separation of grains [60][61].

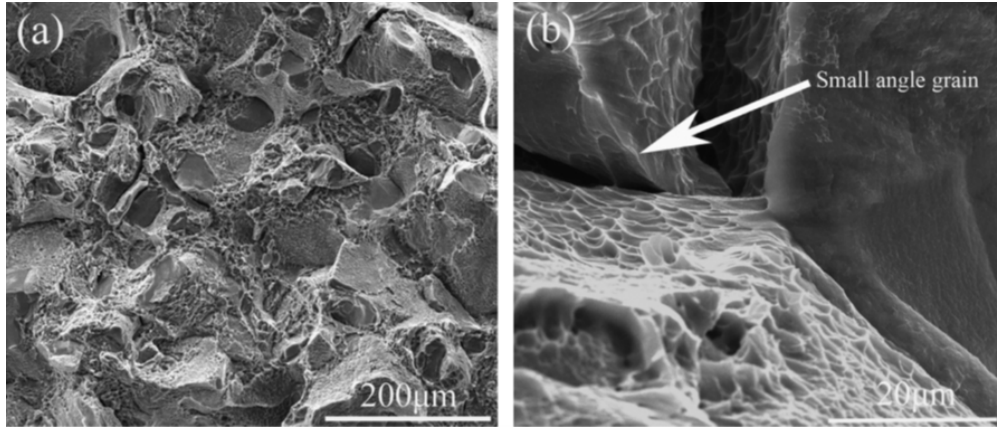


Figure 1.21: Fracture surfaces of Ti5553 after solution treatment at 830°C plus aging at 520°C [62]

1.5 Mechanical properties of titanium alloys

1.5.1 Effect of heat treatment on mechanical properties

The mechanical properties depend on the microstructure, including the arrangement of α and β phases, grains and texture. Table 1.3 shows the results presented in different studies where different microstructures have been submitted to specific heat treatments. As one can see, heat treatments but also microstructures lead to a large variety in the yield strength reached.

The mechanical properties of metastable β titanium alloys can be controlled by heat treatments. For example, Ti5553 are usually found under two different heat treatments. HT1 is solution treatment above β transus temperature and step-quenched to 600°C and then aging for 600 min, furnace cooling; HT2 is heat treatment below β transus temperature, air cooling to room temperature and aging at 600°C for 600 min, air cooling. The processing routes of these two heat treatments are shown in Figure 1.22.

The tensile properties, such as ultimate tensile strength (UTS), yield strength (YS), Elongation and Young's modulus (E) for these two conditions are shown in Table 1.4 and Figure 1.23 [68]. They all belong to precipitated state. E is almost the same. Ti5553 HT2 has higher UTS and YS but lower elongation than HT1.

The heat treatment HT1 aims to obtain the maximum ultimate tensile strength. The step-quench to 600°C can increase the nucleation rate of α phase and finally

Table 1.3: The phases, heat treatment and yield strength of some β titanium alloys

Materials	Conditions	YS (MPa)	Ref.
Ti-15V-3Cr-3Al-3Sn	β : ST at 810 °C (1 h); WQ.	701	[63]
Ti-15V-3Cr-3Al-3Sn	$\beta+\alpha$: ST at 810 °C (1 h); WQ; 500 °C (8 h); AC.	1179	[63]
Ti-10V-2Fe-3Al	β : ST at 850 °C (1 h); WQ.	576	[63]
Ti-10V-2Fe-3Al	$\beta+\alpha$: ST at 850 °C (1 h); WQ; 500 °C (8 h); AC.	932	[63]
Ti-5V-5Al-5Mo-3Cr	β : ST at 900 °C (1 h); WQ.	461	[63]
Ti-5V-5Al-5Mo-3Cr	$\beta+\alpha$: ST at 900 °C (1 h); WQ; 500 °C (8 h); AC.	1107	[63]
Ti-5Al-5Mo-5V-1Cr-1Fe	$\beta+\alpha$: ST at 850 °C (1 h); FC; 750 °C (2 h); AC; 650 °C (4 h); AC.	1170	[64]
Ti-5Al-5V-5Mo-3Cr-0.5Fe	$\beta+\alpha$: ST at 821 °C (3 h); AC; 621 °C (6 h); AC.	1245	[65]
Ti-3.5Al-5Mo-6V-3Cr-2Sn- 0.5Fe	β : ST at 830 °C (3 h); 830 °C (0.5 h); AC.	908	[62]
Ti-3.5Al-5Mo-6V-3Cr-2Sn- 0.5Fe	$\beta+\alpha$: ST at 775 °C (3 h); AC; 440 °C (8 h); AC.	1624	[62]
Ti-5Al-5Mo-5V-3Cr-1Zr	$\beta+\alpha$ BM: ST at 790 °C (2 h); AC; 600 °C (6 h); AC.	1248	[66]
Ti-5Al-5Mo-5V-3Cr-1Zr	$\beta+\alpha$ LM: ST at 860 °C (2 h); AC; 600 °C (6 h); AC.	1118	[66]
Ti-15V-3Sn-3Al-3Cr	β : ST at 800 °C (20 min); WQ.	723	[67]
Ti-15V-3Sn-3Al-3Cr	β : ST at 800 °C (20 min); WQ; CR(80%).	1025	[67]
Ti-15V-3Sn-3Al-3Cr	$\beta+\alpha$: ST at 800 °C (20 min); WQ; CR(80%); 450 °C (4 h).	1483	[67]

YS: Yield Strength

AC: Air Cooling

ST: Solution Treatment

WQ: Water Quenching

FC: Furnance Cooling

BM: Bimodal Microstructures

LM: Lamellar Microstructures

CR: Cold Rolling

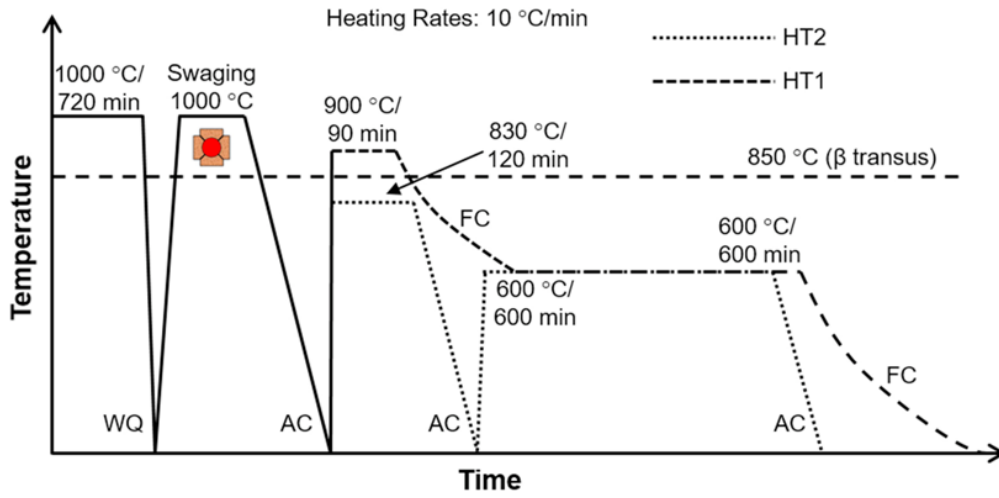


Figure 1.22: Processing route of HT1 and HT2 on Ti5553 alloys [68]

Table 1.4: Tensile properties of Ti5553 [68]

Condition	<i>UTS</i> (MPa)	<i>YS</i> (MPa)	Elongation (%)	<i>E</i> (GPa)
Ti5553 HT1	1147 ± 54	1052 ± 56	10.3 ± 5.6	114 ± 5
Ti5553 HT2	1440 ± 13	1369 ± 24	4.7 ± 0.7	116 ± 4

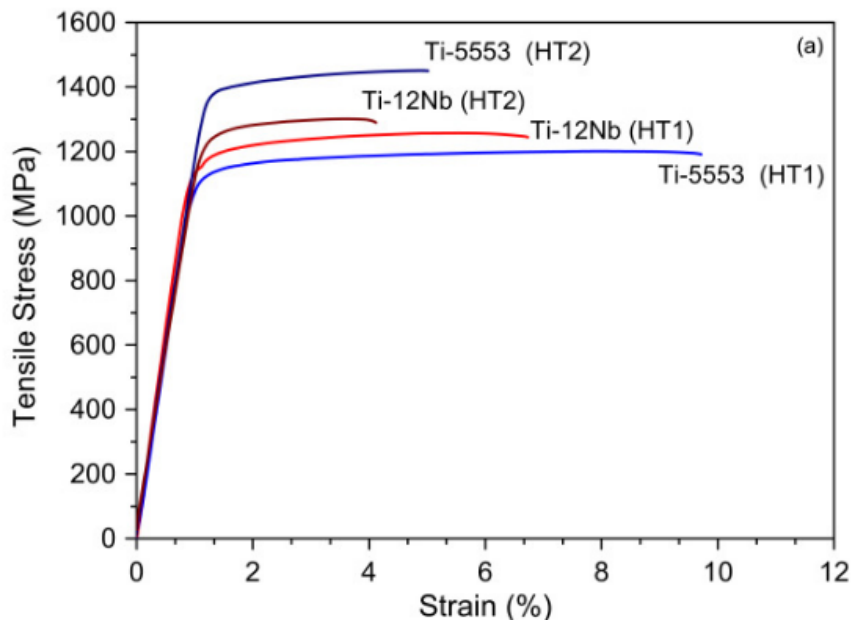


Figure 1.23: Tensile curve of Ti5553 and Ti-12Nb alloy under HT1 and HT2 treatment [68]

refine the α precipitation [69]. The heat treatment HT2 leads to bi-modal microstructure with primary α phase and fine α laths. It has the only purpose of maximizing ultimate tensile strength at any cost. This process sacrifices the ductility of Ti5553.

1.5.2 Influence of phase arrangement

In titanium alloys with α and β phases, equiaxed microstructures have the lowest yield strength and the highest final strain, which means this microstructure will make the materials more ductile. Lamellar microstructures present a strong resistance to cracking [70]. Bi-modal microstructures result from the combination of equiaxed and lamellar microstructures. They also combine their advantages. Fine-scale microstructures increase the strength, which can be realized by increasing the cooling rate [71]. Coarse microstructures can increase the resistance to creep and fatigue. Fine grains increase the ductility [10].

In β alloys, the tensile strength mainly depends on the second phase particles. The tensile yield strength (YS) and the interparticle spacing of α phase (d) can be linked by the following relationship [72]:

$$YS(MPa) = 850 + 70/d^{-1}(1/\mu m)$$

This can explain how fine α particles can increase the yield strength, by preventing the movement of dislocations.

An inverse relationship between strength and toughness is found in metastable β titanium alloys [73]. But a good combination of these two parameters can be realized by controlling thermo-mechanical treatment. If the formation of coarse α plates is controlled during the process of aging, β alloys can achieve very high yield strength such as 1500 MPa. However, if the material is over-aged, its ductility may be reduced close to 0. Therefore, the choice of an appropriate temperature of aging and cooling rate is essential [74].

1.5.3 Anisotropy

The rolling process form the textures and change the grain size and shape in metallic sheets. Recrystallization can eliminate this effect of the grains from deformation but recrystallization textures still have their affections. This will cause the anisotropy of mechanical properties.

Figure 1.24 shows the anisotropy of Young's modulus of strongly textured Ti-6Al-4V alloys [10]. The Basal/Transverse texture has lower Young's modulus in all directions. For all the textures, the Young's modulus along transverse direction (TD) is the highest and along rolling direction (RD) is the lowest. The textured

titanium sheets can have different mechanical properties because of the relationship between the crystal arrangement and the direction of the load.

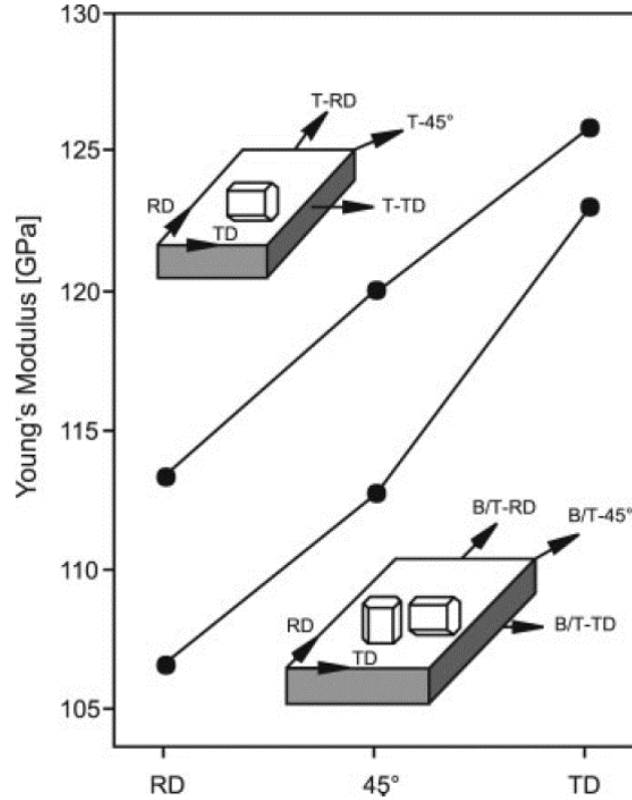


Figure 1.24: Effect of texture on the anisotropy of Young's modulus in Ti-6Al-4V alloys (T: Transverse texture, B/T: Basal/Transverse texture) [10]

The loading along different directions of the hexagonal unit cell of titanium alloys makes the obstacles to slip different. This causes the difference in yield strength and ductility. Figure 1.25 shows the anisotropy of yield strength and ductility RA in different tensile directions of Ti-6Al-4V alloys [26]. The 45° is where yield strength reaches its lowest value while ductility the highest. This can be explained that the tensile is 45° to the basal and prismatic planes so the shear stress is easy to reach its critical value. The displacement of dislocations can be activated easily.

Anisotropy is an important factor affecting plastic behaviors of the materials, this can have a great influence on forming. Lankford coefficients r are used to quantify anisotropy in metal sheets. These coefficients are defined by:

$$r = \frac{\varepsilon_2}{\varepsilon_3}$$

where ε_2 is true width strain which is transverse to the loading direction. ε_3 is true through thickness strain.

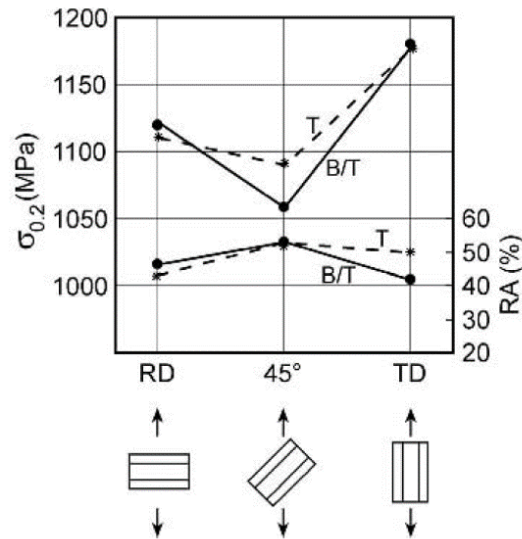


Figure 1.25: Effect of tensile directions on the anisotropy of yield strength and ductility RA in Ti-6Al-4V alloys [26]

The Figure 1.26 shows effect of r -value on the yield surface [75]. The r -value is equal to 1 when the material is isotropic. A material with a high r -value has good resistance to thinning, especially in the biaxial strain condition.

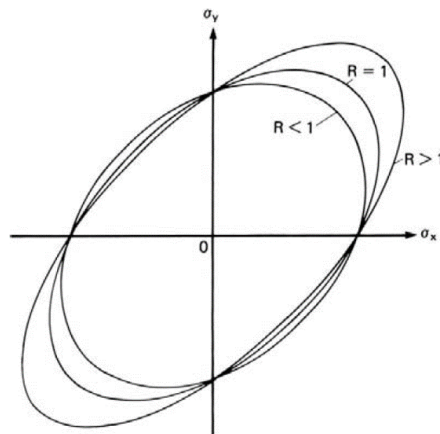


Figure 1.26: Effect of r -value on the yield surface [75]

If the tensile specimen is cut along the rolling direction, the calculated Lankford coefficient can be regarded as r_0 . For the same principle, r_{45} is calculated at 45° from the rolling direction and r_{90} is calculated for a tensile specimen along the transverse direction. The average \bar{r} can be calculated as:

$$\bar{r} = \frac{r_0 + 2r_{45} + r_{90}}{4}$$

Planar anisotropy coefficient Δr or planar r -value can be calculated as:

$$\Delta r = \frac{r_0 - 2r_{45} + r_{90}}{2}$$

High \bar{r} value is good for formability. High Δr is linked to the high dispersion of r -value in the different directions.

The anisotropy of a metal sheet can be affected by crystallographic texture. The predicted \bar{r} and Δr value of each texture component are listed as follows:

Table 1.5: Predicting plastic anisotropy by textures [76]

$\{hkl\}\langle uvw \rangle$	Euler angle ($\varphi_1, \phi, \varphi_2$)	\bar{r}	Δr
$\{001\}\langle 110 \rangle$	(45, 0, 0)	0.45	-0.88
$\{112\}\langle 110 \rangle$	(0, 35.3, 45)	3.33	-5.37
$\{111\}\langle 110 \rangle$	(0, 54.7, 45)	2.80	-0.44
$\{111\}\langle 112 \rangle$	(90, 54.7, 45)	2.80	-0.44
$\{554\}\langle 225 \rangle$	(90, 60.5, 45)	2.87	1.53
$\{110\}\langle 001 \rangle$	(90, 90, 45)	25.43	49.38

These parameters are calculated from the Taylor model. The textures with different Miller indices have different r -values, which may result in different formability in materials. It depends on the intensity of the texture components. The texture components with high \bar{r} value and low Δr value are preferable. It can be concluded that the texture components $\{112\}\langle 110 \rangle$, $\{111\}\langle 110 \rangle$ and $\{111\}\langle 112 \rangle$ have a good effect on the forming. $\{110\}\langle 001 \rangle$ is not suitable because of its high Δr value.

Some researchers have pointed out the effect of texture on the deformation and fracture behavior of the materials (Figure 1.27). It can be understood by the plastic anisotropy (r -value) affected by the texture. A high r -value can increase the limit strain by resisting the through-thickness slip [77].

1.5.4 Anisotropic yield criterion

1.5.4.1 Yield criteria used for titanium alloys

Hill quadratic yield criterion is often used for the modeling of the anisotropic yield behavior of titanium alloys [78]. This criterion can be seen as the expansion of Von Mises yield criterion [79].

$$F(\sigma_{22} - \sigma_{33})^2 + G(\sigma_{33} - \sigma_{11})^2 + H(\sigma_{11} - \sigma_{22})^2 + 2L\sigma_{23}^2 + 2M\sigma_{31}^2 + 2N\sigma_{12}^2 = 2f(\sigma_{ij})^2 \quad (1.1)$$

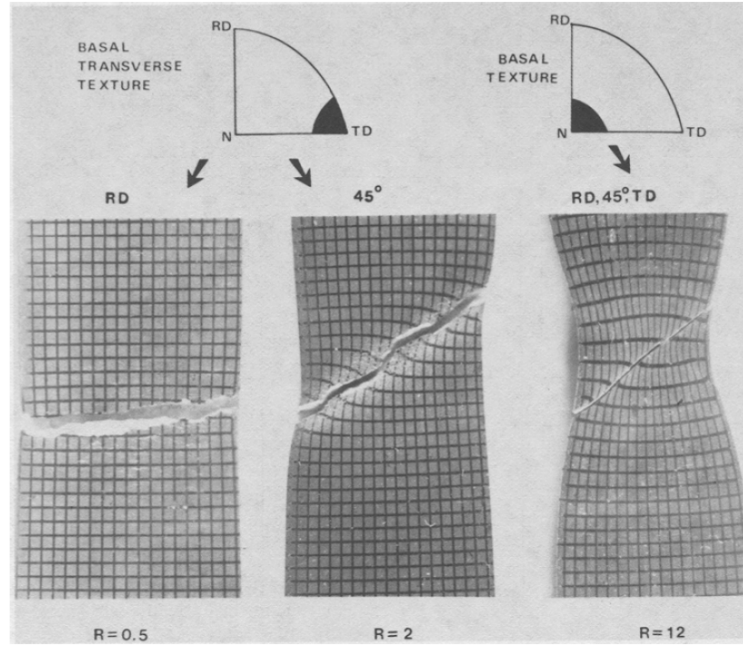


Figure 1.27: The influence of texture and r-value on the necking and fracture behaviour on tensile test by using TA6V [77]

Where F, G, H, L, M, N are constants that are related to the stress components: σ_{ij} . This is the so-called Hill48 criterion. Hill also presented Hill79 [80], Hill90 [81] and Hill93 [82] yield criteria. These may have a better fitting with the experiment results but makes the calculation more complex.

Hill48 yield criterion was used by many researchers in simulation of titanium alloys [83][84][85][86][87][88][89][90][91]. Hill's conventional anisotropic yield criterion is applied in the research of textured titanium alloys by Yamashita [92].

Other criteria such as YLD2000-2D criterion [93][94], or Cazacu 2006 criterion [95][96] were used but Hill's criterion is very simple to implement for titanium alloys and offers a good level of accuracy.

1.5.4.2 Calculation of the parameters of Hill48 yield criterion

Assuming that the axes of material anisotropy are orthogonal, $F, G, H, L, M,$ and N are the material parameters. When $F = G = H = 1, L = M = N = 3$, Hill48 criterion returns to isotropic Von Mises criterion. These values are generally defined through anisotropic parameters $R_{11}, R_{12}, R_{22}, R_{13}, R_{23}$ and R_{33} .

$$F = \frac{1}{2} \left(\frac{1}{R_{22}^2} + \frac{1}{R_{33}^2} - \frac{1}{R_{11}^2} \right); G = \frac{1}{2} \left(\frac{1}{R_{33}^2} + \frac{1}{R_{11}^2} - \frac{1}{R_{22}^2} \right); H = \frac{1}{2} \left(\frac{1}{R_{11}^2} + \frac{1}{R_{22}^2} - \frac{1}{R_{33}^2} \right) \quad (1.2)$$

$$L = \frac{3}{2R_{23}^2}; \quad M = \frac{3}{2R_{13}^2}; \quad N = \frac{3}{2R_{12}^2} \quad (1.3)$$

These anisotropic parameters are calculated from Lankford coefficients r_0 , r_{45} and r_{90} through the formulations below, assuming $R_{11} = R_{13} = R_{23} = 1$:

$$R_{22} = \sqrt{\frac{r_{90}(r_0 + 1)}{r_0(r_{90} + 1)}}; \quad R_{33} = \sqrt{\frac{r_{90}(r_0 + 1)}{r_0 + r_{90}}}; \quad R_{12} = \sqrt{\frac{3r_{90}(r_0 + 1)}{(r_0 + r_{90})(2r_{45} + 1)}} \quad (1.4)$$

1.5.5 Hardening laws

During the plastic deformation of metallic materials, the stress usually changes with the plastic strain. This phenomenon is due to the work-hardening, recovery, recrystallization during the deformation. This phenomenon can be affected by the strain hardening rate (n), strain rate ($\dot{\varepsilon}$) or temperature (T). The choice of the constitutive model is essential for finite element models and can affect the accuracy of the prediction of forming processes.

Many models exist, however, the strain rate ($\dot{\varepsilon}$) and temperature (T) are not considered in this work. Therefore, the strain-stress curve of the material can be defined by material models which accuracy depends on mathematical expression and parameter identification.

Table 1.6: Hardening laws of metallic materials

Names	Functions	Year	Reference
Hollomon's law	$\bar{\sigma} = K\bar{\varepsilon}^n$	1945	[97]
Swift's law	$\bar{\sigma} = K(\bar{\varepsilon} + \varepsilon_0)^n$	1952	[98]
Você's law	$\bar{\sigma} = A + B(-e^{-C\bar{\varepsilon}})$	1948	[99]
Ludwik's law	$\bar{\sigma} = \sigma_0 + K\bar{\varepsilon}_p^n$	1909	[100]
Hartley and Srinivasan's law	$\bar{\sigma} = \sigma_0 + K(\bar{\varepsilon}_p + \varepsilon_0)^n$	1983	[101]
Ludwigson's law	$\sigma = K_1\varepsilon^{n_1} + \exp(K_2 + n_2\varepsilon)$	1971	[102]

$\bar{\sigma}$: equivalent stress

$\bar{\varepsilon}$: equivalent strain

$\bar{\varepsilon}_p$: equivalent plastic strain

n : strain hardening coefficient

K, K_1, K_2 : strength coefficient

A, B, C : material parameters

σ_0 : initial yield stress

ε_0 : initial strain

In the Table 1.6, Hollomon's law is simple and only dependent on K, n [103]. Swift law, as well as Hollomon's law, can not realize the strain hardening of the materials with complex strain path [104]. Você's law is not suitable for modeling wide strain range [105]. Ludwik's law is proposed for isotropic materials but is

often chosen to identify the behavior of anisotropic materials [106]. Recent study shows that it is the most suitable law to model titanium alloys in uniaxial tension [107]. Hartley and Srinivasan's law is more suitable in large deformation [101]. Ludwigs law is suitable for steel and the fcc metals which have low stacking fault energy. This law has some deviations at low strains [108]. Considering the cases above, Ludwik's law is chosen for fitting in our work because it has good performance in fitting with titanium alloys and has simple parameters. It also gives better prediction in some specific conditions [109]. Ludwik's law is easy to implement and is defined with three parameters (σ_0 , K , n). It is therefore chosen in our works.

1.5.6 Conclusion

The modeling of material behaviour can have a strong influence on the accuracy of predictive models of forming processes. Microstructures clearly influence the mechanical properties. In this situation, a suitable mechanical and heat treatment must be chosen wisely. In the modeling of titanium alloys, Hill48 criterion and Ludwik's hardening law appear suitable for our research in titanium alloys.

1.6 Experimental FLC

In sheet metal forming processes, the onset of defects follows the evolution of plastic deformation in the sheet material. The over deforming aggravates the damage inside the material, leading to the failure of the sheet [110]. Many kinds of processing defects are produced in various conditions. Figure 1.28 shows several edge cracking during the forming procedure [111].

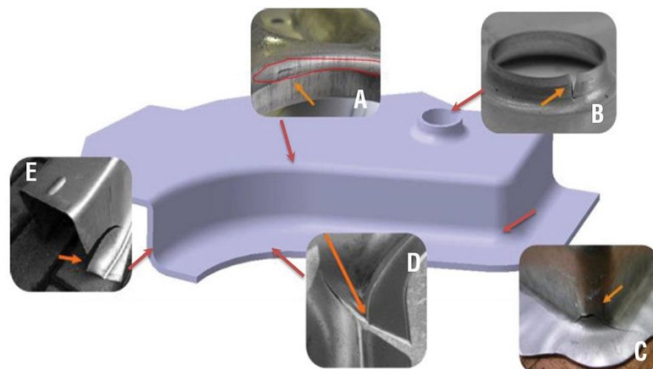


Figure 1.28: Edge cracking on the radius (A), edge cracking after hole flanging or collar forming (B), shearing crack at the deep-drawn edge (C), edge cracking at the flange (D), and edge cracking at the open head (E) [111]

The most useful tool to characterize formability is the Forming Limit Diagram (FLD) [112]. This diagram represents a plot of Forming Limit Curve (FLC) of major versus minor principal strains in the plane of the deformed sheet at the onset of necking. For a specific strain path, the material is safe when the strain condition is under the FLC. When the strain condition reaches the FLC, the necking happens. If the deformation continues growing, the failure of the material will occur rapidly [113]. This curve is the standard method to characterize the formability of a sheet metal [114][115]. The metal forming process can be controlled according to FLC.

The FLC contains the strain paths from uniaxial tension to equal-biaxial tension. It usually has its lowest point for plane strain condition. Four points can be defined to plot forming limit curves which are presented in Figure 1.29.

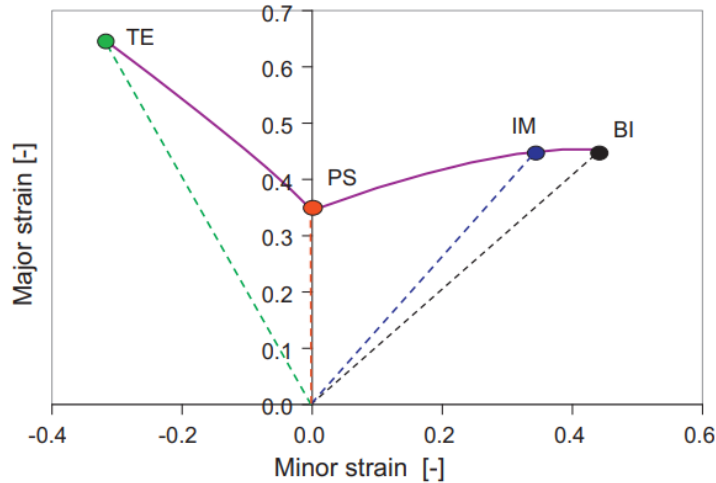


Figure 1.29: Four points to detect forming limit curves: TE: Tensile test at necking point; PS: plane strain; IM: intermediate biaxial; BI: equi-biaxial [116]

1.6.1 Nakazima and Marciniak tests

To determine the forming limit curves, there are two main methods: the out-of-plane stretching such as Nakazima test [117] and the in-plane stretching such as Marciniak test [118]. The Nakazima and Marciniak tests are shown in Figure 1.30.

Standard ISO 12004-2 explains the detail of the procedure to plot FLC. The detail of this method will be introduced in Chapter 2.

Nakazima test uses a rigid hemispherical punch. The stress state on the blank is triaxial. In order to eliminate the effect of bending, a large geometric size of the specimen and die are required. Because of the out-of-plane deformation, Nakazima test needs two cameras to capture the deformed shape of the specimen.

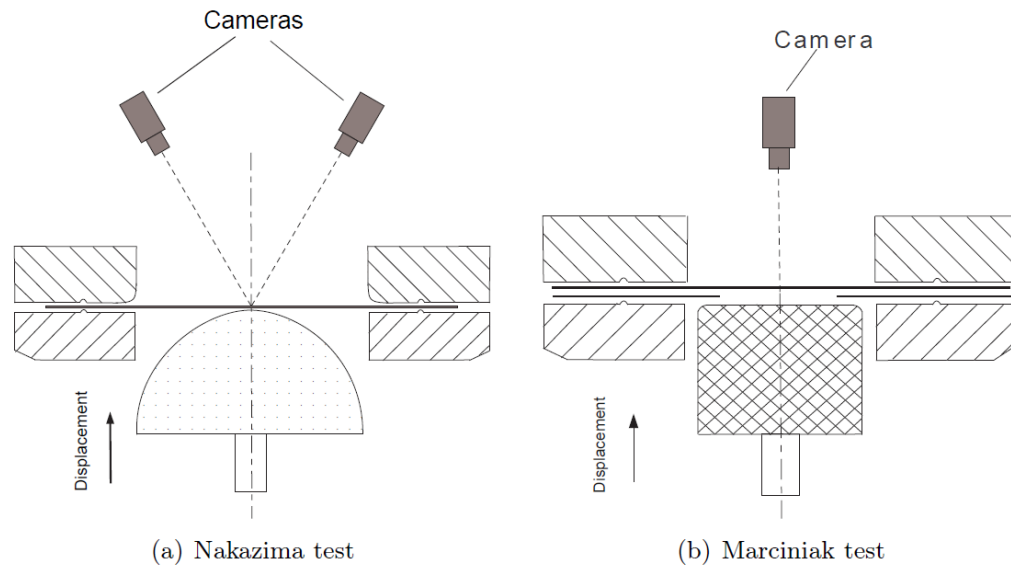


Figure 1.30: Nakazima and Marciniak tests [117][118]

The specimen is always in contact with the hemispherical punch during the test, consequently, it is difficult to eliminate the effect of friction.

Marciniak test leads to a plane stress state in the center area of the blank. Moreover, due to the special geometry of the specimen and the punch, there is no contact between the punch and the sheet in the center of the specimen, avoiding bending and friction effects. The surface of the specimen remains flat during the test so only one camera is needed to film the specimen [119].

Besides Marciniak test and Nakazima test, some other methods can be used to obtain limit strains. Figure 1.31 shows the curves from different testing methods. It demonstrates that these testing methods present limits. The Nakazima and Marciniak tests can plot the FLC for a large range of strain paths.

1.6.2 Factors affecting forming limit curve

Besides microstructures mentioned above, several factors can affect the shape and level of forming limit curves for a specific material.

1.6.2.1 Strain path

A strain path is made by a group of principal strain components ($\varepsilon_2; \varepsilon_1$) which ends up at the fracture point in FLD. The Figure 1.32 shows different strain paths by various methods.

The forming limit curve is strongly affected by the strain path history. Figure 1.33 shows the effect of strain path history. If a specimen is submitted to a uniaxial stretching ($\varepsilon_1 > 0$, $\varepsilon_2 < 0$) and then followed by a biaxial expansion ($\varepsilon_1 > 0$,

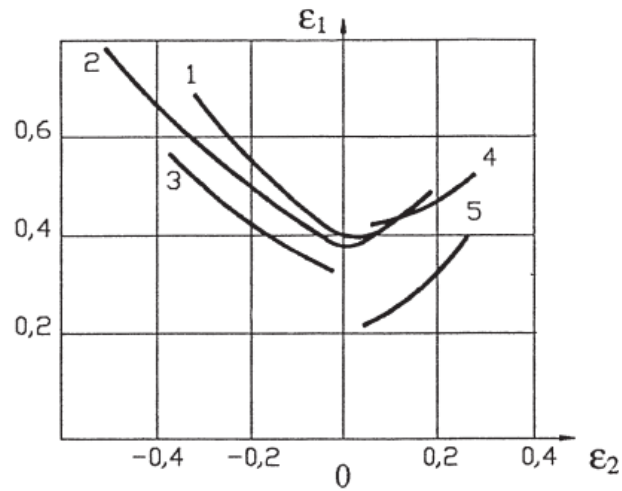


Figure 1.31: Forming limit curves by different testing methods: 1 Hasek test; 2 Nakazima test; 3 uniaxial tension test; 4 Keeler test; 5 hydraulic bulge test [120]

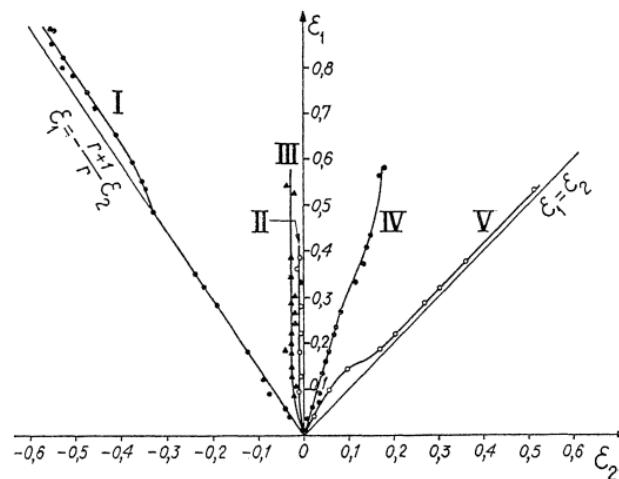


Figure 1.32: Strain paths from different methods. I: ISO 50 - From uniaxial tensile test with standard specimen; II: TPE 1 - From tensile test with thinned specimen; III: Swift 50 - From a flat bottom cylindrical cup with $\Phi=50$ mm; IV, V: From hydraulic expansion [121]

$\varepsilon_2 > 0$), the forming limit curve will be higher (II) than the curve with linear strain path (I). If the uniaxial tensile loading ($\varepsilon_1 > 0$, $\varepsilon_2 < 0$) is after a biaxial expansion ($\varepsilon_1 > 0$, $\varepsilon_2 > 0$), the forming limit curve will be lower (III).

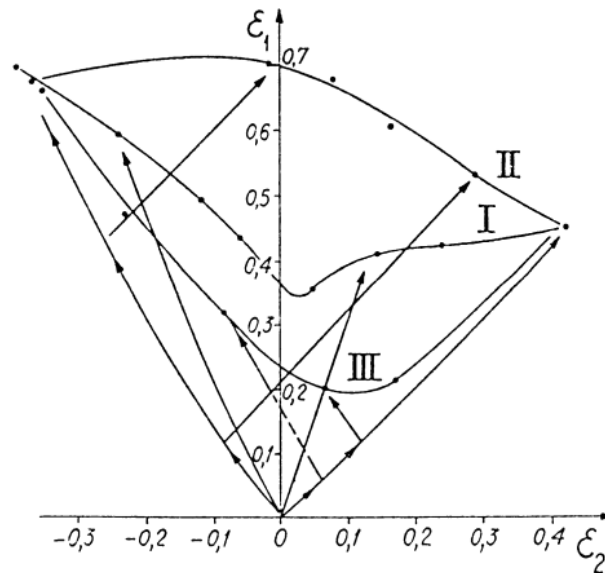


Figure 1.33: Influence of strain path on the forming limit curve [122]

1.6.2.2 Temperature

Temperature can affect FLC. Figure 1.34 shows the effect of temperature on the FLC for AA3003 aluminium alloys when the punch speed is 1.6 mm/s [123]. With the increase of temperature above 100°C, the level of FLC increases and formability is improved.

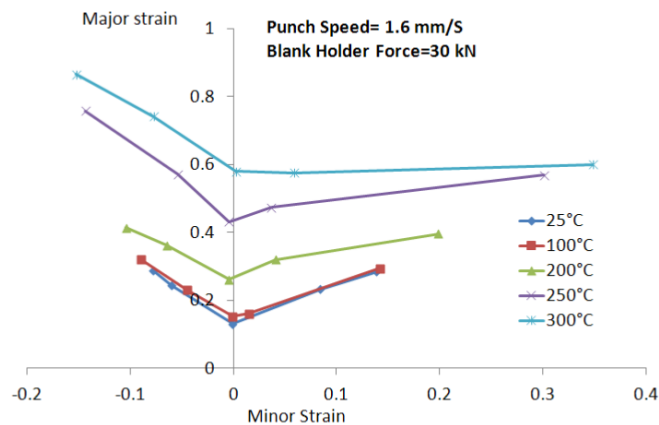


Figure 1.34: Influence of temperature on the forming limit curve [123]

1.6.2.3 Strain rate

Strain rate can also affect FLC. In Nakazima and Marciniak tests, this parameter can be controlled by punch speed. Figure 1.35 shows the effect of punch speed on the FLC for AA3003 aluminium alloys under two temperatures [123]. No matter the temperature, the FLC with a slower punch speed is higher. However, compared to the effect of temperature, the effect of punch speed remains low.

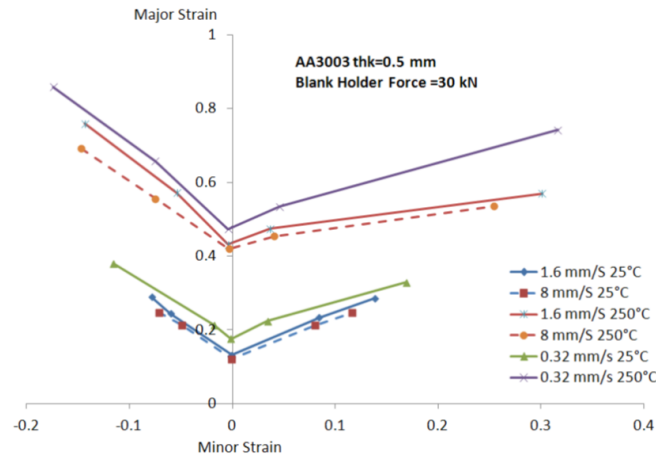


Figure 1.35: Influence of punch speed on the forming limit curve [123]

1.7 Predicted FLC

1.7.1 Models for predicting FLC

Different predictive models have been proposed that focus either on diffuse or localized necking. These models can help to reduce the experimental effort of formability characterization. The classification of theoretical models which can predict forming limit curves is shown in Figure 1.36.

Some important models are introduced below:

Hill presented a model with localized necking in 1948 [78]. Swift presented a model with diffuse necking in 1952 [98]. These models assumed that the sheet is homogeneous. Some models are based on the theory of ductile fracture criteria [125][126][127].

M-K (Marciniak-Kuczynski) model with thickness imperfection (groove) becomes popular [128] after the study of mini-grooves before fracture [129].

Pishbin tested the theory of Jones [130][131] and Gillis [132] which is based on the three-phase deformation idealization and Hill's non-quadratic flow law [80]. It concluded that the agreement between the models and the experiments is poor for aluminium alloys and fair for titanium alloys [133].

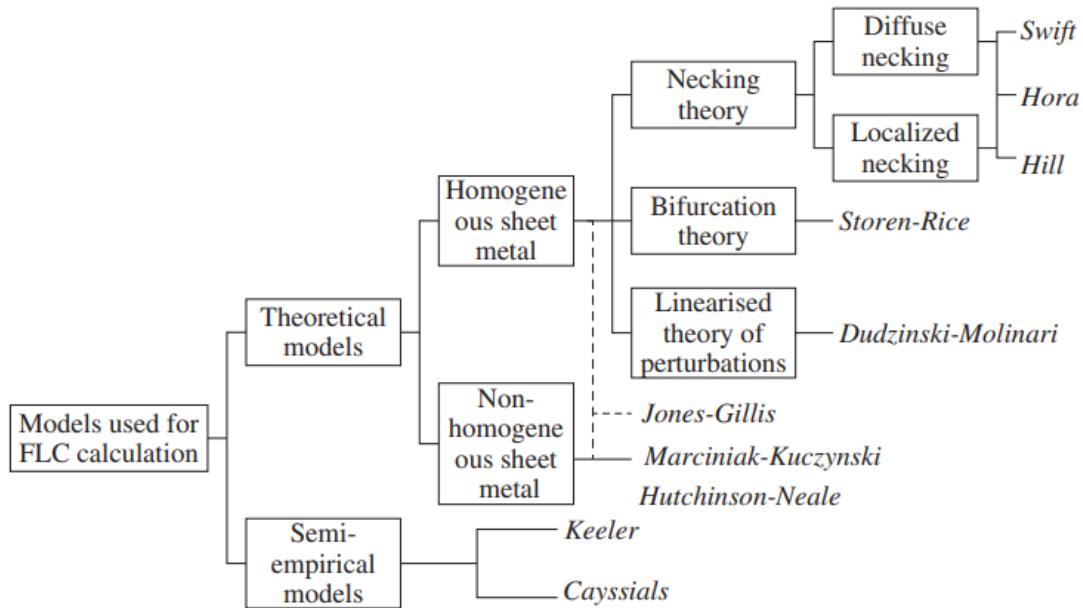


Figure 1.36: The classification of theoretical models for predicting forming limit curves [124]

Bressan's model proposed a shear stress mechanism in which instability of shear stress occurs in a specific plane when necking [134]. Then a strain gradient evolution model is used to overcome the limitation of fast shear stress fracture [135].

Storen and Rice model, which is based on the bifurcation theory, proposed a vertex on the yield surface to determine local necking [136]. This model has good agreement with some experimental results but has poor prediction in the negative quadrant of FLD [136][137].

Viscoplastic crystallographic slips and the Taylor approach [138] can be used to predict the FLC. It illustrates that texture, as well as anisotropy, influences FLC mainly for equibiaxial stretching [139].

1.7.2 Marciniak-Kuczynski model

1.7.2.1 Theoretical M-K model

M-K model is widely used for predicting FLC. The complete FLCs predicted by M-K model have good agreement with the experimental results as this is the case for aluminium alloys [140]. The model assumes that there is a pre-existing groove [128][141]. This geometrical defect can represent non-uniform microvoids, pre-cracks or other weak points in the material. The different deformations and fracture behaviors from textures can also be predicted by the models with imperfection [77]. The typical M-K model is shown in Figure 1.37. Axes 1, 2, 3

represent the rolling, transverse and normal directions of the sheet. The basic model assumes that the groove is perpendicular to axis-1.

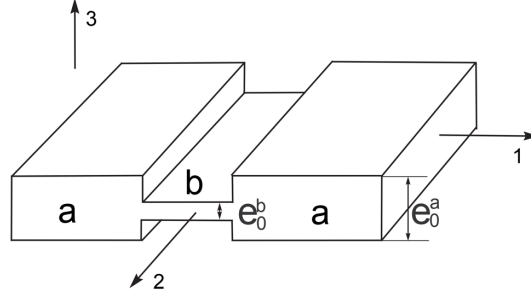


Figure 1.37: Representation of the M-K model

The geometrical imperfection can be quantified by an initial imperfection factor f_0 .

$$f_0 = \frac{e_0^b}{e_0^a} \quad (1.5)$$

Where e_0^a and e_0^b are the thicknesses of the sheet corresponding to the homogeneous region (zone a) and the region of the groove (zone b).

The model is subjected to plastic deformation in the two regions. The choice of yield criterion and constitutive model of the material have a great influence on the predicted forming limit curves [142]. For the Von Mises's yield function and plane stress condition ($\sigma_{13}^k = \sigma_{23}^k = \sigma_{33}^k = 0$, with $k = a$ or b).

$$(\bar{\sigma}^k)^2 = (\sigma_{11}^k)^2 - \sigma_{11}^k \sigma_{22}^k + (\sigma_{22}^k)^2 + 3(\sigma_{12}^k)^2 \quad (1.6)$$

Where $\bar{\sigma}^k$ is the equivalent stress, σ_{11}^k , σ_{22}^k and σ_{12}^k are stress tensor components. Swift's hardening law is applied here for example:

$$\bar{\sigma}^k = K(\bar{\varepsilon}_0 + \bar{\varepsilon}_p^k)^n \quad (1.7)$$

Where $\bar{\varepsilon}_p^k$ is equivalent plastic strain, n is strain hardening index, K and $\bar{\varepsilon}_0$ are material parameters.

The sheet metal can obey Levy-Mises flow rule:

$$\Delta \varepsilon_{ij}^k = \frac{\partial \bar{\sigma}^k}{\partial \sigma_{ij}^k} \Delta \bar{\varepsilon}_p^k, \quad i, j = 1, 2 \quad (1.8)$$

Where $\Delta \varepsilon_{ij}^k$ is strain component increment and $\Delta \bar{\varepsilon}_p^k$ is equivalent plastic strain increment.

The principle of volume constancy is:

$$\Delta\varepsilon_{11}^k + \Delta\varepsilon_{22}^k + \Delta\varepsilon_{33}^k = 0 \quad (1.9)$$

The same force in the direction 1 is transmitted across zone a and b. Hence the equilibrium equation are:

$$\sigma_{11}^a e^a = \sigma_{11}^b e^b \quad (1.10)$$

Where e^a and e^b are the current thicknesses of the sheet in zone a and zone b. Thickness e^a , and e^b are given by:

$$e^a = e_0^a \exp(\varepsilon_3^a), \quad e^b = e_0^b \exp(\varepsilon_3^b) \quad (1.11)$$

The major strain is assumed along 1-axis. The compatibility requirement assumes that the strain in zone b is limited by zone a in the groove direction:

$$\Delta\varepsilon_{22}^a = \Delta\varepsilon_{22}^b \quad (1.12)$$

By combining the equations above, a function $[F(\Delta\varepsilon_{11}^b)]$ of the value of increment $\Delta\varepsilon_{11}^b$ can be written. Finally, by using Newton-Raphson's method, an iteration step can be expressed as:

$$(\Delta\varepsilon_{11}^b)^{(i+1)} - (\Delta\varepsilon_{11}^b)^{(i)} = -\frac{F((\Delta\varepsilon_{11}^b)^i)}{dF/d((\Delta\varepsilon_{11}^b)^i)} \quad (1.13)$$

When the absolute value of increment $(\Delta\varepsilon_{11}^b)^{(i)}$ is less than a error E , $\Delta\varepsilon_{11}^b$ can be solved. For every increment $\Delta\varepsilon_{11}^a$, a strain increment $\Delta\varepsilon^b$ is obtained iteratively. The strain in zone a and zone b for every step of increment are noted. When the failure criterion is satisfied, the ε_{11}^a and ε_{22}^a at this moment are regarded as the forming limit strains. The whole FLC can be plotted by using different ratios of proportional loading.

Decades later the definition of M-K model was extended. The groove can be defined with an angle to the principal axis [143]. Effect of temperature has been added into the M-K model [144]. This model also has been used to predict FLC for titanium alloys [145][144][146]. Figure 1.38 shows the predicted FLC for Ti-6Al-4V for different strain rates from theoretical M-K model [147], at high temperature.

The presented theoretical M-K model is built on the basic hypothesis that the groove is perpendicular to the 1-axis. For the general case, the groove can have an angle Ψ_0 to the 1-axis. In order to simplify the calculation, a numerical approach based on the finite element method and on the theoretical M-K model with a groove perpendicular to the 1-axis can be used.

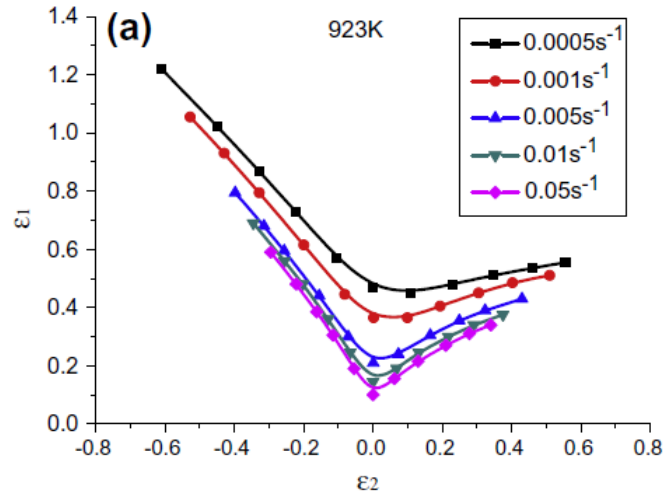


Figure 1.38: Predicted FLC for Ti-6Al-4V for different strain rates from theoretical M-K model [147]

1.7.2.2 Numerical M-K model

Compared to the theoretical M-K model, the numerical M-K model can include advanced mechanical behaviors of materials.

Researchers studied the effect of yield criterion, orientation of the defect, or mesh size on the predicted FLC [148]. Zhang et al. use the finite element method to predict FLC for AA5086 alloy [149]. Yuan et al. also compared the predicted FLC and experimental results for aluminium AA5754-O with a numerical M-K model [150]. Figure 1.39 shows the comparison of predicted FLC and experimental points of TNW700 titanium alloy by numerical M-K model from Liu [145]. The results show a good agreement in plane strain condition. The detail of this model will be introduced in Chapter 4.

1.7.3 FLC for titanium alloys

Very few studies exist on the determination of FLC for titanium alloys, especially for metastable β titanium alloys. Figure 1.40 shows the experimental results of Ti-grade 1 [151], Ti-grade 2 [152], Ti-6Al-4V [153][154], Ti-5Al-2.5Sn [154] and Ti40 [155]. The Ti-6Al-4V and Ti-5Al-2.5Sn are strongly textured so the limit strains in the left part of the FLC are very high, they are limited for the right part. Ti40, Ti-grade 1 and Ti-grade 2 have very good formability.

1.7.4 Conclusion

The numerical M-K model is a suitable model to predict FLC for titanium alloys because of its ease of implementation and wide applications. Generally, there is

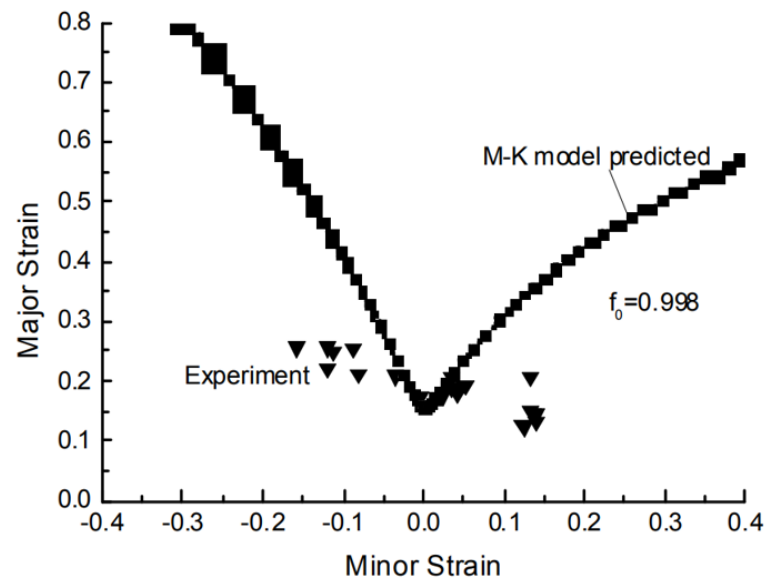


Figure 1.39: Comparison of predicted FLC from M-K model and the Marciniak test results for TNW700 titanium alloy [145]

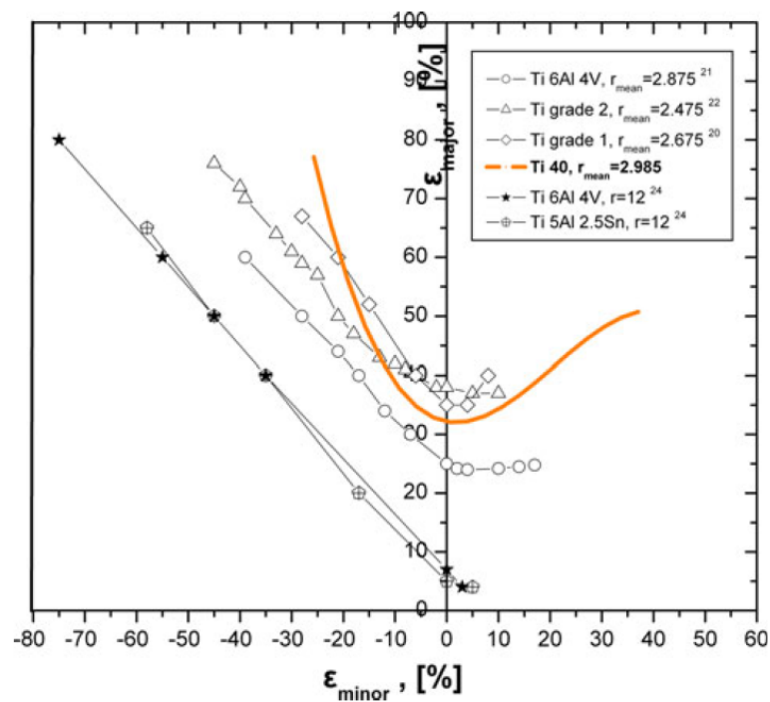


Figure 1.40: Experimental results of FLC for several titanium alloys [155]

also good agreement between the experimental results and the predicted FLC from M-K model. Because the predicted FLC is sensible to the imperfection value, the calibration of this value is essential to improve this agreement. No study exists on the prediction and characterization of metastable β titanium alloys.

1.8 Conclusion

Titanium alloys can have different microstructures by controlling the size and arrangement of the two phases α and β . Fine α phase plates can precipitate from the original β matrix to form a dispersed second phase, which is a strengthening mechanism of β alloys. The strengthening happens by hindering the movement of dislocations at interfaces between α and β phases at room temperature. This phenomenon lowers the ductility, and hence, reduces the formability. Textures also can affect the mechanical properties through anisotropy. Many researchers have focused on the mechanical properties of titanium alloys, as well as microstructure. But very few of them studied the effect of microstructure on formability.

Forming of titanium alloys is often used in the aviation industry. Forming limit curves is a widespread tool to achieve a complex formed component. This curve is also affected by the microstructures of titanium alloys. Investigating the relationship between the microstructure and the formability can lead to a better control over the manufacturing of titanium alloys.

FLC is used to characterize the formability of sheet metal. But plotting forming limit curves from experiments is very time-consuming and expensive. With the development of predictive models, predicted FLCs is increasingly used. Theoretical M-K model was demonstrated suitable to predict FLC for titanium alloys. M-K numerical model can be used to predict FLC because complex behaviors of materials can be introduced and it is easily implemented.

This work focuses on the study of the behavior of metastable β titanium alloys which are increasingly used in aeronautical applications replacing common α and $\alpha+\beta$ titanium alloys. The aim is to study the influence of microstructure, and particularly the texture, on the formability of such materials. The metastable β titanium alloys Ti21S and Ti5553 are selected for this study. Due to the complex procedure for detecting the whole forming limit curves, uniaxial tensile tests are firstly used to characterize one point of the FLC for different microstructures and also to determine the conventional mechanical properties for these different microstructures.

Chapter 2

Microstructure and mechanical properties

2.1 Introduction

Cold rolling and following heat treatment have a great influence on the microstructure, and particularly, on texture. This can affect the mechanical properties and formability of alloys.

In metastable β titanium alloys, α phase can precipitate to form a dispersed second phase. This will change the mechanical properties of the alloy. In this work, two newly developed metastable β titanium alloys Ti21S and Ti5553 are chosen. Mechanical properties of these two alloys with different rolling reduction rates (0%, 50%, 75%) and heat treatments are characterized by tensile tests. To study the effect of anisotropy, tensile tests at 0° and 90° from the rolling direction are conducted. Microstructures, with special attention to grain size and texture, are characterized by EBSD. Meanwhile, fractographs after tensile tests are observed by SEM. These analyses permit to discuss the effect of the microstructure on mechanical properties.

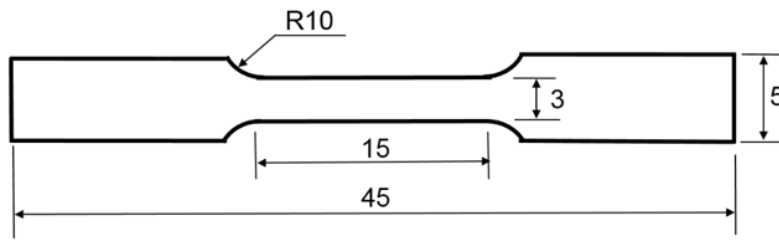
From tensile tests, one point on the forming limit curves for the uniaxial condition can be plotted. The relationship between microstructure and formability is investigated.

2.2 Experimental procedure

2.2.1 Materials, thermomechanical treatments and tensile tests

The received Ti21S sheet with thickness of 0.8 mm and Ti5553 forged bar which is cut with the thickness 1.5 mm are all solution treated at 900°C for 30 min and water quenched. This temperature is in the β phase zone of these two materials. Solution treatment at this temperature allows to dissolve all the α phase in the β matrix. Then these materials are cold rolled with a reduction rate of 0%, 50% and 75% which can give a global view of the effect of no deformation, medium and severe deformation on the microstructure. Then the materials are all again solution treated at 900°C for 30 min, and quenched in water. Recrystallization happens during this treatment and the squashed grains from cold rolling recrystallized to equiaxed grains. A part of treated Ti21S alloys is then heat treated at 650°C for 8 h and cooled in the furnace. From the TTT diagram of Ti21S (Figure 1.9 in chapter 1), the aging at 650°C for 8 h and cooling in the furnace allows precipitation of α phase from the solid solution of β phase. This treatment is suitable to study the effect of α precipitates in metastable β titanium alloys. This condition of Ti21S alloy which has $\alpha+\beta$ phases is named Ti21S+ in this work. Tensile specimens are machined as in Figure 2.1 and polished). To investigate the effect of anisotropy,

all the conditions are tested along the rolling direction and transverse direction.



(a) Dimensions of the tensile specimen (mm)



(b) Painted tensile specimen

Figure 2.1: Tensile specimen

The name of specimens contains the materials and both direction parameters and rolling parameters, with the form: (Material) (direction parameter),(rolling rate), which shown below:

Materials:

Ti21S (β)

Ti21S+ ($\alpha+\beta$)

Ti5553

Directions:

L: along the longitudinal direction, i.e, the rolling direction

T: along the transverse direction

Rolling parameters:

0: Reduction rate of 0% (without cold rolling)

50: Reduction rate of 50%

75: Reduction rate of 75%

All the experimental procedures and naming of Ti21S and Ti5553 alloys are summarized in Figure 2.2. The name of the specimens of each condition is displayed with a red frame in the figure. Especially, the specimen labeled Ti5553 RM corresponds to the raw material with no heat treatment. There is no Ti5553 T,0 because of the symmetry of the Ti5553 forged bar.

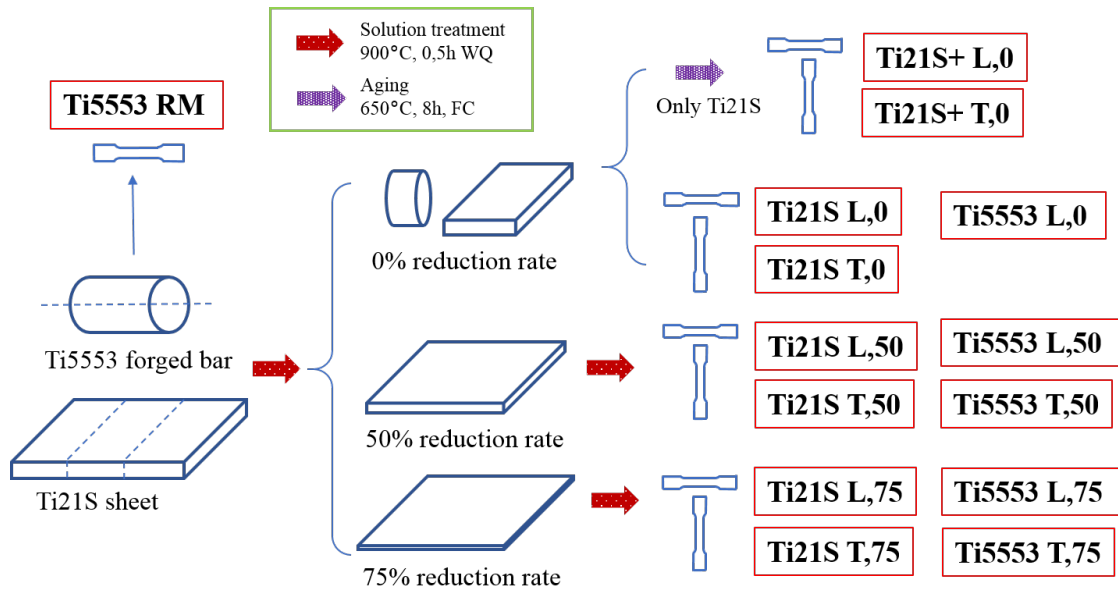


Figure 2.2: Mechanical and heat treatment applied to Ti21S and Ti5553 alloys

The tensile tests are carried out on INSTRON-3345 testing machine, at room temperature with an initial strain rate of 10^{-3}s^{-1} . Every specimen is painted with speckle pattern to permit DIC (Digital image correlation) method which will be explained later. A camera is set for filming the deformation of the specimens during the tensile test. For each condition, five specimens are tested. The specimens which have necking outside of the center deformation zone will not be taken into account. Samples with large dispersed results are neglected.

2.2.2 EBSD

In order to find the effect of microstructure on mechanical properties, EBSD is conducted to characterize microstructures, including grain size and, the most important, texture.

Rectangle EBSD samples are cut from the corresponding materials. The length is along the rolling direction. The procedure of the EBSD samples is showed below:

(a) Cut-off

The samples with the appropriate size about 15×10 mm are cut off from the materials by a cutting machine.

(b) Mounting

The samples are put into a holder in order to have better handling and protection. Hot mounting is conducted to cover the samples.

(c) Grinding

Grinding papers from rough to fine are used during this procedure. Silicon Carbide (SiC) papers are used, with the grit of 800, 1000, 1200, 2000. After each

paper, a rotation of 90° of samples is needed in order to totally eliminate the scratches from the previous step.

(d) Polishing

Polishing textile is used in this procedure to make sure the sample is very flat. During the polishing, a special solution of OP-S colloidal silica is used.

(e) Etching

In order to reduce the residual stress on the surface of the samples, etching with a particular solution needs to be conducted. The time of this procedure is strictly controlled. Any inadequate etching and over-etching will strongly affect the image we observe. The solution of 5% HNO_3 and 5% HF in water with an etching time of 10 s are applied.

(f) Scanning

Several continuous areas per sample are scanned to acquire sufficient information about the samples. A general quick scanning is conducted at first to verify the sample surface condition and grain size. Then the samples are scanned in detail with a step size of 1/10 actual average grain size.

(g) Analyzing

For a specimen, several areas along the rolling direction are scanned to maximize the number of grains contained. The obtained EBSD IPF (inverse pole figure color coding) maps of several areas are merged into a large EBSD IPF map. The calculated information of grain sizes and textures are based on these merged EBSD IPF maps. The inverse pole figures give a global view of the texture distribution in the samples. ODF (orientation distribution function) which is a classical three-dimensional tool to characterize texture, is also used.

2.2.3 Method of plotting forming limit points

Figure 2.3 shows geometry of specimens that can be used to plot FLC and the corresponding strain path. It can be seen that the tensile test gives one point at the uniaxial tension part of FLC [156]. The forming limit points of Ti21S and Ti5553 with different microstructures can be obtained by this tensile test.

To obtain the limit strain of these points, the strains during tensile tests must be identified. A very convenient and affordable way to measure the strain field is Digital Image Correlation (DIC) [157][158]. This measurement method uses the images which are acquired by a camera. The surface of the specimen is sprayed by a speckle pattern (Figure 2.1). When the specimen is under deformation, the pattern will deform and its deformation can be calculated by following the displacement of subsets.

GOM Correlate is a software often used to calculate the strain components at each point in the gauge area at any instant time. In order to make the results

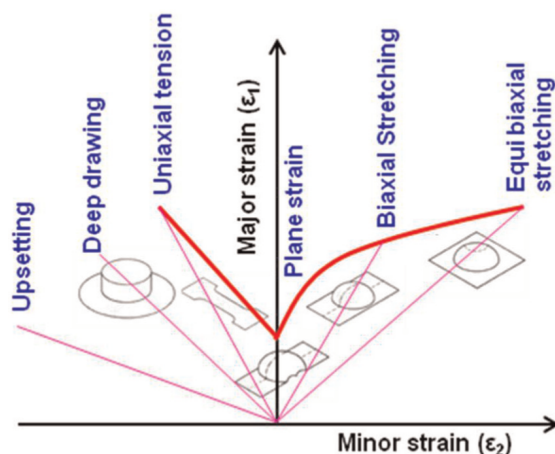


Figure 2.3: Specimen geometries and the corresponding strain paths of FLC [156]

more reliable, three sections in each specimen are chosen. The strains along the section just before the rupture can be plotted. Due to the onset of necking, rupture happens at the position with the highest major strain at the next moment. The detail of this method is presented in Figure 2.4 and the definition of the parameters in Table 2.1, by using an example of Ti21S L,0.

Table 2.1: Definition of parameters in detecting limit strain

Parameters	Definition
Position X	Length of sections on the specimen (mm)
A	The rightest point of the left fit window
B	The leftest point of the right fit window
W_l	Width of the left fit window
W_r	Width of the right fit window

This method to detect limit strains from the strain distribution curves was introduced by ISO 12004-2 [119] for Marciniak and Nakazima tests. For each section, to calculate the limit major strain ϵ_1 , the distribution of major true strain is plotted (example for section 1 in Figure 2.4). At the beginning, two inner boundary points A and B are chosen manually according to the dividing point of the strain unstable zone on the curve. Besides, the width of two fit windows W_l , W_r are chosen. Then, an inverse parabola defined by a quadratic equation (Eq. 2.1) is used to fit the experimental points in the two fit windows.

$$f(x) = \frac{1}{ax^2 + bx + c} \quad (2.1)$$

Where a, b, c are constants which are optimized by the iteration algorithm. The highest point on the inverse parabola is the limit strain ϵ_1 .

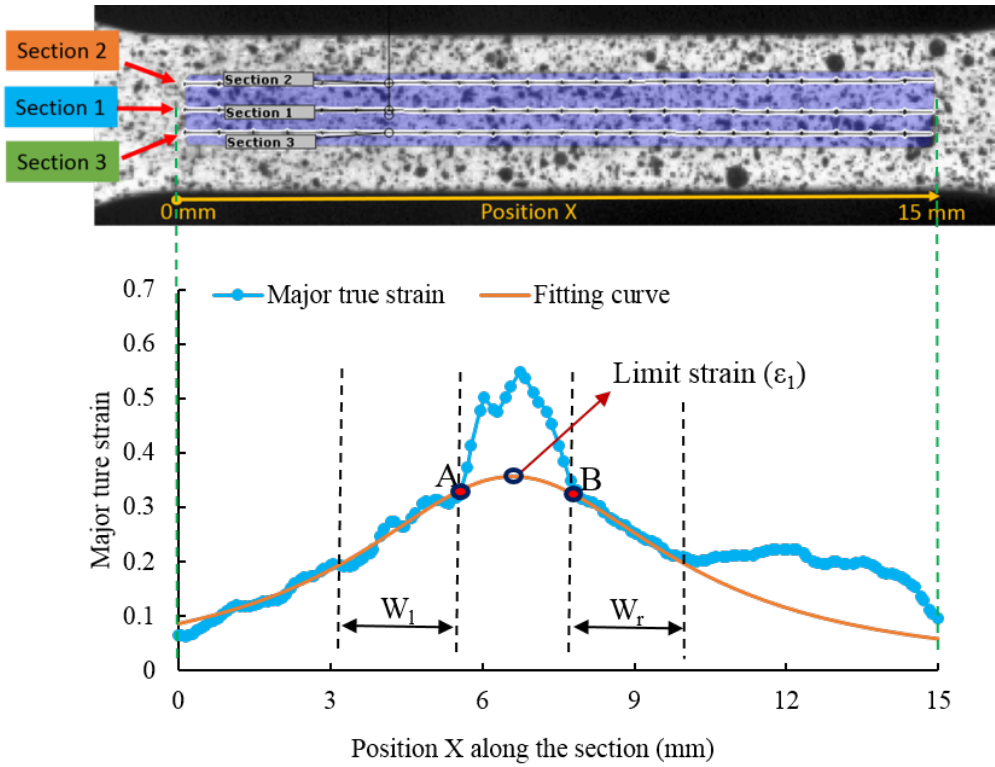


Figure 2.4: Detecting forming limit strain from ISO 12004-2 [119]

To calculate the limit minor strain ε_2 , Chu et al. proposed a modified method different from the standard, using the determined experimental strain path [109]. The ε_2 value corresponds to the ε_1 on the actual strain path at the limit strain (see in Figure 2.5). The result from the modified method improves the measure of minor strain, especially when the strain is large.

2.2.4 Method for calculating Lankford coefficients r

Lankford coefficients (r -values) permit to characterize the anisotropy of a rolled sheet. These values can be calculated in every corresponding direction. Since the tensile tests along the rolling direction and transverse direction are conducted in this work, the r -value can be calculated for these two directions. The comparison of these r -values can highlight the effect of microstructure on the tensile anisotropy of Ti21S and Ti5553 alloys.

In order to calculate r -values, the strain components ε_2 and ε_3 are needed as $r = \varepsilon_2/\varepsilon_3$. The ε_3 is the deformation along the normal direction so that it is hard to measure directly. The principle of incompressibility is then applied: $\varepsilon_3 = -\varepsilon_1 - \varepsilon_2$. Therefore, using GOM software to calculate ε_1 and ε_2 , r -values can be determined.

Here we choose Ti21S L,0 as an example to introduce the method of calculating r -values by using GOM Correlate software. Five points are chosen on each spec-

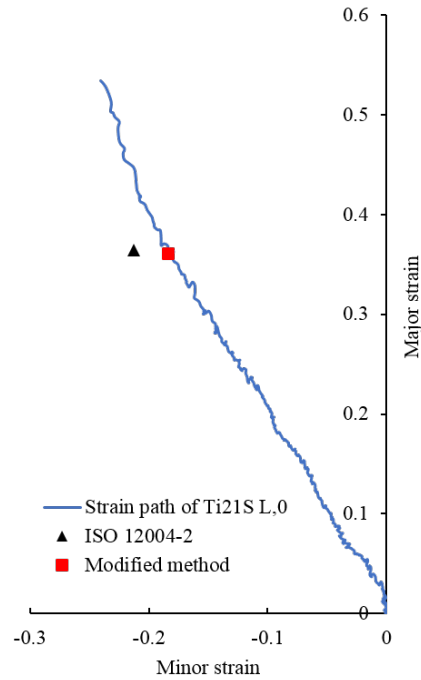


Figure 2.5: Comparison of limit points from ISO 12004-2 and modified method proposed by Chu [109]

imen to minimize the errors. These equally spaced five points need to be located in the zone with plastic deformation of the tensile specimen (see in Figure 2.6).

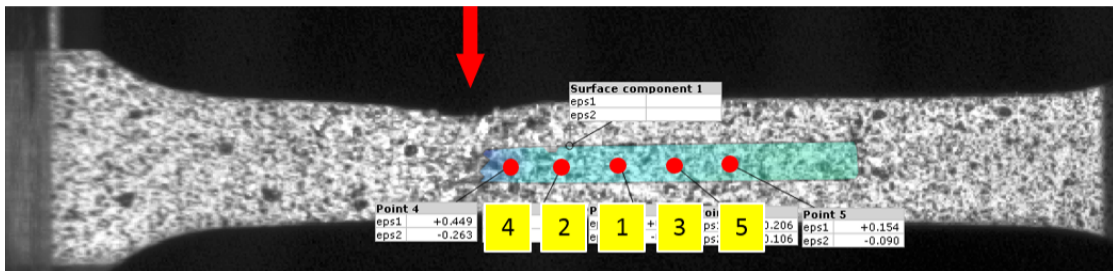


Figure 2.6: Position of the five selected points on the specimen Ti21S L,0

A range of strain from 50% to 75% of maximum strain is chosen to ensure homogeneous increments on the strain components ε_2 and ε_3 and precise r -values evaluation (Figure 2.7). The range can be adjusted when the increments are not homogeneous.

Then, the strain evolution of ε_2 and ε_3 of the five points in this range (Figure 2.8 (a)) are plotted. A linear tendency curve is plotted to fit the averaged curve. The slope of this linear fitting curve gives the r -value (Figure 2.8 (b)).

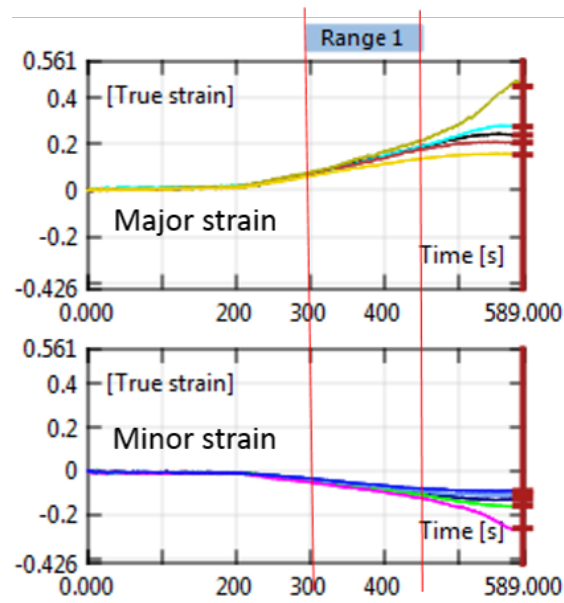


Figure 2.7: Strain range of 50%-75% of maximum strain for the specimen Ti21S L,0-1

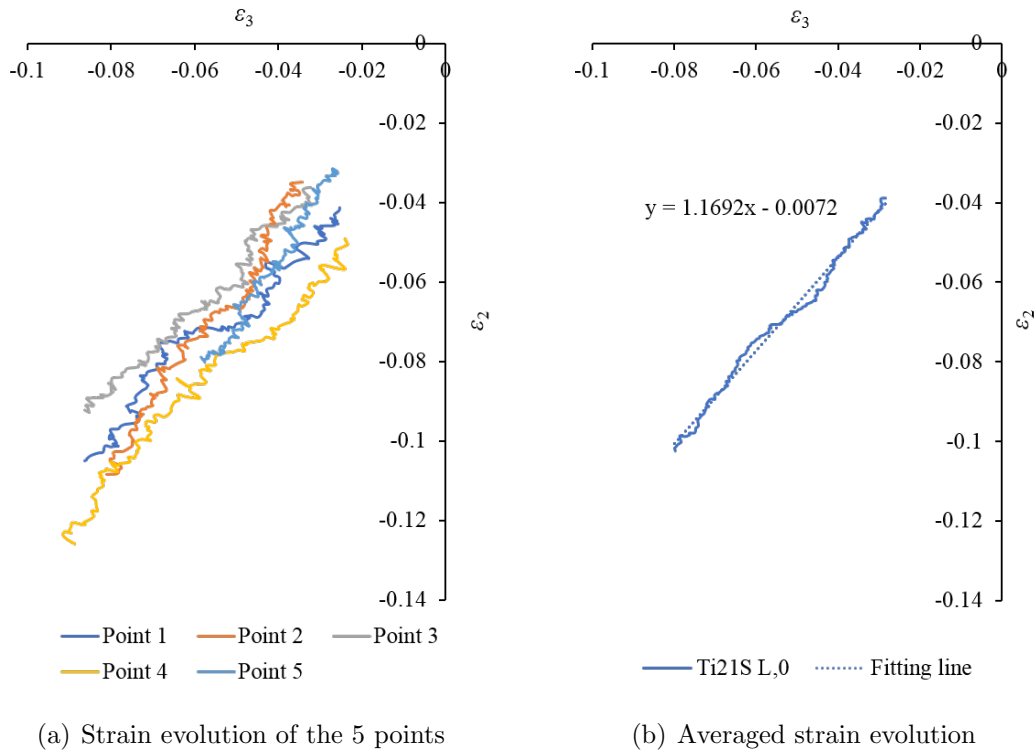


Figure 2.8: Evolution of ε_2 and ε_3 of the 5 points chosen on specimen Ti21S L,0 and its averaged strain evolution curve

2.3 Microstructure of Ti21S and Ti5553 alloys

2.3.1 Grain size of Ti21S and Ti5553 alloys

Figure 2.9 shows the EBSD results of Ti21S and Ti5553 alloys for each rolling reduction rate: 0%, 50% and 75%. The grains are fully equiaxed. Therefore, recrystallization structure is for all the specimens after the solution treatment.

A statistic of average grain size and its standard deviation of Ti21S and Ti5553 alloys is shown in Table 2.2. Grain diameter distribution of these two materials are shown in Figure 2.10 and Figure 2.11.

Table 2.2: Statistics of average grain size and standard deviation of Ti21S and Ti5553 alloys

Specimen	Average grain size/ (μm)	Standard deviation $\bar{\sigma}/(\mu\text{m})$
Ti21S 0	66	34
Ti21S 50	78	42
Ti21S 75	79	41
Ti5553 0	225	157
Ti5553 50	130	87
Ti5553 75	109	78

We can see from the Table 2.2, Figure 2.10 and Figure 2.11, after the heat treatment, the Ti21S alloy with cold rolling has slightly larger grain size. Their distribution is similar, whatever the cold rolling rate. Ti5553 has a larger grain size than Ti21S. All the conditions have a quite dispersed distribution of grain size, especially Ti5553 0. This phenomenon is due to the limited number of grains scanned by EBSD. The largest grain is for Ti5553 0, which has a diameter of 600 μm . This phenomenon is probably due to the large size of grains in the received materials.

2.3.2 Texture of Ti21S and Ti5553 alloys

2.3.2.1 Inverse pole figure

Inverse pole figures of Ti21S and Ti5553 alloys are presented in Figure 2.12 and Figure 2.13. In these figures, the evolution of the global texture can be seen. For Ti21S, an increased density of $\{113\}$ //sheet plane is exhibited. With the increase of rolling reduction rates, the maximum densities are increased slightly. The inverse pole figures of Ti5553 0 show strong $\{115\}$ //sheet plane textures.

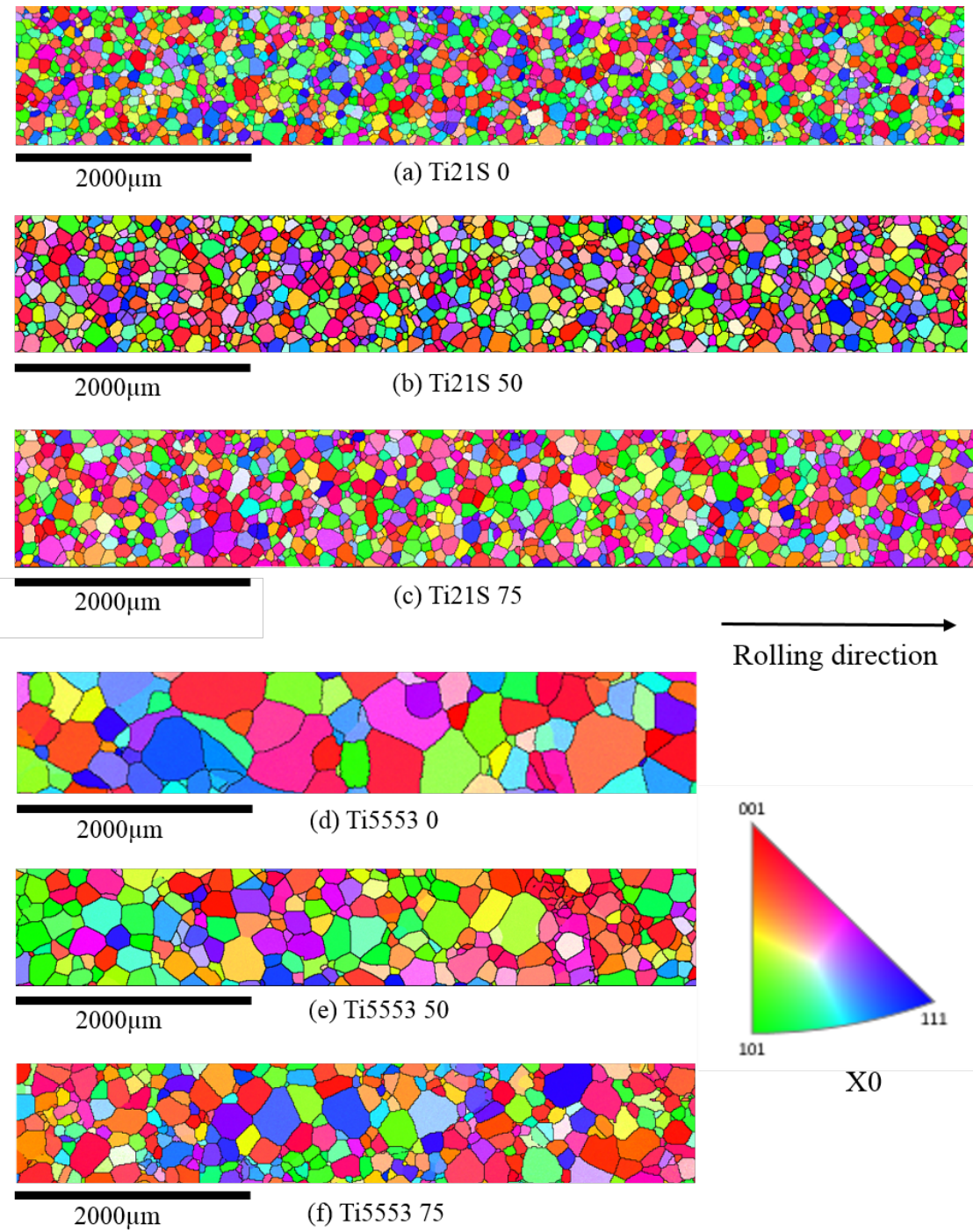


Figure 2.9: EBSD IPF maps of Ti21S and Ti5553 alloys (X direction is along rolling direction)

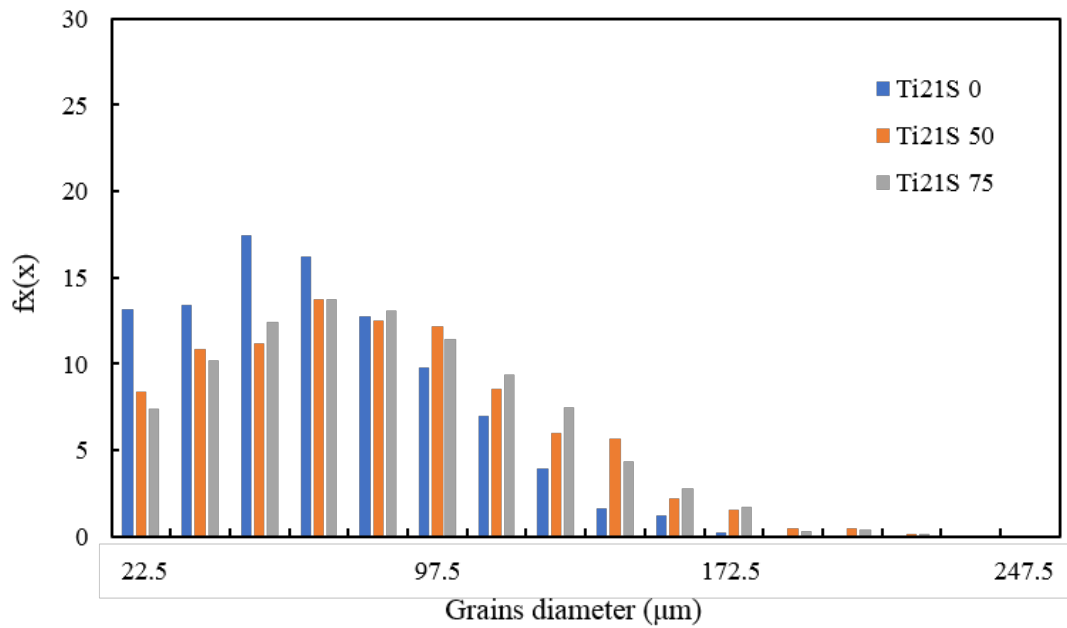


Figure 2.10: Distribution of grains diameter of Ti21S alloy

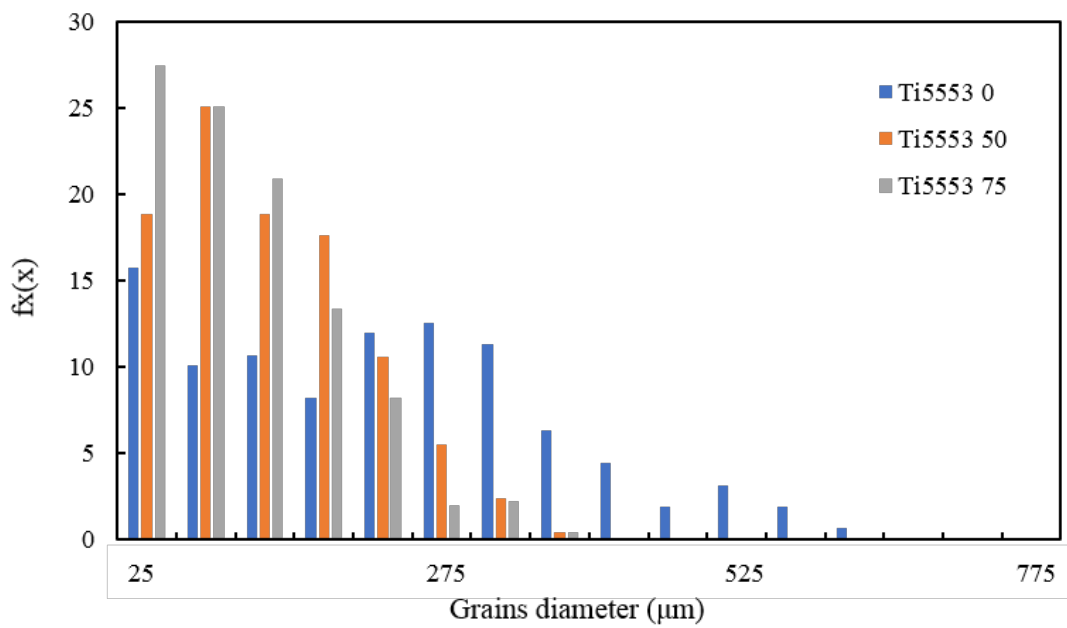


Figure 2.11: Distribution of grains diameter of Ti5553 alloy

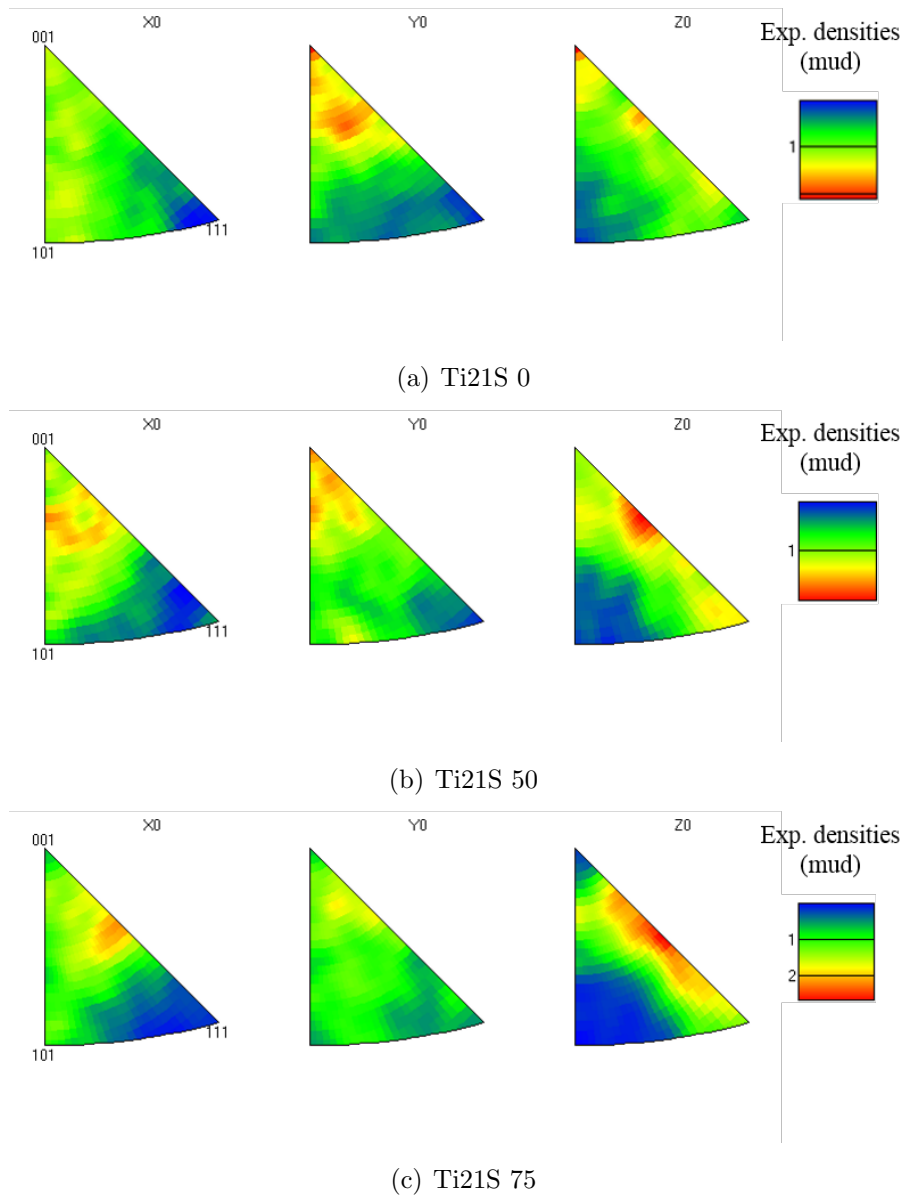


Figure 2.12: Inverse pole figure of Ti21S (a) 0% reduction rate, (b) 50% reduction rate, (c) 75% reduction rate (X0 corresponds to the rolling direction)

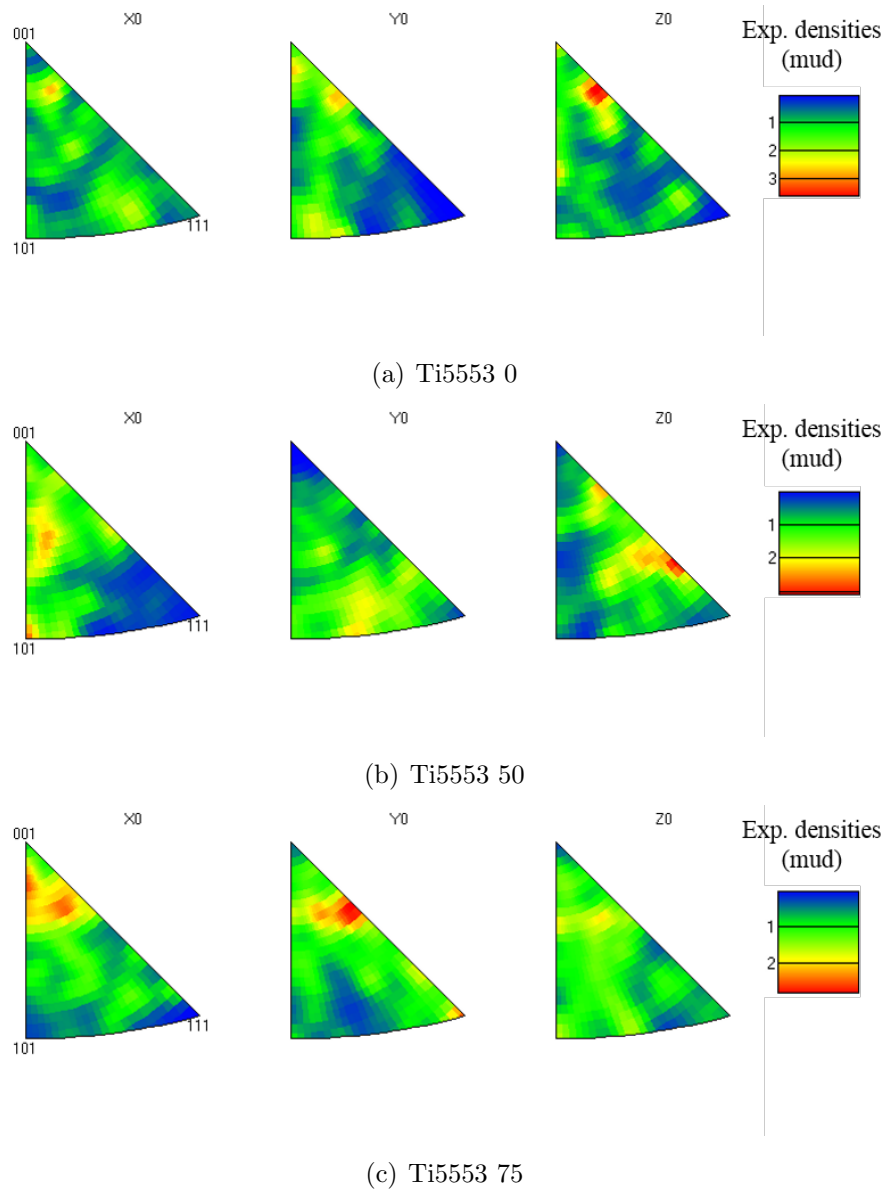


Figure 2.13: Inverse pole figure of Ti5553 (a) 0% reduction rate, (b) 50% reduction rate, (c) 75% reduction rate (X0 corresponds to the rolling direction)

2.3.2.2 ODFs

In order to analyze several specific texture components, the most frequently used $\varphi_2=45^\circ$ section of ODF of Ti21S and Ti5553 alloys in different conditions are shown below. The whole ODF of each condition is listed in Appendix A, where the texture components are marked and located.

The $\varphi_2=45^\circ$ sections of ODF of Ti21S for different conditions are plotted in Figure 2.14. The ODF shows the low intensity of the texture in Ti21S 0 and Ti21S 50. Ti21S 75 has the highest intensity compared to other conditions. Several texture components are developed: like $\{112\}\langle 02\bar{1}\rangle$ in Ti21S 0, $\{113\}\langle \bar{6}9\bar{1}\rangle$ in Ti21S 50 and $\{238\}\langle \bar{2}4\bar{1}\rangle$ in Ti21S 75.

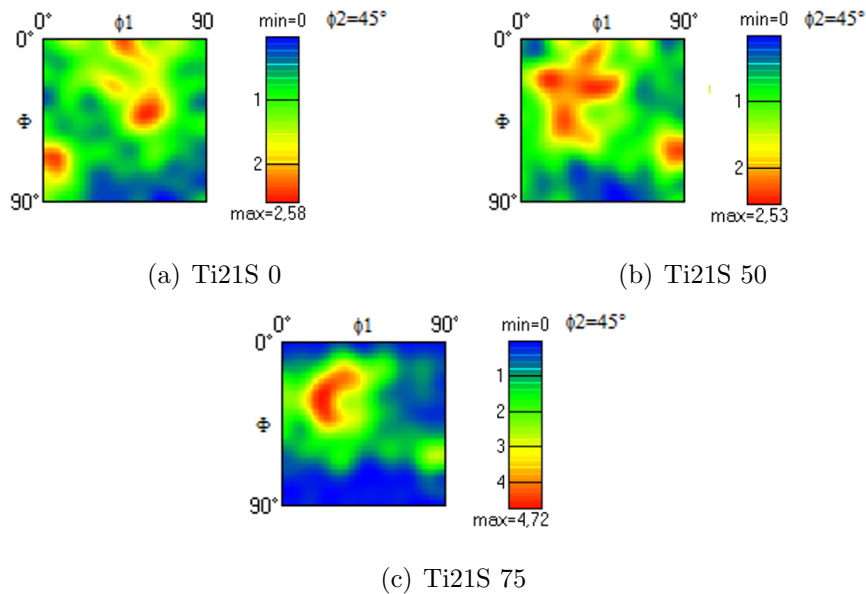


Figure 2.14: $\varphi_2=45^\circ$ section of ODF of Ti21S (a) 0% reduction rate, (b) 50% reduction rate, (c) 75% reduction rate

The $\varphi_2=45^\circ$ sections of ODF of Ti5553 for different conditions are plotted in Figure 2.15. The ODF shows a higher density of textures than Ti21S, but it decreases when the rolling reduction rate increases to 75%. The Ti5553 0 has an evident texture of $\{115\}\langle 55\bar{2}\rangle$ and $\{225\}\langle \bar{3}8\bar{2}\rangle$ which disappears for the other two conditions. The Ti5553 50 has its special orientation of $\{321\}\langle 01\bar{2}\rangle$, while the Ti5553 75 forms a texture of $\{110\}\langle 1\bar{1}2\rangle$. Large texture difference are observed for all the conditions.

2.3.3 Conclusions

Specimens of Ti21S and Ti5553 have been tested in their solution-treated conditions. Ti5553 has a larger grain size than Ti21S. This step brings alloys various

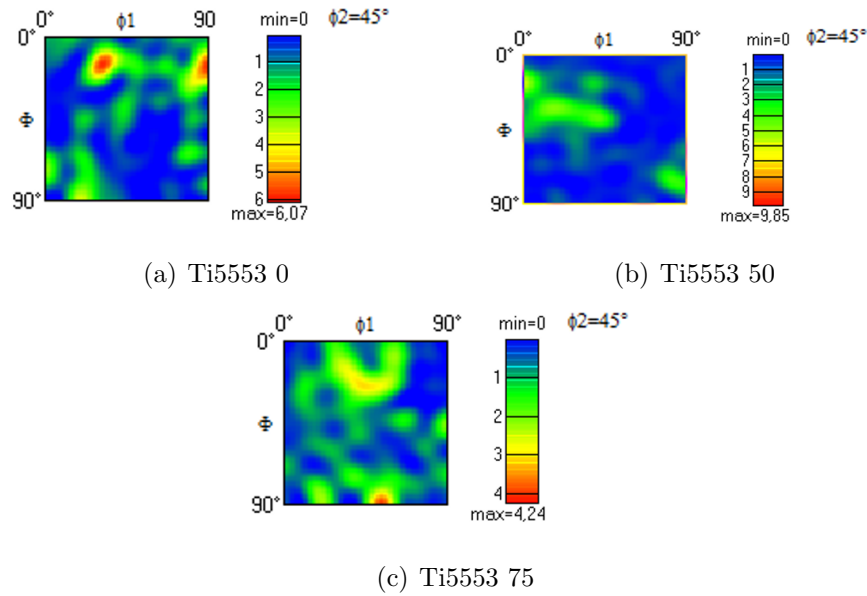


Figure 2.15: $\varphi_2=45^\circ$ section of ODF of Ti5553 (a) 0% reduction rate, (b) 50% reduction rate, (c) 75% reduction rate

recrystallization textures according to the previous deformation texture. Ti21S shows fewer concentrations on the texture compared to Ti5553 alloys. With the increase of rolling reduction rates on Ti21S alloys, the texture $\{1\ 1\ 3\}$ //sheet plane is reinforced. Ti21S 0 has its special textures of $\{4\ 6\ 5\}\langle 0\ 5\ \bar{6}\rangle$. Ti21S 50 has $\{3\ 1\ 1\}\langle 1\ 2\ \bar{5}\rangle$, $\{1\ 1\ 4\}\langle \bar{1}\ 7\ \bar{2}\rangle$. Ti21S 75 has $\{2\ 3\ 8\}\langle \bar{2}\ 4\ \bar{1}\rangle$, and also $\{3\ 1\ 1\}\langle 1\ 2\ \bar{5}\rangle$. For the textures of Ti5553 alloys, $\{5\ 1\ 2\}\langle \bar{1}\ 9\ \bar{2}\rangle$, $\{2\ 2\ 5\}\langle \bar{3}\ 8\ \bar{2}\rangle$ and $\{1\ 1\ 5\}\langle 5\ 5\ \bar{2}\rangle$ textures are found in Ti5553 0. When the rolling reduction rate is 50%, these textures disappear and all the texture components are concentrated into $\{3\ 2\ 1\}\langle 0\ 1\ \bar{2}\rangle$. However, this concentrated texture becomes disperse into $\{1\ 1\ 0\}\langle 1\ \bar{1}\ 2\rangle$, $\{0\ 1\ 4\}\langle 1\ 0\ 0\rangle$ when the rolling reduction rate increased to 75%.

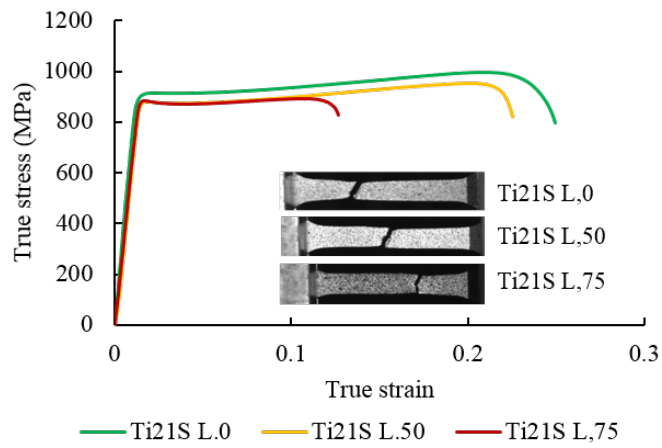
2.4 Tensile tests of Ti21S and Ti5553 alloys

Tensile tests of Ti21S and Ti5553 alloys are conducted. True stress - true strain curves, mechanical properties and forming limit points are evaluated for all the microstructures. The analysis of these results permits to have a comprehensive understanding of the effect of the mechanical and thermal treatments on mechanical properties.

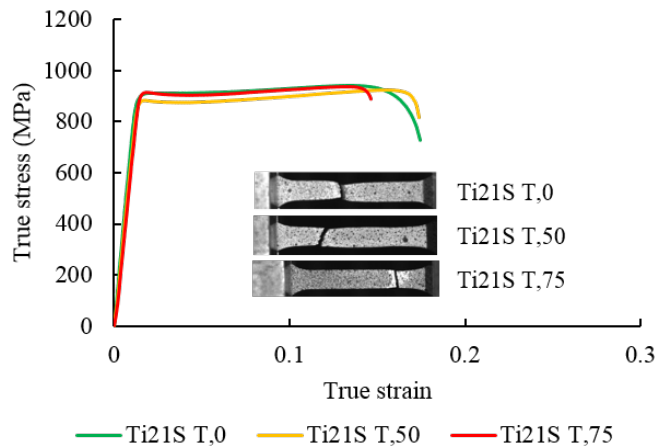
2.4.1 Tensile results of Ti21S and Ti5553 alloys

True stress - true strain curves of Ti21S L and Ti21S T with different rolling reduction rates are plotted in Figure 2.16. The tensile test shows that the specimen

Ti21S L,0 has the largest elongation. With the increase of the reduction rate, the elongation decreases. The difference of elongations in T direction is not evident. Young's modulus and yield strength for these curves are very close. From the fracture images of the tensile specimens, a clear necking is observed for Ti21S 0 whatever the direction. There is no evident necking for Ti21S 50 and Ti21S 75. It demonstrates that with the increasing of the rolling reduction rate, the total deformation reduces. This may have a negative effect on the formability of the material.



(a) Ti21S L

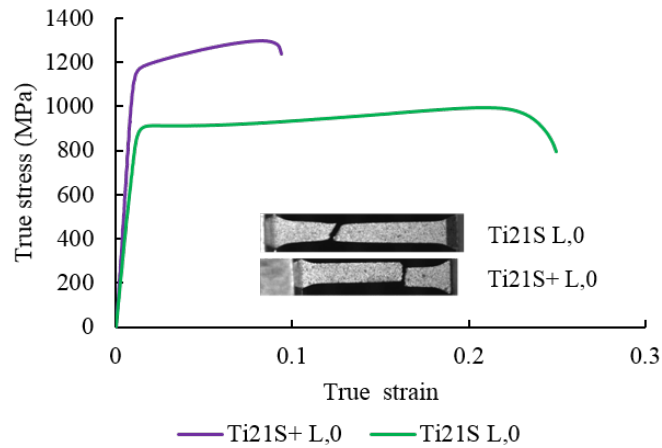


(b) Ti21S T

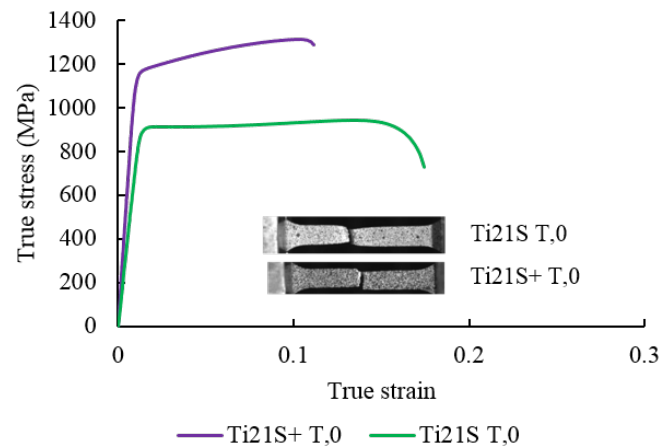
Figure 2.16: Comparison of tensile curves of Ti21S alloys: (a) L direction, (b) T direction

True stress - true strain curves of Ti21S 0 and Ti21S+ 0 for different tensile directions are plotted and compared in Figure 2.17. These two materials have very different mechanical behaviors. After the aging process, Ti21S+ 0 specimen shows a significant increase in tensile strength compared to the Ti21S 0. But as

compensation, the elongation is reduced. The images of fractured specimens in Fig 2.17 show that there is merely no necking near the tensile crack for Ti21S+, while necking appears in Ti21S 0 specimens. The cracks are also perpendicular to the rolling direction for Ti21S+ specimens. All these features of Ti21S+ are due to the well-known hardening effect and embrittling effect of α phase precipitation [159].



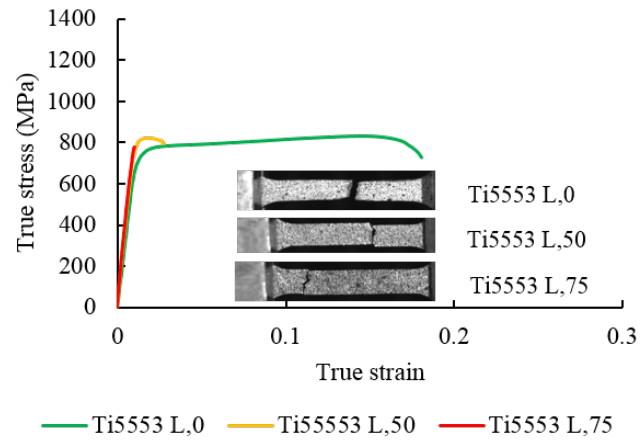
(a) Ti21S+ L



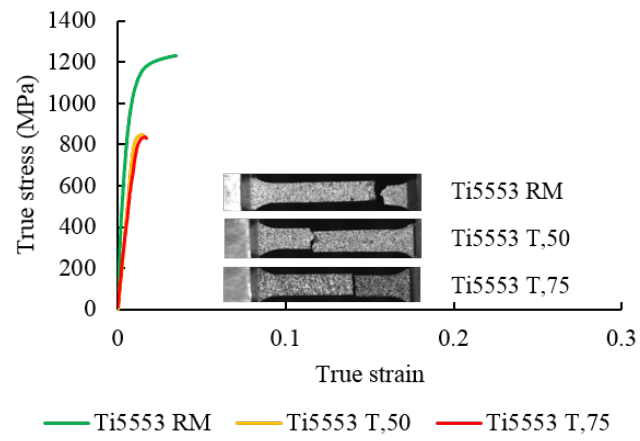
(b) Ti21S+ T

Figure 2.17: Comparison of tensile curves of Ti21S 0 and Ti21S+ 0: (a) L direction, (b) T direction

Similarly, true stress - true strain curves of Ti5553 alloys are shown in Figure 2.18. The tensile result of Ti5553 shows that all the ultimate tensile strength are close, while the one of Ti5553 RM is much higher. Poor elongations are observed. This brittle behavior will certainly affect the formability. The raw material of Ti5553 RM may have α precipitates which can explain its behaviour, similar to the tensile behavior of Ti21S+.



(a) Ti5553 L



(b) Ti5553 T

Figure 2.18: Comparison of tensile curve of Ti5553 alloys: (a) L direction, (b) T direction

The Young's modulus (E), elongation (A), ultimate tensile strength (UTS), yield strength (YS), and their standard deviations ($\bar{\sigma}$) of Ti21S and Ti5553 alloys are listed in Table 2.3 and Table 2.4.

Table 2.3: Mechanical properties of Ti21S and Ti5553 alloys (1 of 2)

Specimen	E/GPa	$\bar{\sigma}(E)/\text{GPa}$	$A/\%$	$\bar{\sigma}(A)/\%$
Ti21S L,0	75	2.8	27.8	1.7
Ti21S L,50	70	2.7	20.6	3.6
Ti21S L,75	68	1.0	16.2	2.1
Ti21S T,0	73	1.5	19.3	1.5
Ti21S T,50	71	2.3	16.3	2.7
Ti21S T,75	65	2.1	10.0	1.4
Ti21S+ L,0	122	3.5	9.9	0.8
Ti21S+ T,0	113	3.6	9.0	1.7
Ti5553 L,0	68	3.6	19.7	1.9
Ti5553 L,50	78	6.1	3.7	1.4
Ti5553 L,75	88	2.0	1.1	0.1
Ti5553 RM	114	12.3	4.0	0.9
Ti5553 T,50	88	2.1	2.0	0.5
Ti5553 T,75	74	4.5	1.8	0.0

For Ti21S, YS , UTS , as well as A along L direction are higher than T direction, except for Young's modulus, which is nearly the same for both directions. Texture is responsible for this anisotropy. The texture components of Ti21S are not exactly the same but their orientations are very close. The evolution of the texture can be regarded as $\{465\}\langle 05\bar{6}\rangle$ (Ti21S 0) to $\{114\}\langle \bar{1}7\bar{2}\rangle$ (Ti21S 50) and then to $\{238\}\langle \bar{2}4\bar{1}\rangle$ (Ti21S 50). The texture component $\{311\}\langle 12\bar{5}\rangle$ is also rising during this procedure. They give good mechanical properties in the rolling direction and fair in the transverse direction.

On the contrary, Ti21S+ 0 specimens do not show this anisotropy evidently. The difference in the mechanical properties of Ti21S+ 0 is very limited, although they have the same texture components as Ti21S 0. The precipitation of α phase in Ti21S+ 0 dramatically improves the mechanical properties, which covered the effect of texture on the anisotropy. The ultimate tensile strength of Ti21S+ 0 is much higher than Ti21S 0. It increases from 989 MPa to 1304 MPa (L direction), or from 890 MPa to 1300 MPa (T direction). Young's modulus also increases evidently. But the elongation of Ti21S+ 0 is less than 10%, while Ti21S 0 has elongation of 27% and 19% in L and T directions.

Ti5553 L,0 has lower YS than the other conditions, due to its large grain size.

Table 2.4: Mechanical properties of Ti21S and Ti5553 alloys (2 of 2)

Specimen	UTS/MPa	$\bar{\sigma}(UTS)/MPa$	YS/MPa	$\bar{\sigma}(YS)/MPa$
Ti21S L,0	989	19	894	24
Ti21S L,50	945	32	889	27
Ti21S L,75	878	17	852	21
Ti21S T,0	923	12	875	14
Ti21S T,50	890	29	867	28
Ti21S T,75	794	19	792	21
Ti21S+ L,0	1304	7	1167	3
Ti21S+ T,0	1300	23	1176	26
Ti5553 L,0	825	21	711	9
Ti5553 L,50	844	16	814	18
Ti5553 L,75	807	37	807	37
Ti5553 RM	1230	1	1155	80
Ti5553 T,50	843	7	830	9
Ti5553 T,75	846	17	815	19

The elongation A of Ti5553 is extremely low except for Ti5553 L,0. The effect of texture on the Ti5553 alloys is not evident.

When compared to the two materials with the same treatment, Ti21S alloys have larger YS , UTS , and A than Ti5553 alloys in general. The different percentage of β stabilizers makes the difference on the mechanical behavior of titanium alloys.

2.4.2 Forming limit points and r -values of Ti21S and Ti5553 alloys

Following the procedure presented in section 2.2.3 and 2.2.4, the results of forming limit points and r -values of Ti21S, Ti21S+ and Ti5553 are plotted in Figure 2.19.

For uniaxial stretching, the formability of Ti21S alloys decreases with the increase of the reduction rate. The major limit strain of Ti21S alloys with 75% of rolling reduction is nearly half of the one of Ti21S alloys without rolling. The r -values of Ti21S L with three different rolling reduction rates are very close.

The texture component $\{112\}\langle 1\bar{1}0\rangle$ is known to be good for formability (Table 1.5 in Chapter 1) [76]. In the specimen with the best formability, Ti21S L,0, the $\{112\}\langle 02\bar{1}\rangle$ texture component have the same $\{112\}$ //sheet plane with $\{112\}\langle 1\bar{1}0\rangle$. This group of textures increases the formability.

The formability from the T direction is generally lower than the one from L

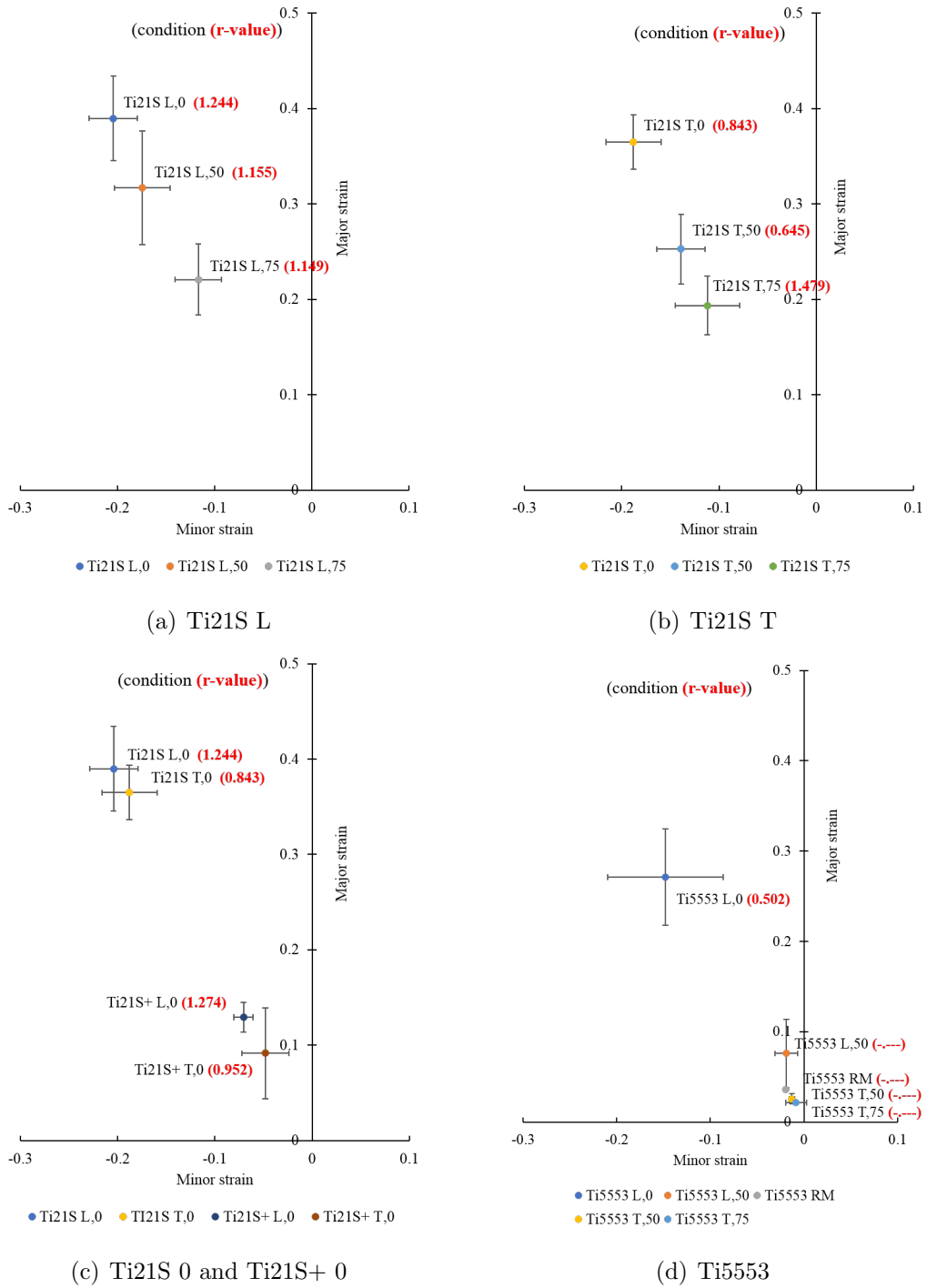


Figure 2.19: Average forming limit points and r -values for Ti21S and Ti5553 alloys

direction, except for Ti21S 75. For a specimen, variations of r -value and formability can be linked. The r -value reflects the property of the resistance to thinning. The r -value which is less than 1 means that the material is easy to thin, which makes it vulnerable when forming. This can explain that the forming limit points from the tensile test along the transverse direction are lower than the points from the rolling direction for the same conditions.

The Ti21S+ has excellent tensile strength but poor formability. This is mainly due to the α phase precipitation from the β matrix. The material is strengthened but the ductility is sacrificed. This microstructure is not suitable for forming.

The results of Ti5553 alloys exhibit extremely low formability, except for Ti5553 L,0. The Ti5553 with 50% and 75% rolling reduction rates and raw materials have very poor formability. Similarly, a very low elongation at rupture was measured during the tensile test. Comparing the forming limit points of Ti5553 L,0 and Ti21S L,0, Ti5553 L,0 exhibits a lower r -value and formability.

The texture component $\{110\}\langle 1\bar{1}2\rangle$ in Ti5553 75 has the similar $\{110\}$ //sheet plane with $\{110\}\langle 001\rangle$, which is bad for formability (Table 1.2 [76]).

2.4.3 Conclusions

From the results of the tensile tests of Ti21S and Ti5553 alloys we can draw some conclusions:

1. With the increase of the rolling reduction rate, both E and UTS decreases. It also reduces the ductility of the material. The tensile strength along the longitudinal direction is higher than the one along the transverse direction. r -value of rolling directions is higher than transverse direction, except for Ti21S 75. The r -values can be linked to the formability in the different directions of a specimen. The effect of texture on the mechanical properties of Ti21S and Ti5553 alloys is not so evident.

2. From the values of the forming limit points, the rolling process reduce the formability of materials. The higher the reduction rate, the worse the formability. For uniaxial stretching, the formability along the longitudinal direction is better than in transversal direction also with an exception for Ti21S 75. The Ti5553 alloys show very low formability, except Ti5553 L,0. This reduction of formability has a relationship with deformation. The $\{112\}$ //sheet plane and $\{110\}$ //sheet plane can explain some effects of texture on the formability on Ti21S 0 and Ti5553 75.

3. The alloy with heat treatment at 650°C for 8 hours (Ti21S+), cooled in the furnace has a significant increase of Young's modulus and ultimate tensile strength due to α phase precipitation. Ductility is reduced which makes the formability of Ti21S+ worse than the Ti21S. The effect of aging on the mechanical properties

can cover the effect of textures.

2.5 Fracture analysis of Ti21S and Ti5553 alloys

SEM observations are conducted on the fracture surface of the tensile specimens in each conditions.

2.5.1 Fractographs of Ti21S

Fractographs of each condition of Ti21S are shown in Figures 2.20 to 2.22. Each group has two kinds of tensile directions: 0° and 90° from the rolling direction. Every specimen exhibits a low magnification image and a high magnification image.

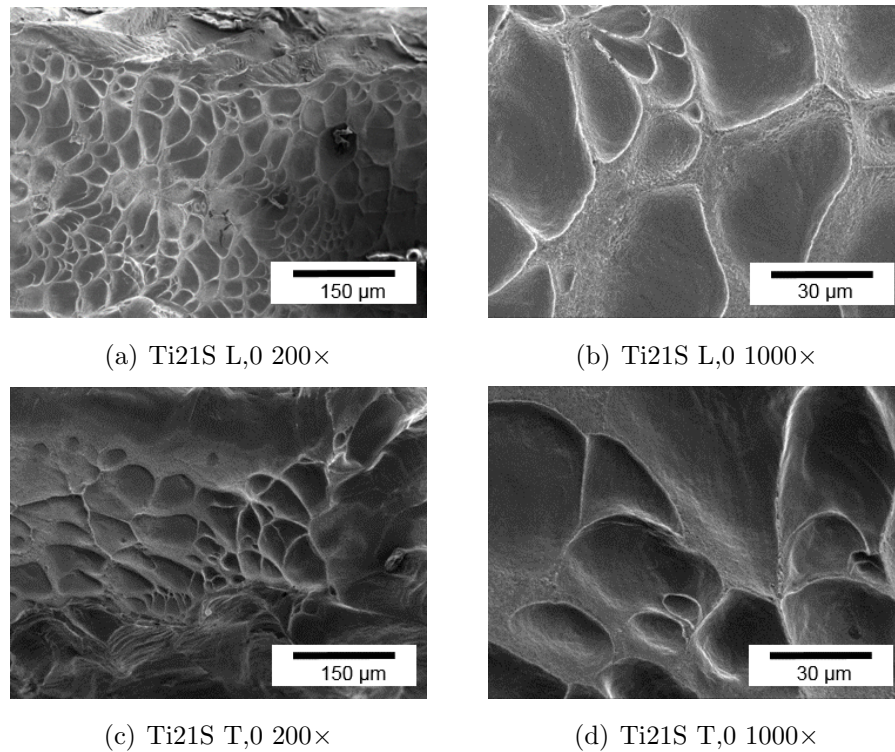


Figure 2.20: Ti21S 0 SEM images

The fractograph of Ti21S 0 shows a fracture with large size dimples. The fracture surface in the dimples is very flat. The large size of dimples reflects that the nucleation sites are very few.

The Ti21S 50 shows a rupture with fewer dimples. Furthermore, this specimen exhibits a part of the river pattern. This is the main feature of cleavage fracture.

The fractograph of Ti21S 75 rarely has dimples. The surface exhibits a dominated cleavage fracture. The appearance of dimples demonstrates the ability of plastic deformation to develop. The tendency of dimples to disappear for Ti21S

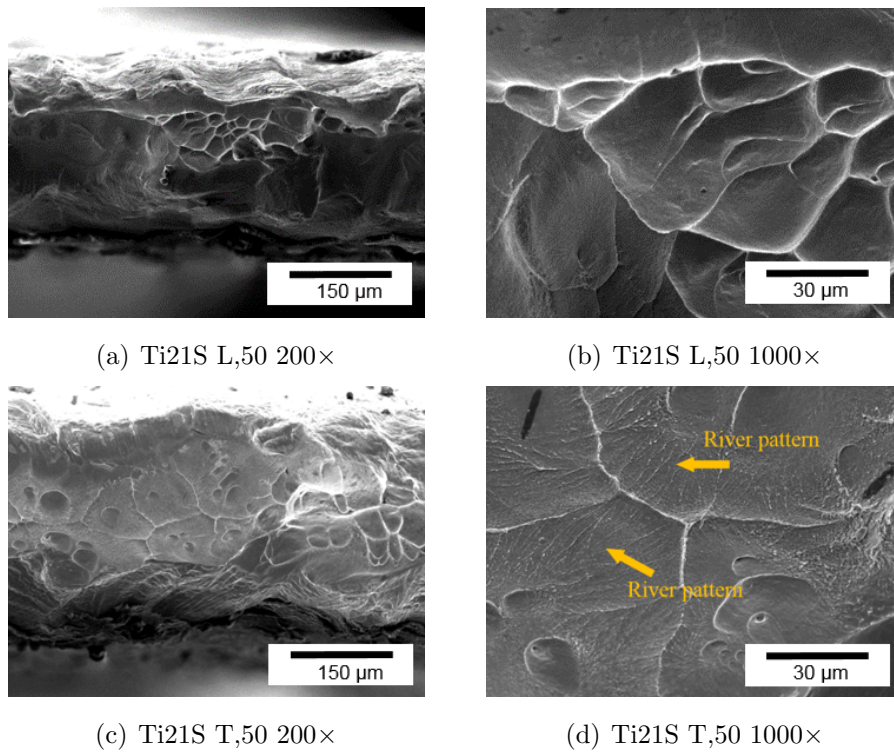


Figure 2.21: Ti21S 50 SEM images

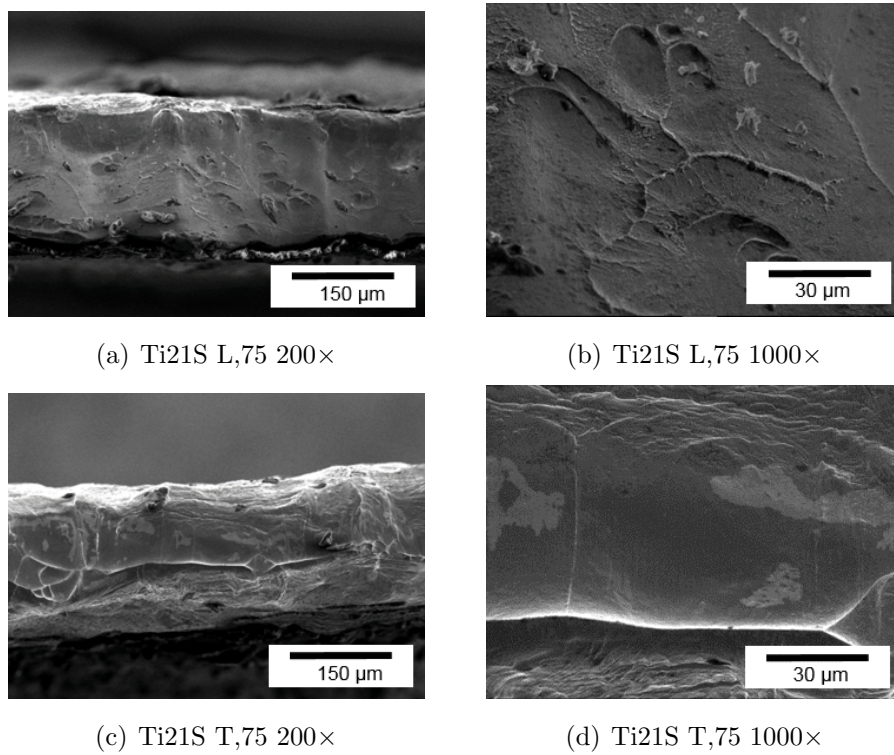


Figure 2.22: Ti21S 75 SEM images

from 0% to 75% of rolling reduction rates is linked to the loss of formability. Fracture surface of Ti21S 0 along the rolling direction has more dimples than the transverse direction. This demonstrates that the elongation of Ti21S L,0 is higher than Ti21S T,0. The difference of fractograph between different directions of Ti21S 50 and Ti21S 75 is not evident.

2.5.2 Fractographs of Ti21S+

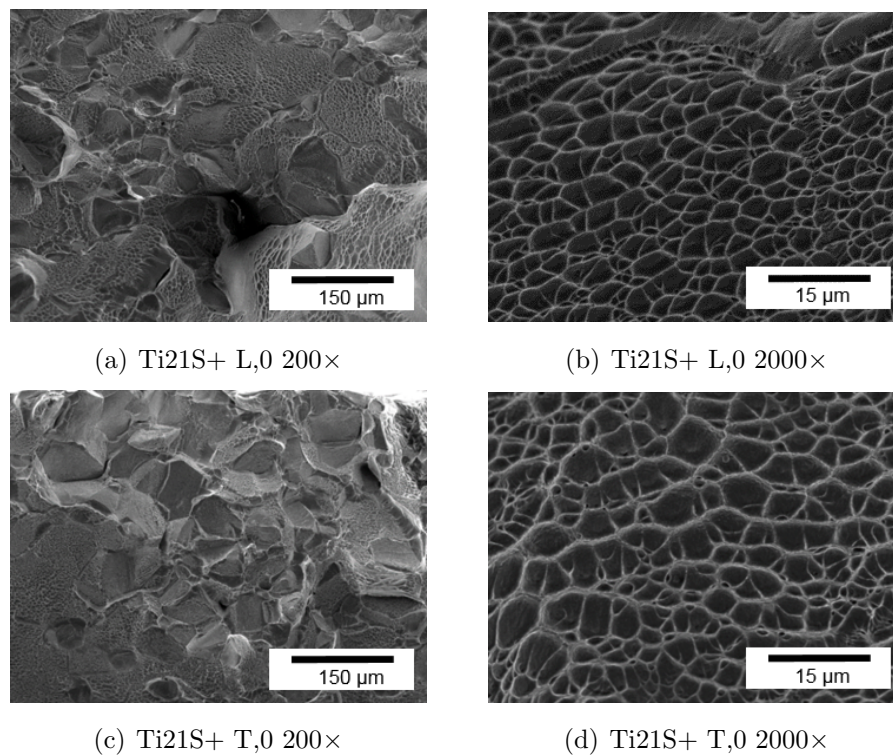


Figure 2.23: Ti21S+ 0 SEM images

The fracture surface of Ti21S+ shows a mix-mode fracture. Low-magnification (200×) shows a grainy appearance, where decohesion occurs, because of α precipitates in the grain boundaries. High-magnification SEM shows shallow dimples on the facets, which is a ductile fracture. The dimples contribute to the plastic part deformation, which reflects on the higher work hardening on the tensile curve of Ti21S+ than Ti21S. But because of the existence of α and β phases, the interface of these two phases can be a good zone for voids gathering, crack nucleation and becomes the path of crack propagation. The zone that has shallow dimples is an evidence of the transgranular fracture. This significantly restricts the plastic deformation, furthermore, the formability. That is why the tensile curve of Ti21S+ has high strength, high hardening rate but low elongation.

2.5.3 Fractographs of Ti5553

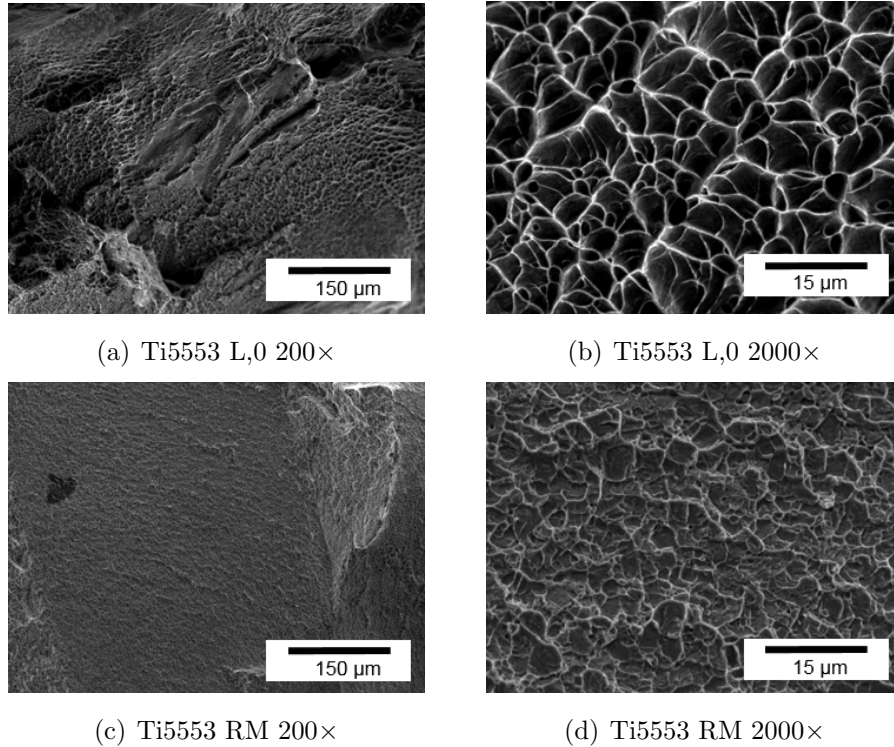


Figure 2.24: Ti5553 SEM images

Ti5553 L,0 shows a ductile fracture with fine dimples, which leads to good ductility. Ti5553 RM shows transgranular fracture. The grains have very limited plastic deformation. Similar phenomena are found in titanium alloys with low formability [145]. Due to the very low plastic deformation of Ti5553 50 and Ti5553 75, the fractographs of them are not analyzed.

2.5.4 Conclusions

Fractography of Ti21S 0 shows a fracture with a flat surface and large size dimples, revealing a transgranular fracture. With the increase of rolling reduction rates, the dimples decreases on the fracture surface.

The fracture mode of Ti21S+ is a mixed-mode with intergranular fracture and ductile fracture. Very small and shallow dimples with some visible grains can be observed. This change in fracture mechanism after aging treatment is clearly due to the precipitation of α phase.

Ti5553 L,0 has many fine dimples and presents good ductility.

2.6 Conclusions

The solution treatment leads to recrystallization of specimens after cold rolling. The reduction rate affects the final texture components. The effect of these texture components on the mechanical properties is limited, because they are not so concentrated in some specimens.

For Ti21S, r_0 is higher than r_{90} except for Ti21S 75. This also makes the formability from the longitudinal direction is higher than the transverse direction.

The formability of Ti21S is better than Ti21S+. The aging procedure after solution treatment generates fine α precipitation. This is the main reason which affects the mechanical behavior of β metastable titanium alloys. This kind of treatment increases the ultimate tensile strength evidently and reduces elongation. It reduces the formability dramatically. The mixed fracture mode (intergranular and ductile) of these specimens explains this phenomenon.

The formability of Ti21S is better than Ti5553. They have similar phases but different textures. Ti21S shows a low intensity of texture while Ti5553 has a stronger texture. These textures make a low r -value of Ti5553 0 (0.502), that is bad for formability. The textures are affected by the rolling procedures, then affecting the mechanical properties of Ti21S and Ti5553.

One forming limit point in uniaxial stretching condition is not enough to evaluate the formability of a material. The whole FLC needs to be plotted to have a global comparison between microstructures and formability, that will be done in the next Chapters.

Chapter 3

Prediction of forming limits at necking

3.1 Introduction

Uniaxial tensile tests with different microstructures provided only one point for each microstructure on the Forming Limit Diagram for the corresponding strain path. From these first observations, one can draw some basic conclusions about the effect of microstructures on formability. But the complete FLCs are not identified.

In order to plot whole FLCs, predictive models are an interesting alternative while experimental method is costly and time consuming. The deformation of a reliable predictive model is linked to the choice of the material constitutive model and instability criterion.

In this chapter, the widely used M-K model is introduced. A finite element (FE) M-K model is proposed to predict the forming limit curve for different microstructures. Previous uniaxial tests are used to identify the parameters of the constitutive model and to calibrate the imperfection factor of the M-K model. Predicted FLCs of Ti21S and Ti5553 alloys are then plotted. Finally, the predicted FLCs with different rolling reduction rates of Ti21S alloys are compared. The effect of anisotropy on the predicted FLCs of Ti21S alloys is also studied.

3.2 Numerical M-K model

3.2.1 Definition of the FE M-K model

A finite element M-K model is built with the ABAQUS software by referring to the model proposed by C. ZHANG [149]. Due to symmetry, only 1/8 of the model is considered, which has 50 mm in length and 50 mm in width totally. The normal thickness is set as 1 mm and the thickness in the groove is adjustable. The width of the groove is 2.5 mm. Different displacements (u, v) are applied on the boundaries, respectively along directions 1 and 2, for simulating different strain paths (Figure 3.1).

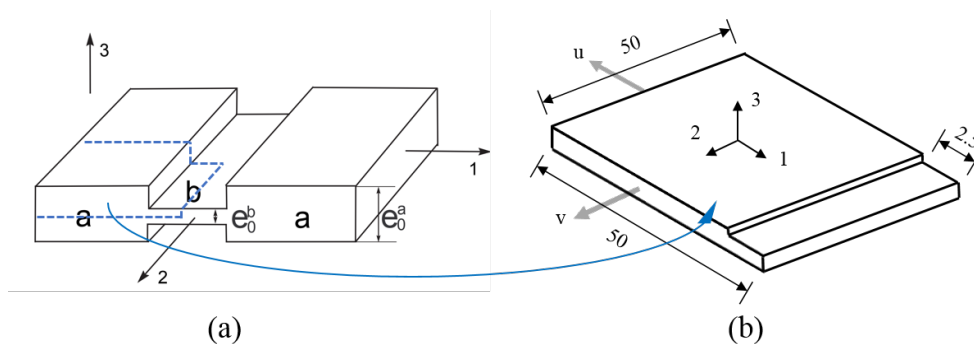


Figure 3.1: (a) M-K analytical model and (b) 1/8 of the M-K model and its dimensions

This model is meshed by hexahedral elements with an approximate global size of 1 mm to guarantee the accuracy of the simulation (see Figure 3.2). This size of the mesh is decided by testing the evolution of the equivalent strain where the smaller element size have a similar results. As shown in Figure 3.2, an element in the zone with the normal thickness e^a is designated "Element A" and an element in the imperfection zone with the reduced thickness e^b is called "Element B". As the same in the M-K theory, the numerical imperfection can also be quantified by an initial imperfection value f_0 (see in equation 3.1):

$$f_0 = \frac{e_0^b}{e_0^a} \quad (3.1)$$

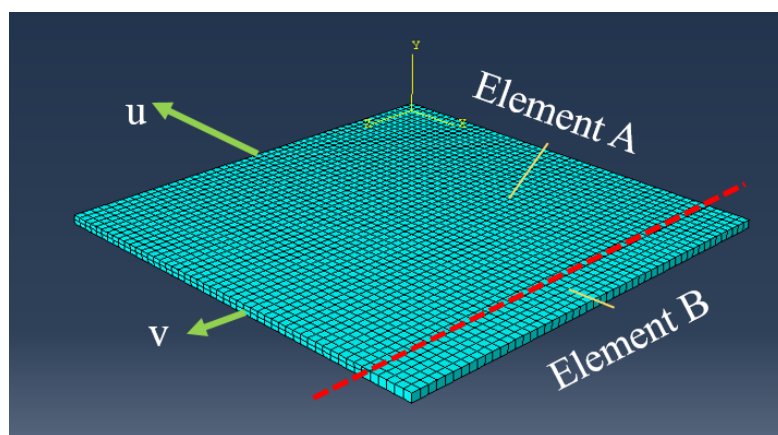


Figure 3.2: Finite element model of the M-K model

The properties of materials used in these FE simulations are based on experimental uniaxial tensile test results presented in Chapter 2. For each material, Young's modulus, Poisson's ratio and identified hardening laws are introduced.

At the end of the simulation, the temporal evolution of equivalent plastic strain, major strain and minor strain for Element A and Element B are exported. The evolution of the equivalent plastic strain for Element A and Element B for Ti21S L,0 are plotted in Figure 3.3 as an example.

3.2.2 Failure criterion of M-K model

During the deformation, the evolution of equivalent stress and strain in zone a and zone b are different. The equivalent stress and strain must meet the static equilibrium conditions and geometric coordination conditions, which makes the stress in zone b larger than the stress in zone a. The evolution of stress and strain in zone b will accelerate when necking. Choosing a suitable failure criterion to identify this necking is important in this work.

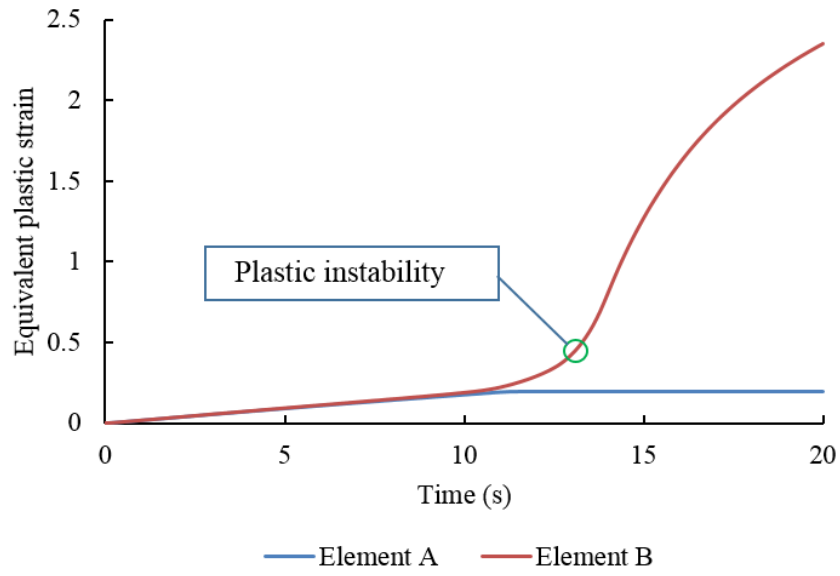


Figure 3.3: Identify the necking of Ti21S L,0

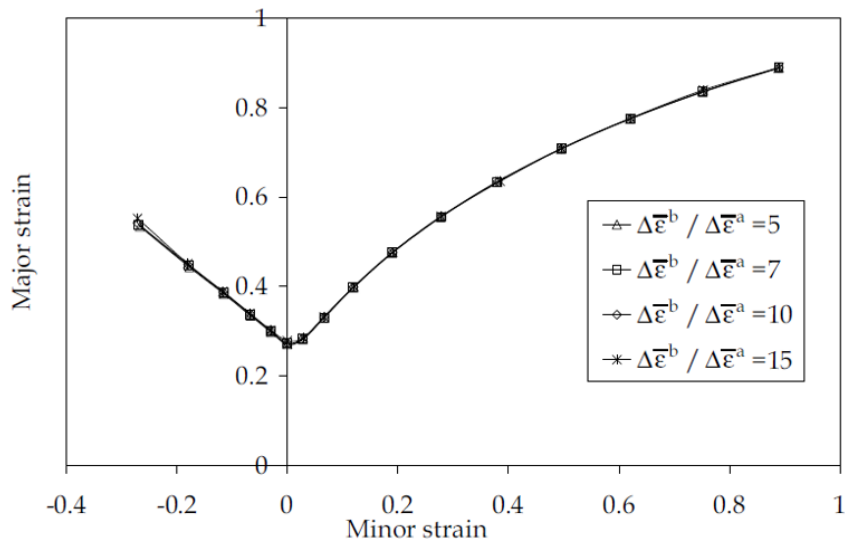


Figure 3.4: The effect of different critical increment ratios ($\Delta\bar{\epsilon}^b / \Delta\bar{\epsilon}^a$) on predicted FLC of aluminium alloy AA6111-T4 [160]

There are various failure criteria. Marciniak-Kuczynski proposed that the necking happens when the real-time ratio of the thickness (e^b/e^a) becomes lower than a critical value [128], the result is very sensitive to this critical value. Another method is that when the ratio of the strain increment in the zone b is 7 times than in zone a ($\Delta\bar{\varepsilon}^b/\Delta\bar{\varepsilon}^a > 7$), the necking happens [161]. The influence of the value of the critical ratio on the forming limits is very low (Figure 3.4). The predicted FLCs from different ratios are coincident, which indicate that the effect of critical value from 5 to 15 on the predicted FLC is not obvious. Therefore, the critical value 7 in the studied range is chosen in this work.

The method to determine the limit strains is as follows:

1. Calculate the increment of the equivalent plastic strain of Element A and Element B.
2. Find out the moment whose increment in Element B is firstly larger than 7 times the increment in Element A (see plastic instability point in Figure 3.3).
3. The major strain and minor strain at this moment in Element A are the forming limit strains, which correspond to one point of the forming limit diagram for the considered strain path.

In the predicting model, different strain paths are calculated by changing the displacement ratio in the two different directions 2 and 1 respectively. This ratio is defined by S :

$$S = \frac{v}{u} \quad (3.2)$$

In order to cover strain states from equibiaxial stretching to uniaxial stretching, the ratio S is changed.

3.2.3 Comparison of numerical and analytical predictions of forming limits from M-K model

For many years, the analytical M-K model has been widely used for the prediction of forming limits of metal sheets. Therefore, a procedure of validation of the finite element model by the analytical model is conducted.

This work refers to the results of the M-K theory by C. ZHANG based on an analytical M-K model [162]. The same material of AA6056 is chosen in our simulation because the analytical results and the mechanical properties are already provided. For the elastic part, Young's modulus $E=70500$ MPa, Poisson's ratio $\nu=0.33$. For the hardening, a Swift's law is considered:

$$\bar{\sigma}^k = K(\bar{\varepsilon}_0 + \bar{\varepsilon}^k)^n \quad (3.3)$$

The parameters of this function are $K=567.28$ MPa, $\bar{\varepsilon}_0=0.0029$, and $n=0.1939$.

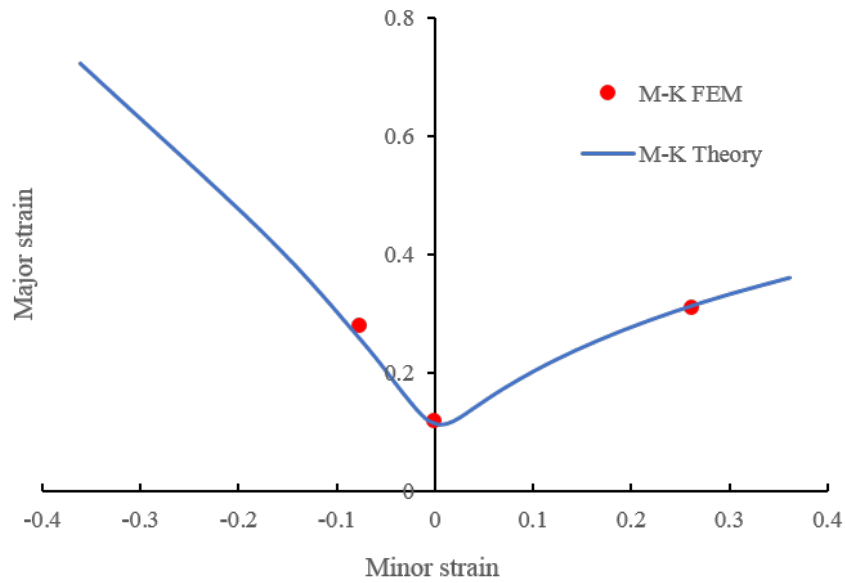


Figure 3.5: Validation of finite element model by comparing numerical and analytical results

Figure 3.5 shows a comparison of the predicting result between the proposed FE model and the analytical M-K model. Three strain paths which correspond to uniaxial tension, plane strain and biaxial tension are applied in FE model. From the results of the simulation, the two methods fit well. The FE model can be a reliable method for the prediction of forming limits. Because the numerical M-K model is easy to implement, it has been chosen for study in this work.

3.2.4 Effect of the initial imperfection factor f_0

The imperfection factor f_0 is a very important factor that has a great effect on the predicted FLC. It can not be detected directly by experiments. However, one forming limit point of each condition has been already plotted through the experiments of the tensile tests in Chapter 2. So the imperfection factor (defect) is used to calibrate the M-K model from this experimental point. The corresponding imperfection factor (f_0) represents the defects of the microstructure of a material [149].

C. ZHANG has studied the effect of the imperfection factor f_0 on the predicted FLC of AA6056 aluminium alloys by simulation with numerical M-K model with four different factors: 0.99, 0.995, 0.9975 and 0.9985. Figure 3.6 shows the result of this comparison [162].

As shown in Figure 3.6, there is an evident effect of imperfection factor f_0 on the formability. With the decrease of the imperfection factor f_0 , a decrease in the

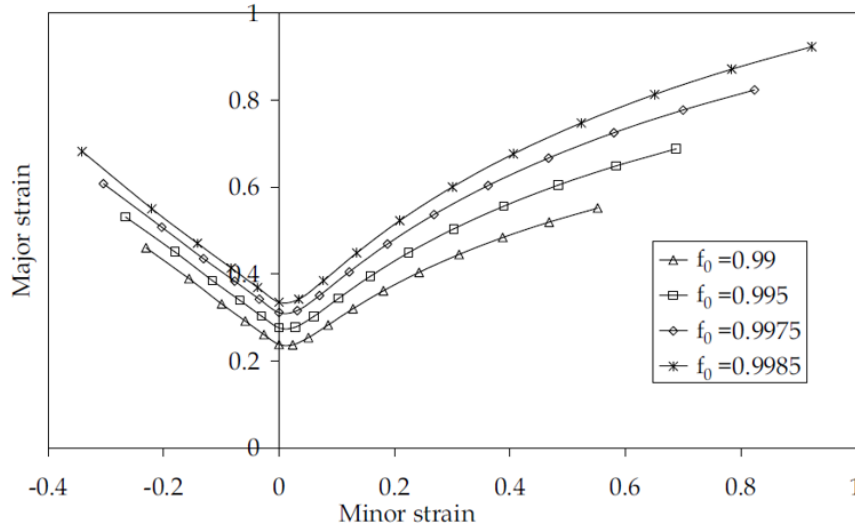


Figure 3.6: Effect of different initial imperfection f_0 on predicted forming limit curve of AA6056 aluminium alloy [162]

formability for every deformation condition can be seen. The level of FLC is very sensitive to the change of the imperfection factor f_0 .

3.2.5 Identification of Ludwik's hardening law

Ludwik's law is calibrated on true stress - plastic strain curves for Ti21S L,0, Ti21S L,50, Ti21S L,75, Ti21S+ L,0 and Ti5553 L,0. Considering the perfect plastic behavior (horizontal plateau) that appears between the end of the elastic domain and the beginning of the hardening for some specimens, the hardening curve is calibrated in a range of deformation between $0.5\varepsilon_m$ to ε_m , where ε_m is the plastic strain corresponding to the maximum stress σ_m . This fitting can make material a better behavior in simulation. This range is chosen because the characterized behavior of the material is just before necking. There have no influence with the difference of the curve at small strain. Figure 3.7 shows this calibration stage applied to the Ti21S L,0 as an example.

Then, the $\sigma_0=750$ MPa is applied for Ti21S L,0, Ti21S L,50 and Ti21S L,75, 1150 MPa for Ti21S+ L,0 and 700 MPa for Ti5553 L,0, according to their initial yield stress from uniaxial tensile tests. 750 MPa is set for all the Ti21S specimens to allow easy comparison. These values are lower than the yield strength of correspondent material just for better fitting. K , n are identified by linearization of the Ludwik's law as follows:

$$\ln(\bar{\sigma} - \sigma_0) = n \ln \bar{\varepsilon}_p + \ln K \quad (3.4)$$

A straight tendency line is plotted from the experimental curve $\ln(\sigma - \sigma_0)$ versus

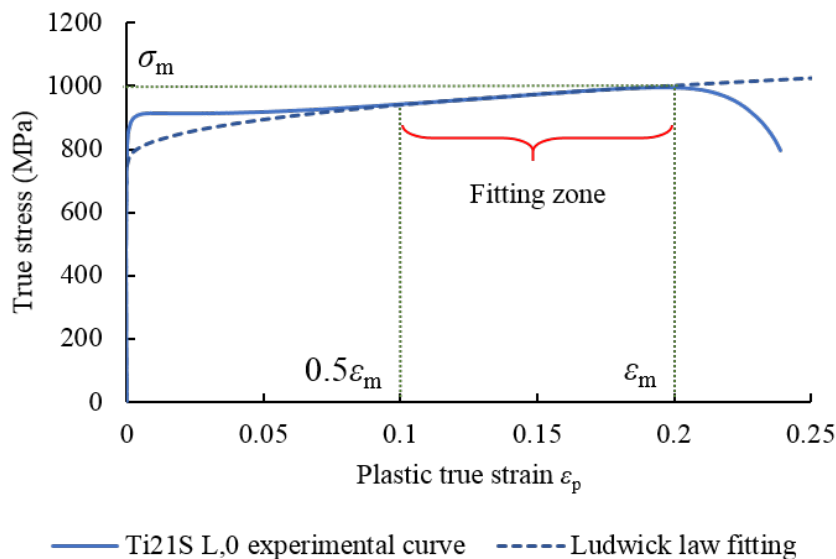


Figure 3.7: Definition of fitting zone

$\ln \varepsilon_p$. The n and K are respectively obtained from the slope and the intercept of the tendency line.

The fitting curve and the tendency line are shown in Figure 3.8. The calculated fitting parameters for Ludwik's law are listed in Table 3.1. These fitting data will be used in the following simulation in Abaqus.

Table 3.1: Fitting parameters by Ludwik's law

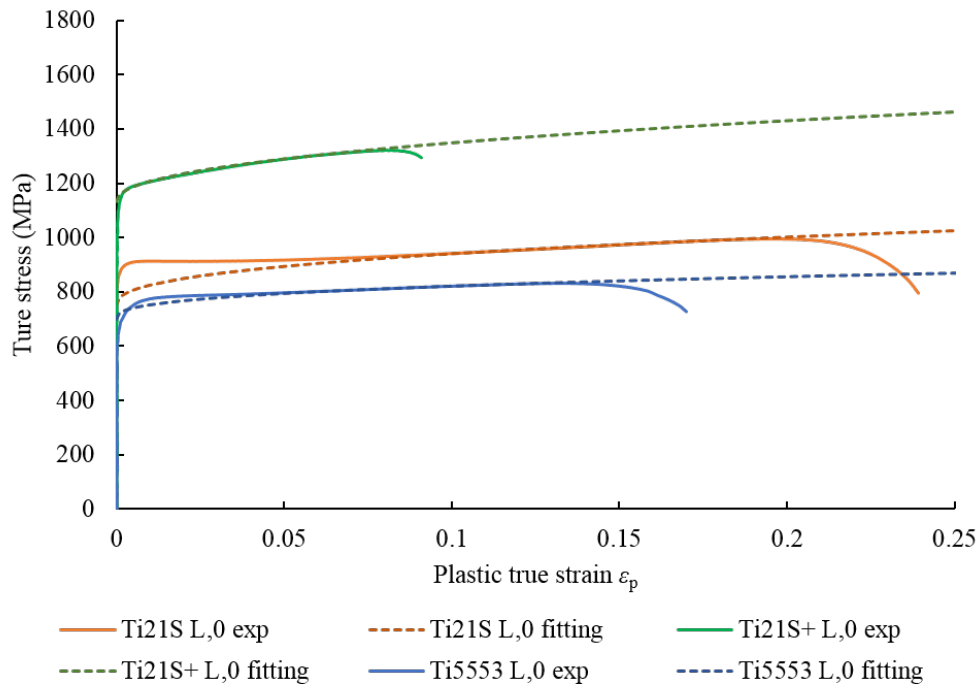
Specimens	σ_0 (MPa)	K (MPa)	n
Ti21S L,0	750	481	0.4
Ti21S+ L,0	1150	628	0.46
Ti5553 L,0	700	278	0.36

With the same method, the fitting on the Ti21S L,50, Ti21S L,75 is also conducted to give convenience on comparing the effect of rolling reduction rates with Ti21S L,0 on the predicted FLCs. The results are shown in Figure 3.9. The calculated fitting parameters for Ludwik's law are listed in Table 3.2.

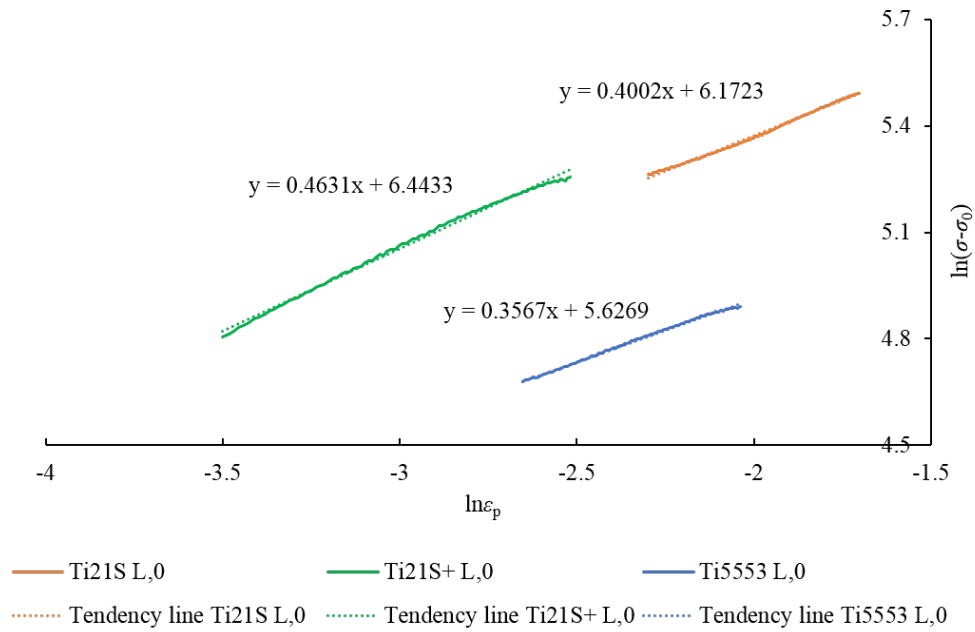
The fitting results show that fitting with Ludwik's law has good agreement with the hardening part of the experimental curve. The mechanical behavior of these materials are kept the same in the simulation of following parts.

3.2.6 Conclusions

A finite element numerical M-K model is proposed and a failure criterion of strain increment in the zone b 7 times larger than in zone a is applied. This numerical

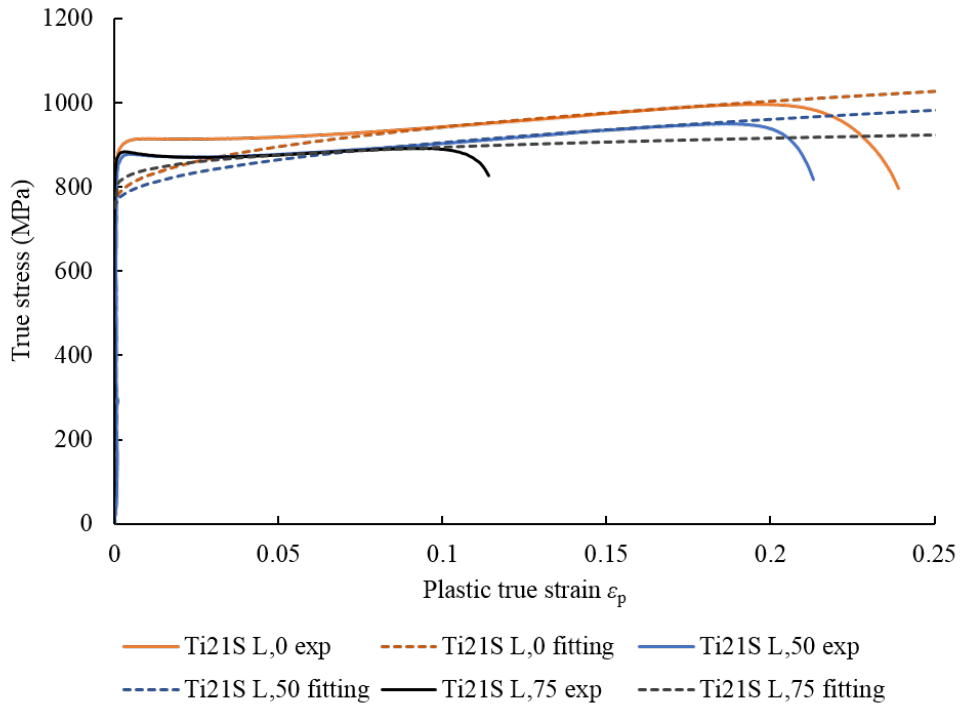


(a) Fitting curve with Ti21S L,0, Ti21S+ L,0 and Ti5553 L,0

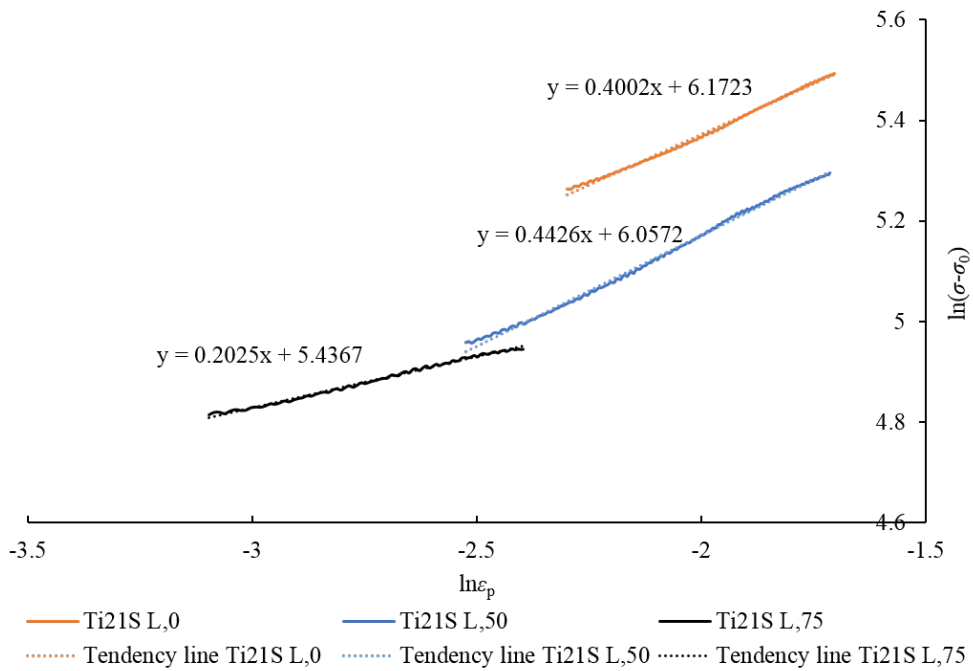


(b) Tendency line with Ti21S L,0, Ti21S+ L,0 and Ti5553 L,0

Figure 3.8: The fitting of Ti21S L,0, Ti21S+ L,0 and Ti5553 L,0



(a) Fitting curve with Ti21S L,0, Ti21S L,50 and Ti21S L,75



(b) Tendency line with Ti21S L,0, Ti21S L,50 and Ti21S L,75

Figure 3.9: The fitting of Ti21S L,0, Ti21S L,50 and Ti21S L,75

Table 3.2: Fitting parameters by Ludwik's law of Ti21S with different rolling reduction rates

Specimens	σ_0 (MPa)	K (MPa)	n
Ti21S L,0	750	481	0.4
Ti21S L,50	750	428	0.44
Ti21S L,75	750	228	0.2

M-K model is validated by analytical M-K model. The initial imperfection factor f_0 has a great effect on the predicted FLC and it can be identified by calibrating the experimental point from uniaxial tensile test. The Ludwik's law can be applied as the hardening law of Ti21S and Ti5553 in simulation.

3.3 Anisotropy characterization of Ti21S

In order to study the effect of anisotropy on the FLC and imperfection factor f_0 , tensile tests on 5 directions of 0° , 22.5° , 45° , 67.5° and 90° to the rolling direction of Ti21S 0 has been conducted. The Lankford coefficients r_0 , $r_{22.5}$, r_{45} , $r_{67.5}$ and r_{90} of Ti21S 0 can be calculated and used to evaluate the anisotropy of the material.

3.3.1 Lankford coefficients of Ti21S 0

Lankford coefficients of Ti21S 0 given in chapter 2 are presented for the five directions in Figure 3.10 for the Ti21S 0.

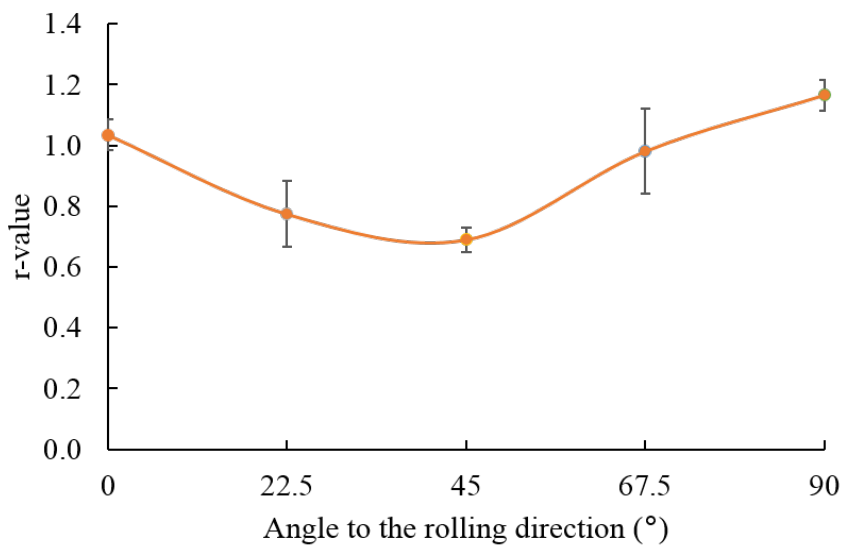


Figure 3.10: r -value of Ti21S 0

This result shows that the r -value in 45° is lower than 0° and 90° . The r -value in 90° is more than 1. It indicates that the strain through the normal direction of the plate is less than the transverse direction. That means the direction of 90° has more resistance to the thinning when deformed. The formability predicted through this direction may be better.

3.3.2 Anisotropy parameters of Ti21S 0

Expressions of anisotropy parameters of Hill48 model R_{11} , R_{12} , R_{22} , R_{13} , R_{23} and R_{33} in function of Lankford coefficients r_0 , r_{45} and r_{90} have been presented in Chapter 1 (Equation 1.4). From these expressions and the Lankford coefficients obtained by uniaxial tensile tests, anisotropy parameters are calculated. Table 3.3 presents these anisotropic parameters for Ti21S 0:

Table 3.3: Anisotropy parameters of Ti21S 0

Parameters	R_{11}	R_{12}	R_{22}	R_{13}	R_{23}	R_{33}
Value	1	1.17	1.03	1	1	1.04

3.3.3 Validating the anisotropy of Ti21S 0 by simulation

In the numerical M-K model, the calculated anisotropy parameters of Ti21S alloys can be added in the plastic property, which is shown in Table 3.3. In order to validate the anisotropy model in Abaqus and the $r_{22.5}$, $r_{67.5}$ values from the experiment, the simulation of a tensile test is conducted in Abaqus. The calculation of r -value is similar to the method on the tensile test in Chapter 2. The finite element model is built as in Figure 3.11. One edge is fixed and a displacement is imposed on the opposite edge.

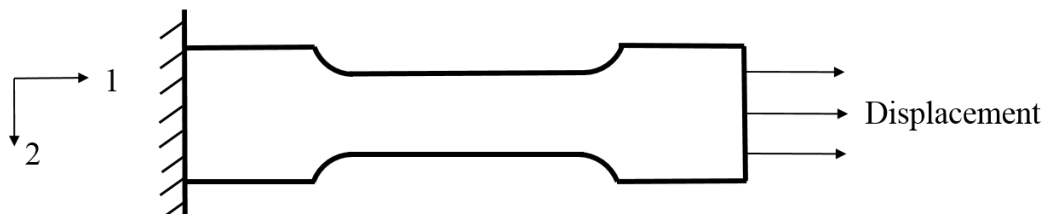
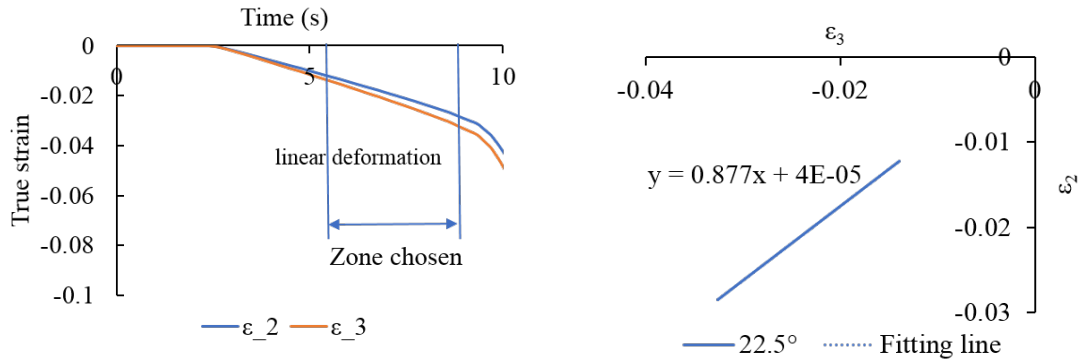


Figure 3.11: Finite model for validation r -value of Ti21S 0

The evolution of strain components ε_2 and ε_3 of an element in the necking zone is exported and plotted in Figure 3.12(a). Then the zone with linear deformation is chosen. A relationship between ε_2 and ε_3 can be plotted. Finally, a straight

tendency line fits this curve. The slope of this tendency line is the r -value (Figure 3.12(b)).



(a) The choosing of calculating zone during the evolution of ε_2 and ε_3 of $22,5^\circ$

(b) The calculation of r -value of $22,5^\circ$

Figure 3.12: Method of calculating r -value in simulation

The comparison of the results of r -value from simulation and experiments are shown in Figure 3.13.

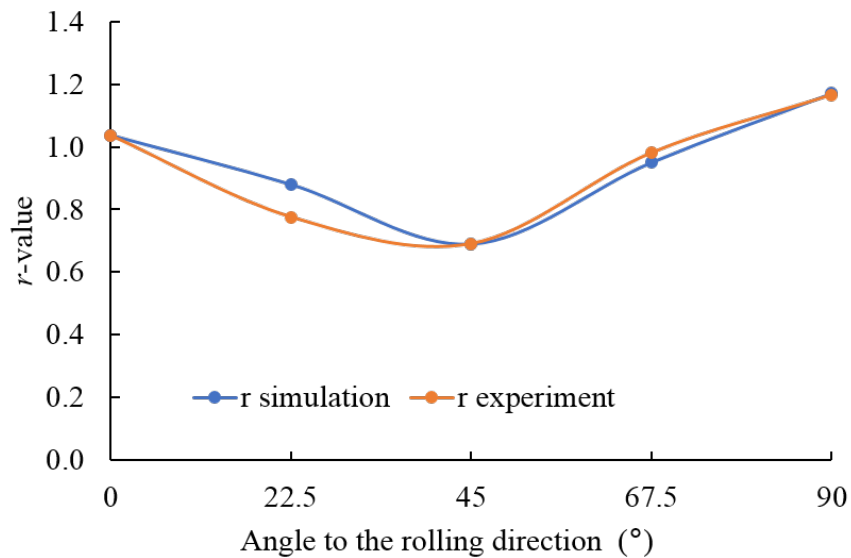


Figure 3.13: Comparison of the r -value of Ti21S 0 from simulation and experiment

From the results of the experimental and the simulation r -values, the anisotropy model is validated in Abaqus. The measured Lankford coefficients $r_{22.5}$ and $r_{67.5}$ are close to the predicted one. It confirms that the Hill48 criterion can be used to model the anisotropic behaviour of the considered materials.

3.4 Predicted FLCs of Ti21S, Ti21S+ and Ti5553

After the validation of the finite element M-K model, the predicted FLCs of the materials can be plotted with acceptable precision. Since the Ti21S 0 can have different anisotropic parameters in directions L and T, their predicted FLCs may be different because of the different material anisotropy parameters adapted in Ti21S L,0 and Ti21S T,0. Moreover, the isotropy material parameters can be applied on the predicted FLCs of Ti21S, Ti21S+ and Ti5553. The FLC of Ti21S+ L,0 can be predicted to study the effect of the precipitated α phase. The effect of the rolling reduction rates on the predicted FLC can be studied with the specimens Ti21S L,0, Ti21S L,50 and Ti21S L,75. The material mechanical properties in isotropy can be applied because the comparison is only between the rolling reduction rates. For Ti5553 alloys, the specimen of Ti5553 50, Ti5553 75 and Ti5553 RM have very low formability, the predicted FLC only on Ti5553 L,0 is conducted for this material.

3.4.1 Methodology

The numerical M-K model built in this chapter is used to predict the different FLCs (Figure 3.2). The simplified naming Ti21S L and Ti21S T are used for the fitting curve from the uniaxial tensile specimen Ti21S L,0, with anisotropy parameters adapted to investigate the effect of anisotropy. Ti21S+ and Ti5553 are based on the uniaxial tensile specimen Ti21S+ L,0 and Ti5553 L,0 with isotropic mechanical properties respectively. Ti21S L,0, Ti21S L,50 and Ti21S L,75 are obtained by assuming isotropic hardening.

According to the experimental forming limit point from the uniaxial tensile test, the ratio of the strain components can be obtained and then S value for the uniaxial tensile path can be applied in the FE M-K model. The imperfection value f_0 in the M-K model is adjusted in order to obtain good correlation between the experimental and the predicted forming limit point from uniaxial tension test. Then the whole predicted FLC can be plotted by changing the S value. Figure 3.14 shows this predicting procedure.

3.4.2 Predicted FLCs of Ti21S L,0, Ti21S L, Ti21S T, Ti21S+ and Ti5553

The properties of the materials used in the simulation are shown in Table 3.4. The comparison of experimental point and predicted forming limit curve of Ti21S L,0, Ti21S L, Ti21S T, Ti21S+ and Ti5553 are shown in Figure 3.15 and Figure 3.16. The S value and imperfection f_0 used in predicted FLC are listed in the Table 3.5.

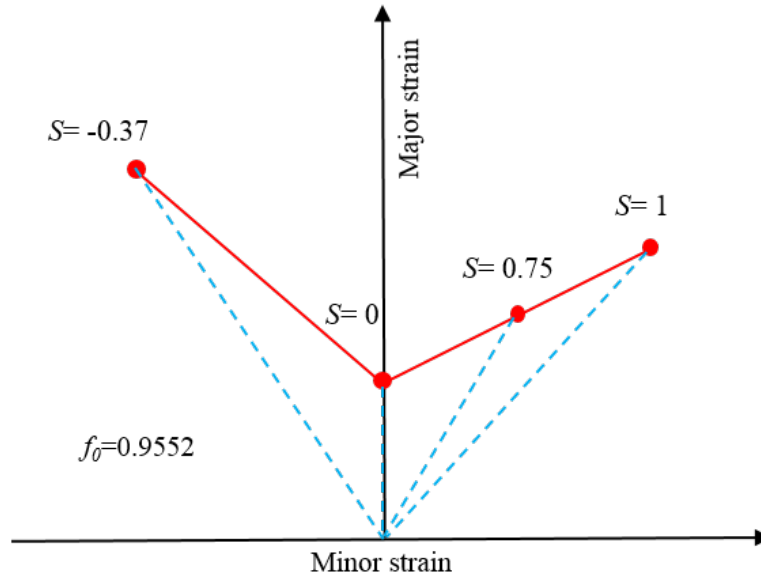
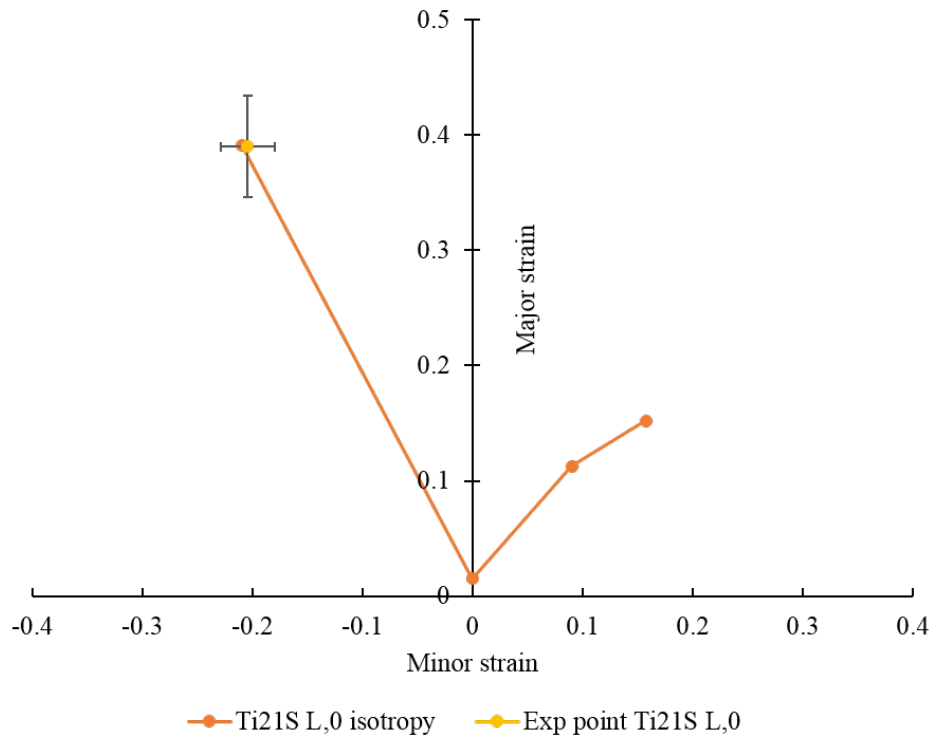


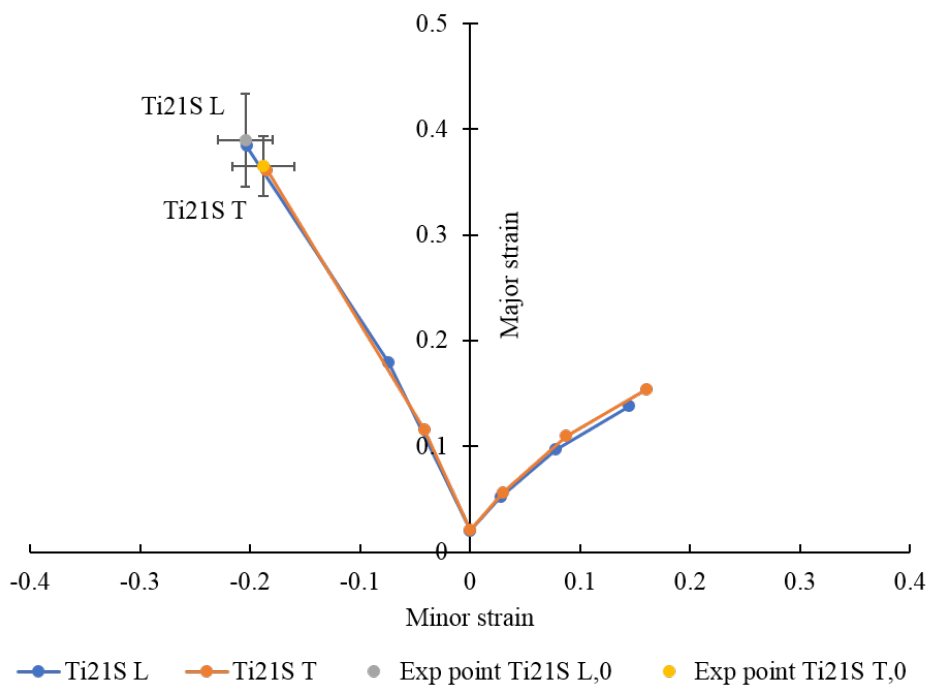
Figure 3.14: Schematic of plotting the whole FLC by using different S values

Table 3.4: Properties of the materials used in simulation of isotropic Ti21S L,0, anisotropic Ti21S L, anisotropic Ti21S T, Ti21S+ and Ti5553

Material	E (MPa)	ν	Hardening laws	Isotropic/Anisotropic
Ti21S L.0	77137	0.36	$\bar{\sigma} = 750 + 481\bar{\epsilon}_p^{0.4}$	Isotropic
Ti21S L	77137	0.36	$\bar{\sigma} = 750 + 481\bar{\epsilon}_p^{0.4}$	Anisotropic
Ti21S T	77137	0.36	$\bar{\sigma} = 750 + 481\bar{\epsilon}_p^{0.4}$	Anisotropic
Ti21S+	118366	0.36	$\bar{\sigma} = 1150 + 628\bar{\epsilon}_p^{0.46}$	Isotropic
Ti5553	68245	0.28	$\bar{\sigma} = 700 + 278\bar{\epsilon}_p^{0.36}$	Isotropic



(a) Isotropic Ti21S



(b) Anisotropic Ti21S L and Ti21S T

Figure 3.15: Comparison of experimental point and predicted FLC assuming (a) isotropic Ti21S, (b) anisotropic Ti21S L and Ti21S T

From the predicted FLC of Ti21S L and Ti21S T (Figure 3.15(b)), it can be seen that the predicted curve of Ti21S L and Ti21S T are almost the same. The imperfection value f_0 are close. It can be concluded that the anisotropy doesn't have obvious effect on the predicted FLCs.

Table 3.5: Minimum S value and imperfection f_0 used in predicted FLC of isotropic Ti21S L, anisotropic Ti21S L, anisotropic Ti21S T, Ti21S+ and Ti5553

Material	S minimum	f_0
Isotropic Ti21S L,0	-0.37	0.9525
Anisotropic Ti21S L	-0.37	0.9460
Anisotropic Ti21S T	-0.37	0.9552
Ti21S+	-0.43	0.9050
Ti5553	-0.39	0.9485

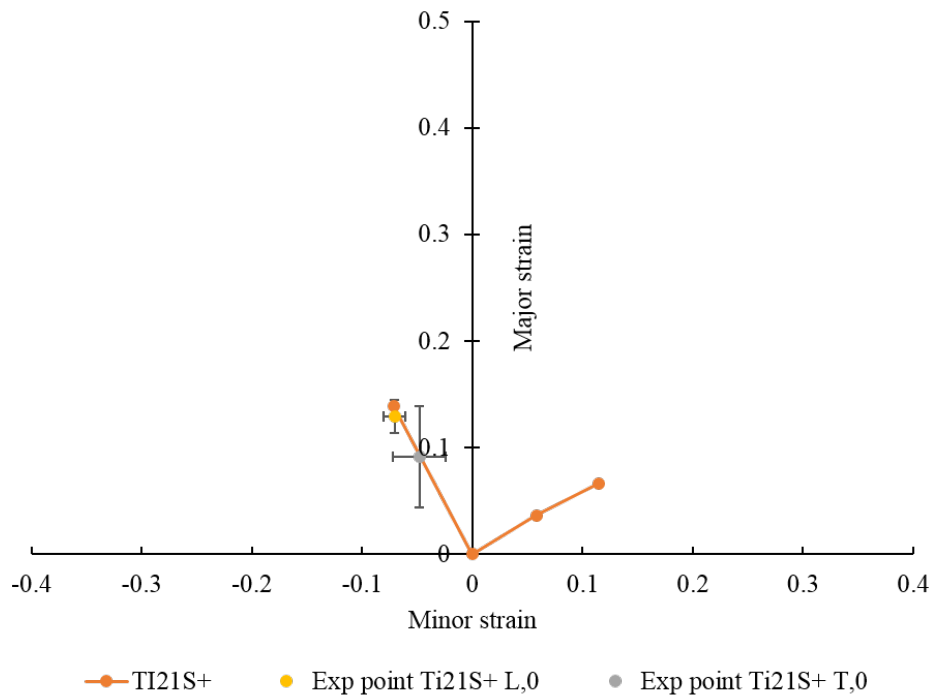
From the predicted FLC of Ti21S+ (Figure 3.16(a)), it has lower formability than Ti21S L,0 for each strain path. The lowest experimental point from the tensile test leads to the smallest value of imperfection factor f_0 . The predicted FLC at the plane strain of Ti21S+ is very close to 0. This phenomenon is due to the low strain volume of the uniaxial tensile test. From the predicted FLC of Ti5553 (Figure 3.16(b)), it can be seen that the formability of Ti5553 is between Ti21S L,0 and Ti21S+. These three materials all indicated low formability in the plane strain condition (minor strain=0).

3.4.3 Predicted FLCs of Ti21S L,0, Ti21S L,50 and Ti21S L,75

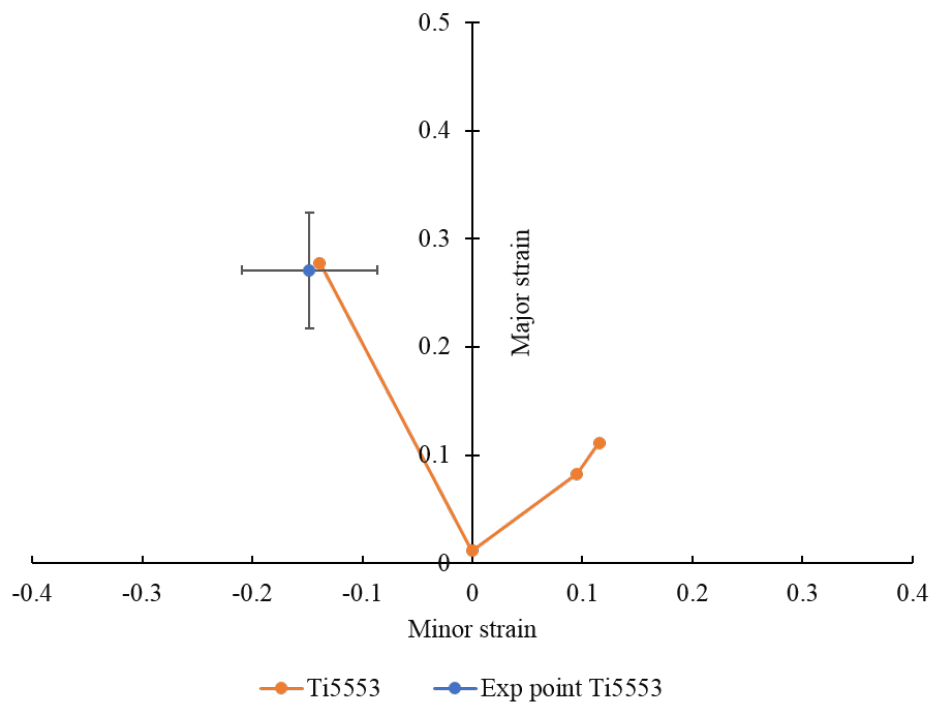
The predicted FLCs of Ti21S alloys with different rolling reduction rates are plotted with the same method. The properties of the materials used in the simulation are shown in Table 3.6.

Table 3.6: Properties of the materials used in simulation of Ti21S L,0, Ti21S L,50 and Ti21S L,75

Material	E (MPa)	ν	Hardening laws	Isotropic/Anisotropic
Ti21S L,0	77137	0.36	$\bar{\sigma} = 750 + 481\bar{\epsilon}_p^{0.4}$	Isotropic
Ti21S L,50	66600	0.36	$\bar{\sigma} = 750 + 428\bar{\epsilon}_p^{0.44}$	Isotropic
Ti21S L,75	66381	0.36	$\bar{\sigma} = 750 + 228\bar{\epsilon}_p^{0.2}$	Isotropic



(a) Ti21S+



(b) Ti5553

Figure 3.16: Comparison of experimental point and predicted FLC of (a) Ti21S+, (b) Ti5553

The comparison of experimental points and predicted forming limit curves of Ti21S L with 0%, 50% and 75% are shown in Figure 3.17. The S value and imperfection f_0 used in predicted FLC are listed in the Table 3.7.

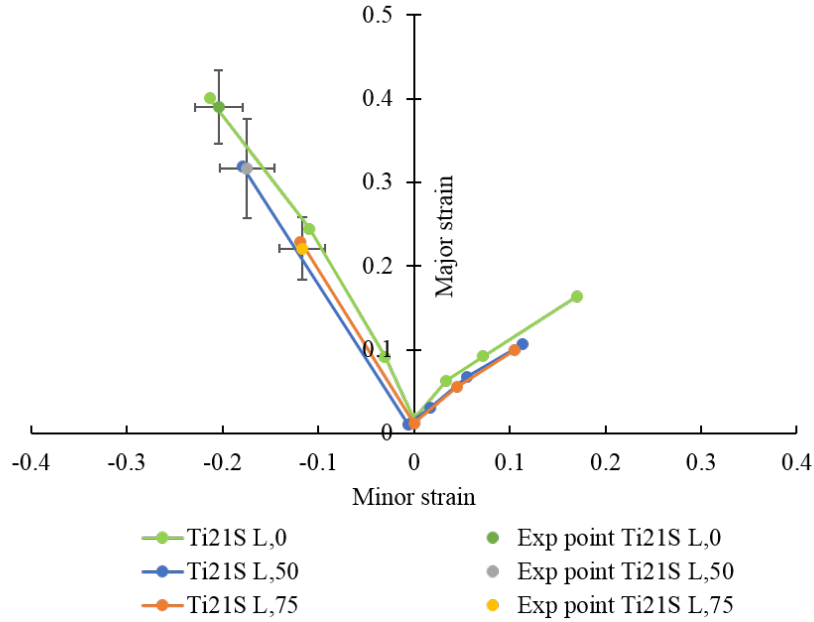


Figure 3.17: Comparison of experimental point and predicted FLC of Ti21S L,0, Ti21S L,50 and Ti21S L,75

Table 3.7: Minimum S value and imperfection value f_0 used in predicted FLC of Ti21S alloys with different reduction rate

Material	S minimum	f_0
Ti21S L,0	-0.370	0.9525
Ti21S L,50	-0.417	0.9258
Ti21S L,75	-0.417	0.9425

From these results, the difference in the shape between these three conditions is not evident. The imperfection value f_0 of Ti21S L,0 is the highest, corresponding to the best formability on the uniaxial stretching path. It leads to the best formability under equibiaxial tension. With very different values of f_0 , the forming limits under the equibiaxial strain path of Ti21S L,50 and Ti21S L,75 are almost the same. The predicted forming limit on plane strain is very low.

3.4.4 Conclusions

The whole FLC can be plotted through calibrating forming limit point from the tensile test with different parameters S and f_0 value. Some conclusions can be

made.

Anisotropy parameters of Ti21S alloys are calculated and applied in the predictive model. The results show that anisotropy has no significant influence on the formability.

The formability of Ti21S alloys between solution treated condition and solution treated and aging condition has great difference. The low formability of Ti21S+ can be attributed to the effect of α precipitates after aging. These precipitates increased the tensile strength but reduced the ductility. In the scale of microstructure, it increased the potential defects. This phenomenon is observed and explained in the fractograph part of Chapter 2. On the numerical simulation, it acted as a smaller imperfection value f_0 for this condition. Then it affects the whole predicted FLC.

The different mechanical behavior of Ti5553 from Ti21S affects their formability. The different chemical composition leads to different solution states, larger grain size and higher texture intensity. All of these can be factors that reduced formability.

The rolling reduction rate can have an evident effect on the uniaxial stretching condition of Ti21S alloys but a less evident effect on other strain paths. The Ti21S L,0 has the highest imperfection value f_0 but Ti21S 50 has the lowest. The value f_0 is not only dependent on the forming limit points from the tensile test but is also sensitive to the mechanical behavior of the materials. From the general comparison between the strain hardening rate n and the imperfection value f_0 , it also can be concluded that the effect of n on the imperfection value f_0 is not evident. The reason for this phenomenon is probably because the simulation neglected the different ultimate strain of materials.

All the predicted FLCs have a similar shape, the difference is only at the uniaxial stretching and biaxial. In the plane strain condition, the predicting results are quite similar. They all have very low formability for this strain path.

3.5 Conclusions

A numerical M-K model has been built to predict the whole forming limit curve of different titanium alloys. This model is based on the M-K theory and has been validated by comparison with the analytical M-K model. Ludwik's hardening law has been chosen here and has been calibrated for the different titanium alloys (Ti21S and Ti5553) studied.

The r -value of Ti21S alloys is calculated by tensile test in five directions. The r -value in 45° is lower than 0° and 90° . A numerical tensile test model with anisotropy is built and the $r_{22.5}$, $r_{67.5}$ values are validated by this numerical tensile

model.

The FLCs are predicted by numerical M-K model calibrated from the forming limit point of the uniaxial tension path. Predicted FLCs in different conditions are compared. The relationship between imperfection value f_0 and microstructure is found. The precipitate condition Ti21S+ has the lowest f_0 , which demonstrates that α precipitates in the β matrix is bad to the formability. The texture affects the r -value of Ti21S L and Ti21S T and consequently the formability. High r -value corresponds to high formability. All the predicted FLCs have low formability at plane strain conditions.

Chapter 4

Characterization of the formability of Ti21S titanium alloy by Marciniak test

4.1 Introduction

In this chapter, experiments with a conventional Marciniak setup will permit to establish experimental forming limit curves for Ti21S titanium alloys. These experimental curves can validate the predicted forming limit curve, which is plotted with the help of an experiment point from a tensile test through a numerical M-K model.

The predicted forming limit curves of Ti21S and Ti5553 alloys have been plotted in Chapter 3 through a numerical M-K model. Each curve is only using one experimental point from a uniaxial tensile test. This point provided an imperfection value f_0 to adapt the prediction on the other strain paths. The experimental method is crucial to validate this numerical M-K model and the predicted forming limit curves.

The Marciniak device available in our group is firstly designed for the determination of the forming limit curves at necking or rupture of aluminium alloys and steels. Preliminary tests performed on titanium alloys have shown a premature rupture of the blank in a non-planar area (curvature radius induced by the punch or the die), an area outside of the one filmed during the test. A determination of the formability limits is impossible in this case.

Marciniak test device and dimensions of the specimen are first optimized through finite element simulation in order to obtain necking in the central zone of the specimen. The parameters of fillet radius of punch, fillet radius of blank holder, shape of specimen and thickness of intermediate part of the specimen are investigated. The Marciniak test device and the specimen are thus modified as the parameters optimized in simulation.

Tests on titanium alloy Ti21S are then conducted on the modified Marciniak test device with success. A modified method to detect forming limit points is proposed and the experimental forming limit curve at necking is plotted. The comparison between the predicted FLC and the experimental one is discussed.

4.2 Presentation of Marciniak test

4.2.1 Marciniak test device

The existing Marciniak device is modified from the device in standard ISO 12004-2 [119]. It has smaller dimensions by proportionality. This device has a smaller specimen size than that in standard ISO 12004-2, so that the tests can be conducted on a device with lower capacity.

Figure 4.1 shows the setup of the Marciniak test device. The blank holder clamps the specimen, and holds it from slipping. On the other side of the specimen

is the punch. Good lubrication is required between the punch and the specimen. The bottom surface with a speckle pattern is facing a 45° mirror under the specimen which allows the image to reflect into a camera recording 50 images/s with the resolution of 512×416 . In order to keep a steady focusing distance to the specimen during the test, the punch is fixed and the blank holder rises together with the specimen at a speed of 1 mm/s. The sheet is deformed until fracture. The strain of the deformed specimen is measured with three parallel sections by DIC method and the forming limit points can be plotted.

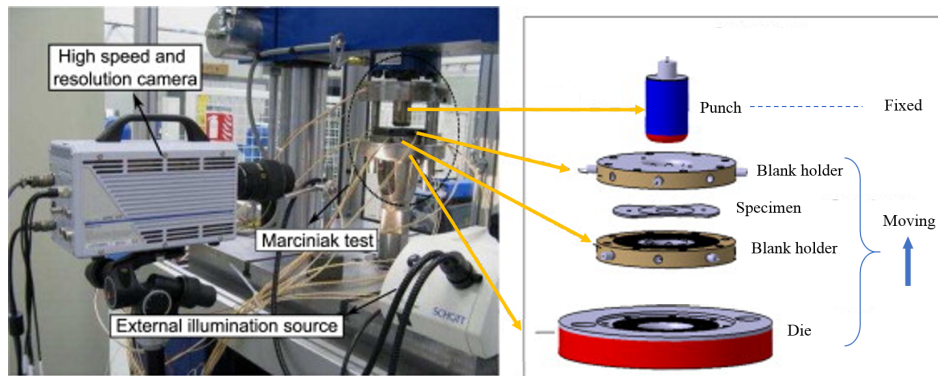


Figure 4.1: Marciniak test device

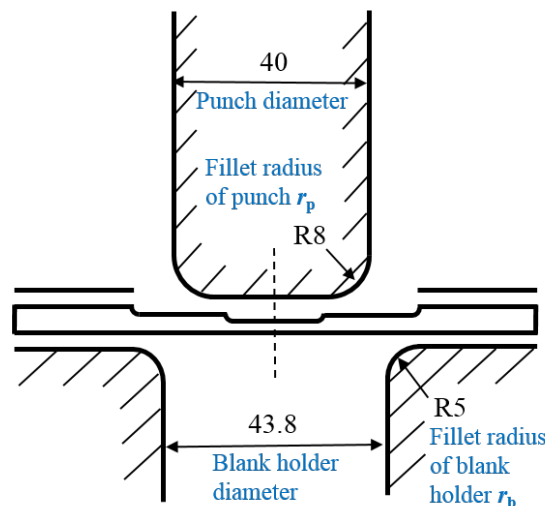


Figure 4.2: Dimensions (in mm) of Marciniak device

4.2.2 Marciniak test specimen

Different from the uniform thickness adapted in the standard, the modified Marciniak specimens contains three parts with different thicknesses. Dimensions of the specimen is shown in Figure 4.3. These modifications are for the Marciniak test on

aluminium by some previous researchers [163][164][165]. The thickness of the specimen is increasing from the center area to the surroundings. These three parts with different thicknesses are called center, intermediate and clamping. This design can reduce the number of the components for Marciniak test compared to standard ISO 12004-2 and further reduce the required force during the test.

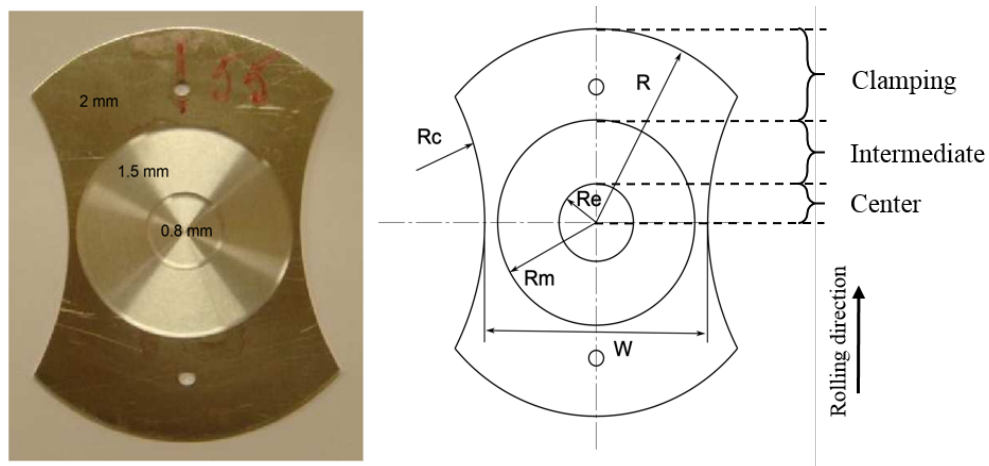


Figure 4.3: Dimensions of Marciniak test specimen with three thicknesses (0.8mm, 1.5mm and 2mm)

The values of R , R_m , R_e and R_c are fixed for each specimen, W is measured perpendicular to the rolling direction and can vary in order to realize different strain paths. The dimensions of these parameters of Marciniak specimens are listed in Table 4.1.

Table 4.1: Dimensions of Marciniak specimens

Parameters	R	R_m	R_e	R_c	W
Dimensions (mm)	50	26.5	10	70	10-100

The specimens are painted at the flat side with a speckle pattern (Figure 4.4) in order to analyze the strains. The different strain paths and the corresponding specimens with different W are shown in Figure 4.5. The experimental forming limit curve can be plotted from such a group of specimens.

4.2.3 Experimental validation of the Marciniak test dimensions for titanium alloys

Marciniak tests on titanium alloy TA6V are firstly conducted on the existing device in order to check that necking appears in the central zone of the specimen.

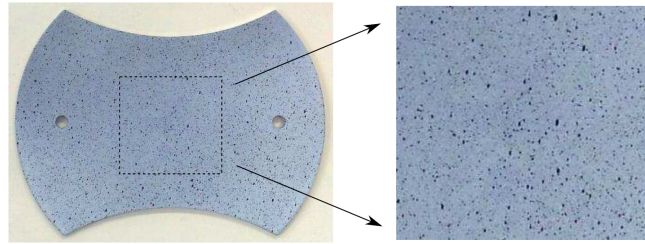


Figure 4.4: Specimen painted with a speckle pattern

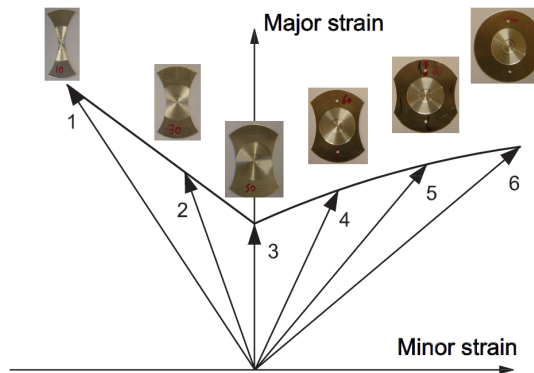


Figure 4.5: Forming limit curve and the corresponding specimen of Marciniak test

Firstly, the specimens with the strain path of uniaxial tension ($W=10$ mm) and plane strain ($W=52$ mm) of TA6V are tested. Results show that the strain localizes near the radius of the clamping part on both TA6V specimens (Figure 4.6) and not in the desired center zone of the specimen. A very small punch displacement was observed which indicates a low deformation before the fracture. This connecting area induces stress concentration due to its geometry, especially if there are some defects from processing, making the fillet on the specimen vulnerable.

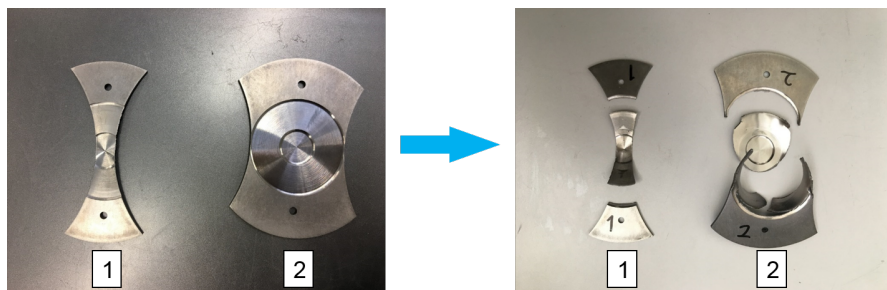


Figure 4.6: Uniaxial and plane strain TA6V specimens before and after Marciniak tests

The explanation of this phenomenon is the different mechanical behavior of titanium and aluminium alloys. Titanium alloy TA6V has high yield stress and low hardening rate (yield stress and ultimate tensile strength of TA6V are very

close) while aluminium alloys are on the contrary. In order to realize the Marciniak test on titanium alloys, the Marciniak device must be optimized.

4.3 Simulation and optimization of the Marciniak test

4.3.1 Finite element model of Marciniak test

Finite element simulations have been led to understand and try to prevent strain localization outside the center zone. Figure 4.7 shows the FEM model of the Marciniak test.

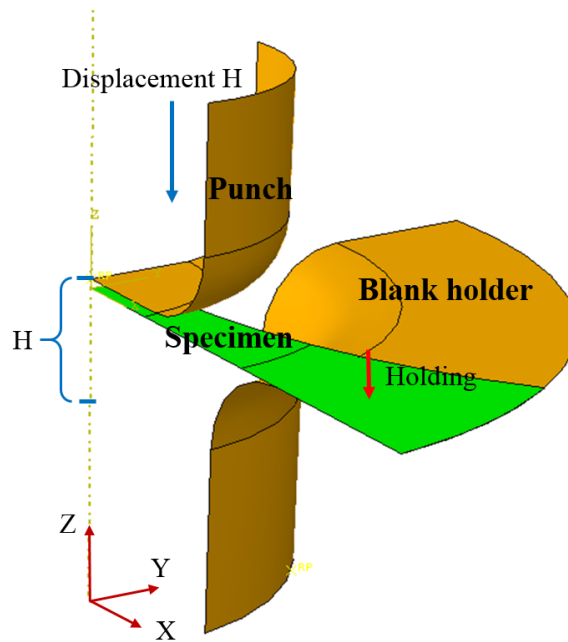


Figure 4.7: Marciniak test parts of the model

One-fourth of the total device is considered because of the two symmetry planes (XZ and YZ) of the device. The punch and the blank holder are considered rigid solids so they are constructed with shell elements. It can reduce the total number of elements calculated. A displacement of a value H is set to simulate the motion of the punch. The specimen is also meshed by shell element with three layers. The result of the center layer is used for analysis. Three parts are divided in order to distinguish the different areas of the uniaxial specimen of Marciniak test (Figure 4.8). E_c , E_i and E_m correspond to the thickness in the center, intermediate and clamping parts. 0.8 mm, 1.5 mm and 2 mm are set as corresponding original thicknesses. The contact zone between the specimen and the punch has no friction.

The zone between the specimen and blank-holder has a friction coefficient of 0.1. Loads of 51.8 MPa are applied on the clamping part of the specimen.

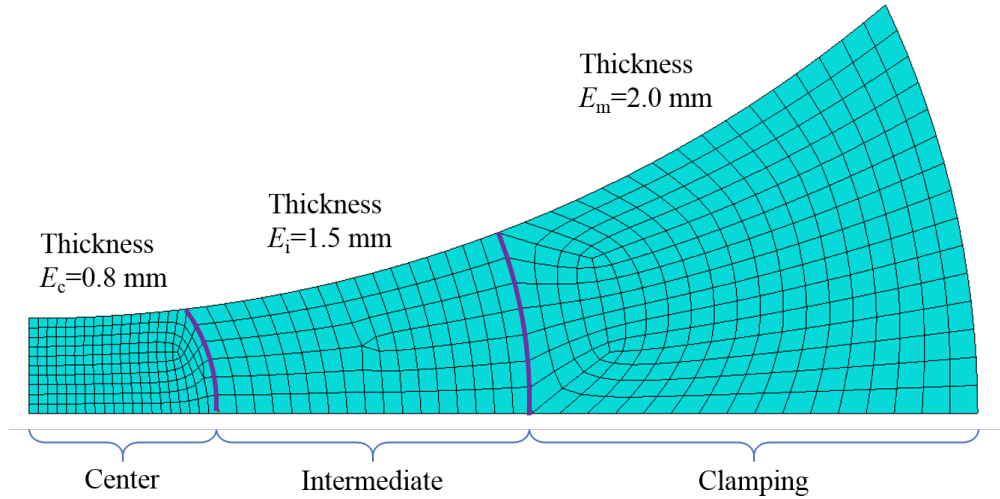


Figure 4.8: Three thickness zones and mesh of Marciniak specimen

The materials of TA6V but also Ti40 commercially pure titanium are used for comparison. Tensile test results are used for these two materials. The yield stress of TA6V is higher than Ti40 and the hardening rate of TA6V is lower. Figure 4.9 shows the plastic properties of these two materials used in the simulation. The ultimate tensile strength (*UTS*), Young’s modulus (*E*) and Poisson ratio (*v*) used in the simulation of TA6V and Ti40 are listed in Table 4.2.

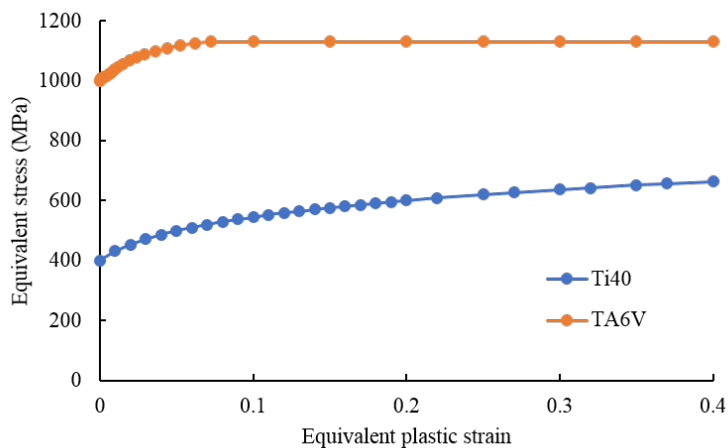


Figure 4.9: Plastic strain - stress curves of TA6V and Ti40

In order to simply simulate the procedure of Marciniak test, the blank holder is fixed. The punch has a displacement of 20 mm to the direction of the specimen.

Figure 4.10 shows simulation results for TA6V when the maximum Mises stress of some part of the specimen has reached *UTS* of 1131 MPa. This does not mean

Table 4.2: Ultimate tensile strength (UTS), Young's modulus (E) and Poisson ratio (ν)

Material	UTS (MPa)	E (GPa)	ν
TA6V	1131	101	0.34
Ti40	627	110	0.30

that the fracture happens because the local stress when fractured is more than this value. But 1131 MPa used here is to set a criterion of the time just before failure. The distribution of Mises stress can be used to identify the area where localization is most likely to happen. The same criterion is also used in the following parts.

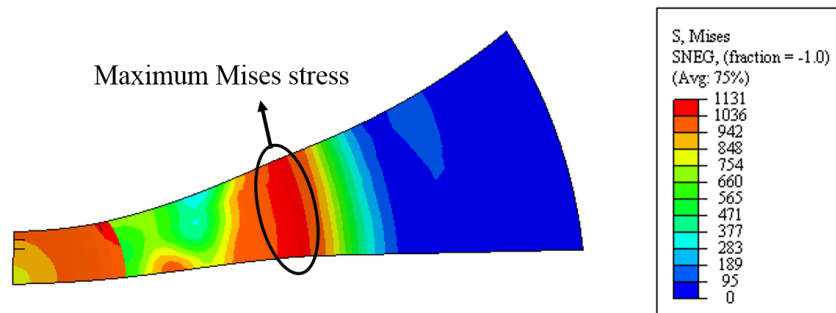


Figure 4.10: Mises stress distribution on the TA6V specimen when the maximum reaches 1131 MPa

From the distribution of Mises stress in TA6V, the area where the stress reached 1131 MPa is not in the center. It is located in the first peripheral, the contacted area with the punch and the second peripheral. This means the first rupture very likely happens in these areas instead of the center.

The displacement of the punch (H) until fracture in the simulation of TA6V is 4.2 mm, while the measured displacement in the experimental Marciniak test of TA6V is 5.8 mm. Considering the offset of the punch and specimen in the experiment, the displacement from simulation and experiment is quite close, which can be a good factor to measure the extent of the deformation. This displacement at fracture can evaluate the forming behaviors. A material that has a large displacement of punch in simulation is more likely to have the maximum stress in the center, which has more possibilities to complete the Marciniak test successfully in the experiment.

Figure 4.11 shows the simulation result of Ti40 when the Mises stress of some part of the specimen has reached 627 MPa. From the distribution of stress of the Ti40 in the figure, the area where the stress reached 627 MPa is just located in the center. This means the rupture of Ti40, in this case, is very likely to happen

in the center.

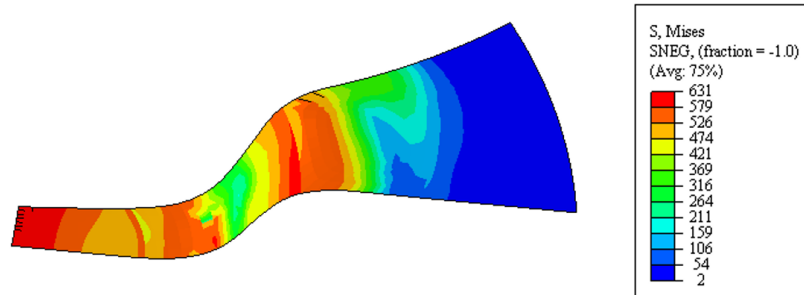


Figure 4.11: Mises stress distribution on the specimen Ti40 when the maximum reaches 627 MPa

The difference in properties between these two materials is the main cause of different simulation results. The TA6V has very high yield stress and little strain hardening. It demonstrates that the Marciniak test is not suitable for TA6V in our condition, while Ti40 has lower yield stress and some strain hardening, which makes it successful in Marciniak test. Whatever, optimizing the test parameters can at least reduce the risk, especially for materials with low hardening.

4.3.2 Parametric study

In order to avoid the strain localization near the radius of the clamping part, the Marciniak device has to be optimized. All the parameters that may affect the distribution of the stress are critical to have localization in the center. Therefore, the fillet radius of blank holder r_b , the effect of the fillet radius of punch r_p , the different surface shape and the thickness of intermediate part E_i of the specimens will be investigated in this section.

During the deformation, there are three points on the specimen that have a high possibility of fracture in simulation. We are focusing on these points which are named center (C), bending center (B,c) and bending edge (B,e). They present stress concentration due to geometry. Figure 4.12 shows the definition of the center (C), bending center (B,c) and bending edge (B,e).

In order to have a quantitative analysis of a test, a G value is proposed:

$$G = Max\left\{\frac{\bar{\varepsilon}_c}{\bar{\varepsilon}_{B,c}}, \frac{\bar{\varepsilon}_c}{\bar{\varepsilon}_{B,e}}\right\} \quad (4.1)$$

Where $\bar{\varepsilon}_c$ is the equivalent plastic strain in the center (C), $\bar{\varepsilon}_{B,c}$ is the equivalent plastic strain in the bending center (B,c), $\bar{\varepsilon}_{B,e}$ is the equivalent plastic strain in the bending edge (B,e). All these values are obtained at the moment when the Mises stress reaches the ultimate tensile strength of the material in any area. The

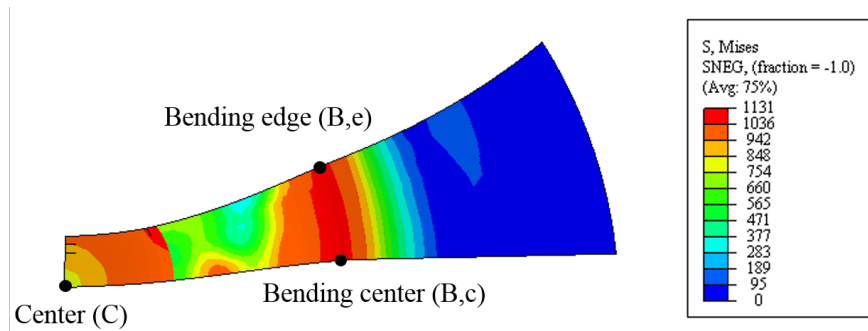


Figure 4.12: Definition of center (C), bending center (B,c) and bending edge (B,e)

larger the G value, the more suitable the test. The material of Ti40 is used in the following investigations just for a convenient comparison between the simulation results from different parameters.

4.3.3 Effect of fillet radius of blank holder r_b

The original dimension of the fillet radius of blank holder is $r_b=5$ mm. Increasing that radius will reduce the bending angle during the test. This may reduce the stress concentration in the bending area. Considering the fracture location of Marciniak test of TA6V is exactly on the bending area, the investigation of this parameter is very important. Enlarging the radius of blank holder r_b to 7.5 mm, 10 mm and 12.5 mm is proposed. The result of the distribution of Mises stress at rupture moment is plotted to find out its evolution and the best parameters. The evolution of equivalent plastic strain is plotted and the displacements of the punch (H) when fracture happens are listed for comparison.

Figure 4.13 shows the result of the simulation of different fillet radius of blank holder r_b . The simulation result with the fillet radius of blank holder r_b of 5 mm shows that both the center and bending area have high stress. The distribution of stress and strain provides the possibility of fracture in both areas. That demonstrates the stress in these two areas is very similar. This specimen has a high risk of fracture in the bending area. With increasing fillet radius of blank holder r_b , the stress concentration on the bending area is less significant. Enlarging the fillet radius of blank holder r_b is a good way to increase the possibility of success of Marciniak test on titanium alloys.

Figure 4.14 shows the evolution of equivalent plastic strain with different fillet radius of blank holder r_b . The evolution of the ratio of the equivalent plastic strain shows that the deformation in the bending area occurs first. When the specimen is bent, the Mises stress on the center increases. It leads to a sudden increase in the equivalent plastic strain. The competition between equivalent plastic strain and stress in these two areas contributes to the location of the fracture.

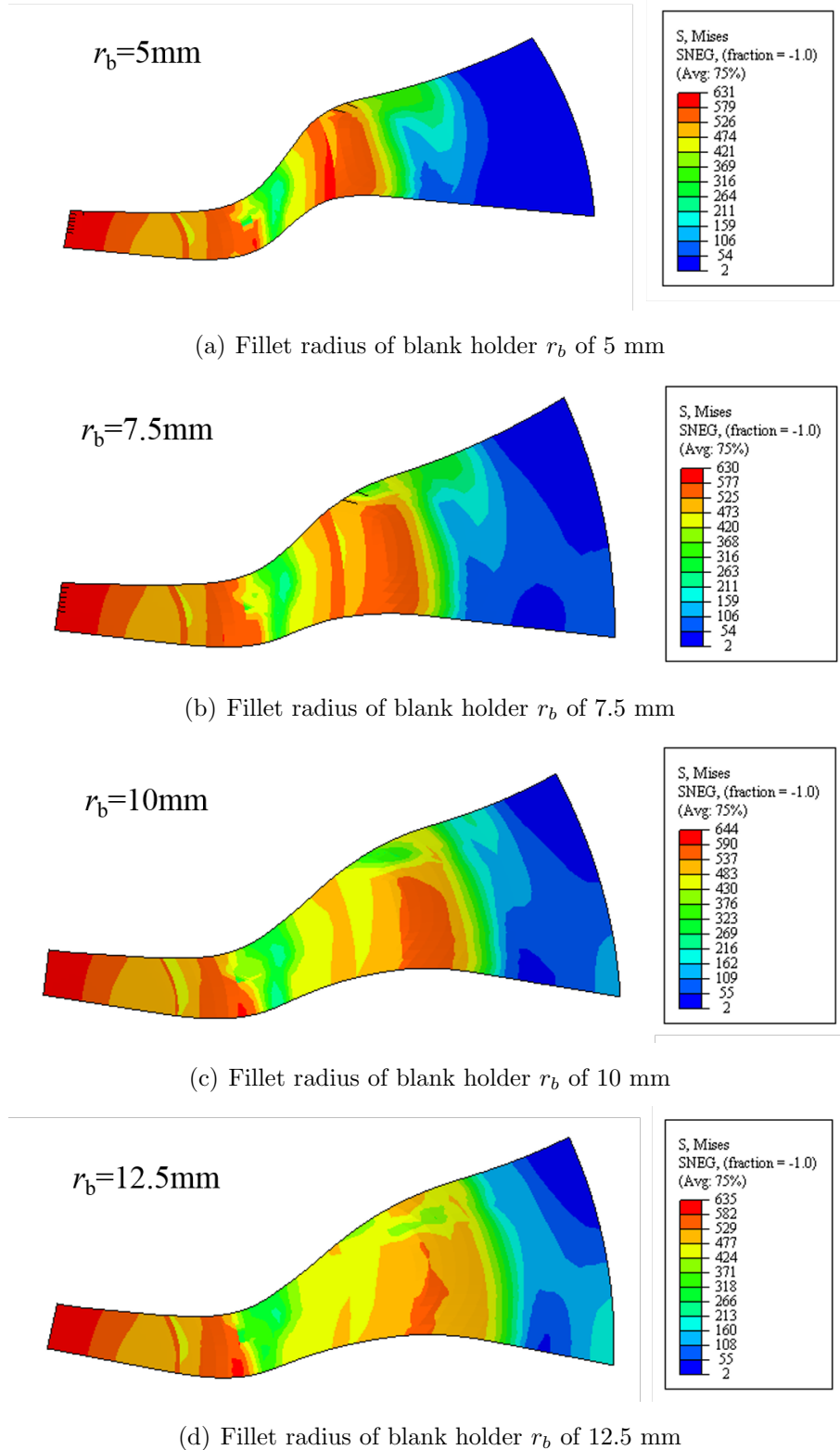


Figure 4.13: Distribution of Mises stress for Ti40 uniaxial specimens with different fillet radius of blank holder r_b

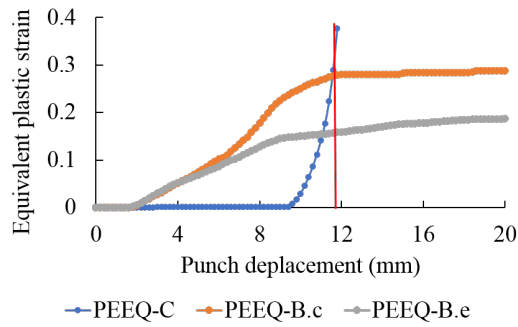
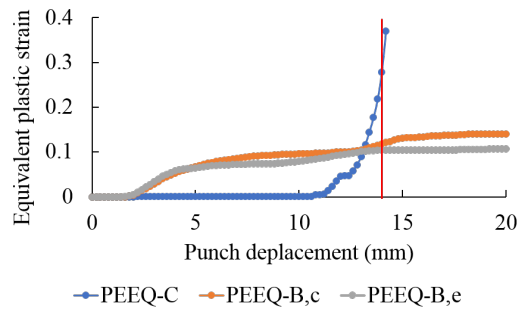
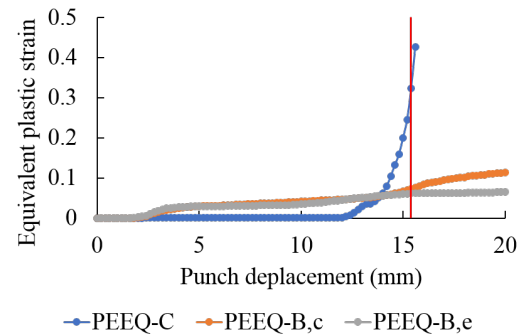
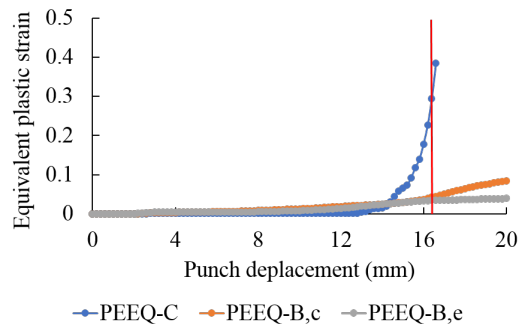
(a) Fillet radius of blank holder r_b of 5 mm(b) Fillet radius of blank holder r_b of 7.5 mm(c) Fillet radius of blank holder r_b of 10 mm(d) Fillet radius of blank holder r_b of 12.5 mm

Figure 4.14: Evolution of the equivalent plastic strain (PEEQ) with different fillet radius of blank holder r_b . Red vertical line indicates the punch displacement when the maximum Mises stress is reached

Increasing the fillet radius of blank holder r_b does not affect the evolution of equivalent plastic strain in the center. However, the punch displacement before reaching the maximum Mises stress is increased. The strain level in the connecting radius zone (B,c; B,e) decreases compared to the one at the central point of the specimen. Large r_b makes the center have the largest equivalent plastic strain when fracture happens.

The effect of the fillet radius of blank holder on the G value is plotted in Figure 4.15, and G value and displacement of the punch are reported in Table 4.3. The larger the fillet radius of blank holder, the larger the G value. From the Table 4.3, an evident increase of displacement of the punch is demonstrated. But in reality, the fillet radius of blank holder can not be too large. Otherwise, the blank holder will lose the area for holding the specimen. Slipping of the specimen will happen because of inadequate friction provided by the blank holder. Therefore, the enlargement of the fillet radius of blank holder from 5 mm to 10 mm can be conducted.

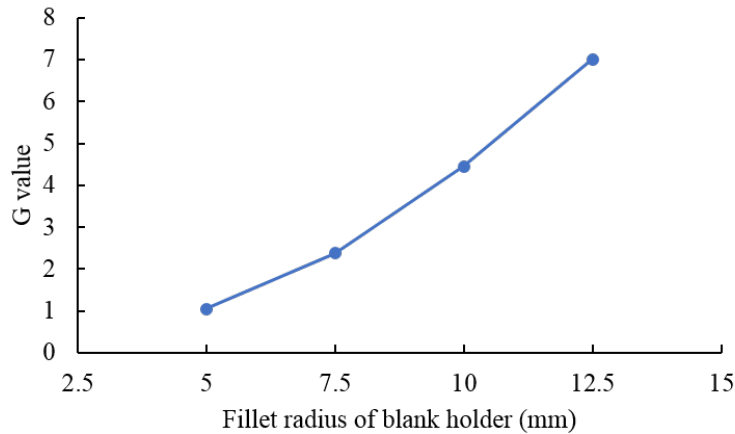


Figure 4.15: Effect of the fillet radius of blank holder on the G value

Table 4.3: G value and displacement of the punch (H) when ultimate tensile strength is reached with different fillet radius of blank holder r_b

r_b (mm)	G value	H (mm)
5	1.04	12.2
7.5	2.37	14.0
10	4.44	15.4
12.5	7.00	16.4

4.3.4 Effect of different fillet radius of punch r_p

The original dimension of the fillet radius of punch is $r_p=8$ mm. The parameter r_p can affect the contact position of the specimen and the punch, and then affect the deformation of the specimen. According to the radius of the punch (20 mm) and the geometry of the specimen, the fillet radius of punch r_p is modified as 6.5 mm or 9.5 mm. These parameters are simulated in Abaqus. The results of distribution of equivalent plastic strain at rupture moment, distribution of Mises stress at rupture moment, evolution of equivalent plastic strain are plotted for comparison. The displacements of the punch (H) when fracture happens are also listed. For all the simulations with different fillet radius of punch, the fillet radius of blank holder keeps an optimized value of 10 mm.

Figure 4.16 shows the results of the simulation of the different fillet radius of punch r_p . From the distribution of the stress in Figure 4.16, the rupture happens in the center. The distribution of the strain verifies that the center has the largest equivalent plastic strain. The increasing of the fillet radius of punch r_p reduces the Mises stress concentration in the contacting area of punch and specimen. The stress distribution in other areas has not much difference.

Figure 4.17 shows the evolution of equivalent plastic strain (PEEQ) with different fillet radius of punch r_p . The evolution of the equivalent plastic strain (Figure 4.17) shows no evident difference. The different fillet radius of punch r_p can affect the stress and strain on the contact zone but have a very limited effect on the center and bending zone.

In order to evaluate the risk of fracture, the G value of these conditions is plotted in Figure 4.18, and G value and the displacement of the punch are presented in Table 4.4. From Figure 4.18, increasing the fillet radius of punch indeed has an advantage on the rupture in the center. But this effect is not as significant as the fillet radius of blank holder. The displacement of the punch of these three conditions is very close and the value is large. Considering the risk and the workload of modifying this radius, the fillet radius of the punch is kept the same.

Table 4.4: G value and displacement of the punch (H) when ultimate tensile strength is reached with different fillet radius of punch r_p

r_p (mm)	G value	H (mm)
6.5	4.02	15.2
8	4.44	15.4
9.5	5.19	15.8

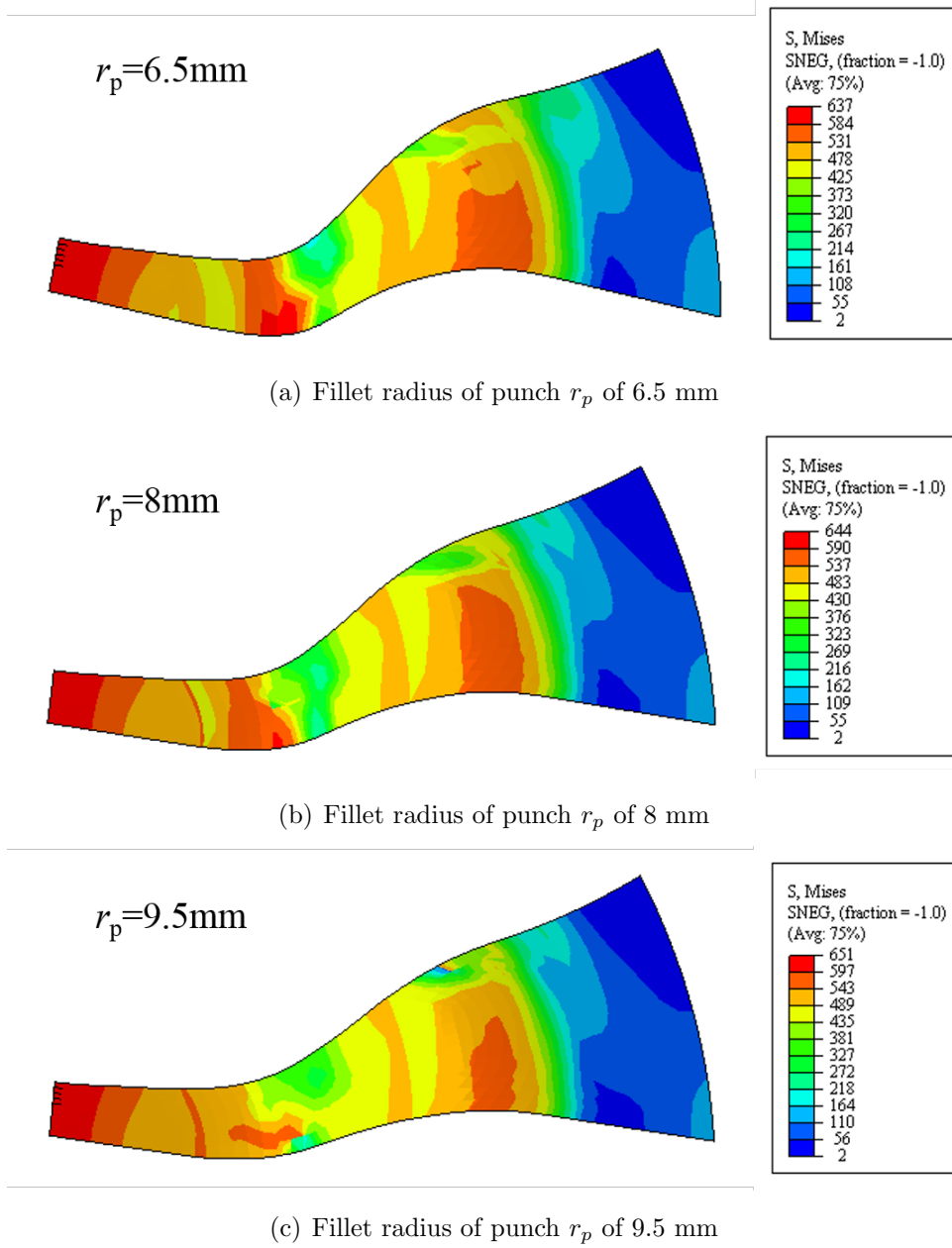


Figure 4.16: Distribution of Mises stress for Ti40 uniaxial specimens with different fillet radius of punch r_p

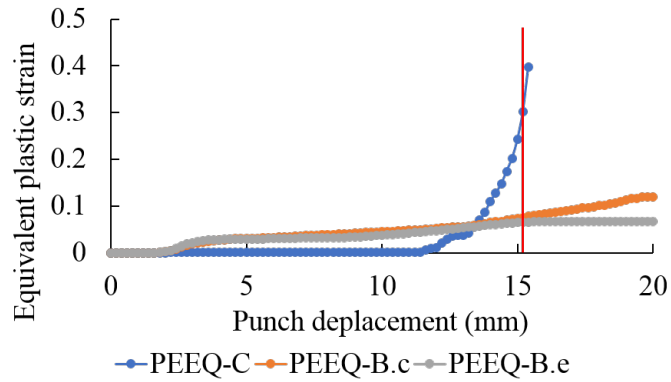
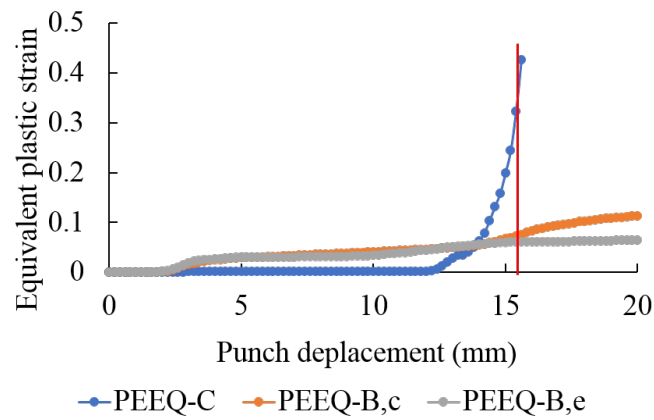
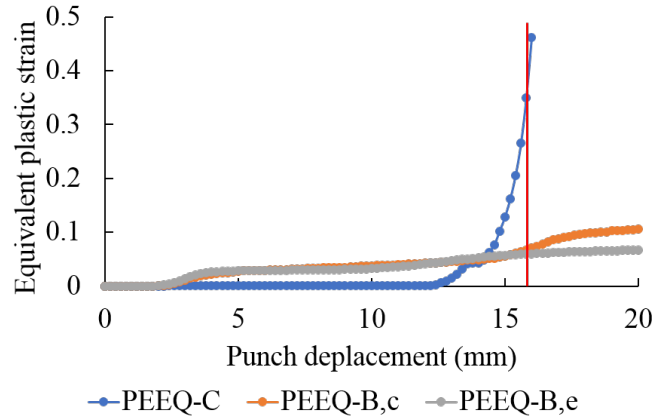
(a) Fillet radius of punch r_p of 6.5 mm(b) Fillet radius of punch r_p of 8 mm(c) Fillet radius of punch r_p of 9.5 mm

Figure 4.17: Evolution of equivalent plastic strain (PEEQ) with different fillet radius of punch r_p . Red vertical line indicates the punch displacement when the maximum Mises stress is reached

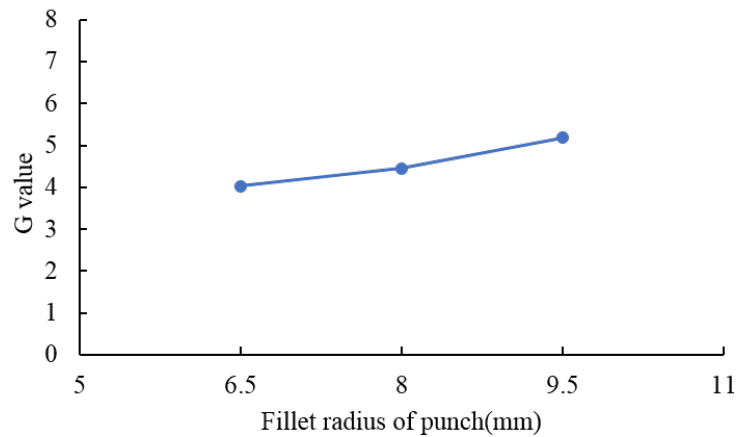


Figure 4.18: Effect of the fillet radius of punch on the G value

4.3.5 Effect of the shape of specimen

Traditional Marciniak test specimen has three parts with different thicknesses. The bending area is very close to the contact area of the intermediate and the clamping. To avoid stress concentration at defects on this contact area which underwent the machining or milling, a new specimen combining the intermediate and center parts in a curved surface is proposed (see the section in Figure 4.19). The thickness in the center point is 0.7 mm and there are no dimension defects for stress concentration. This model is built with 3D solid elements instead of shell elements due to its special shape. The result of the distribution of Mises stress at rupture moment is plotted (Figure 4.20). For this simulation, the fillet radius of blank holder is kept as 10 mm.

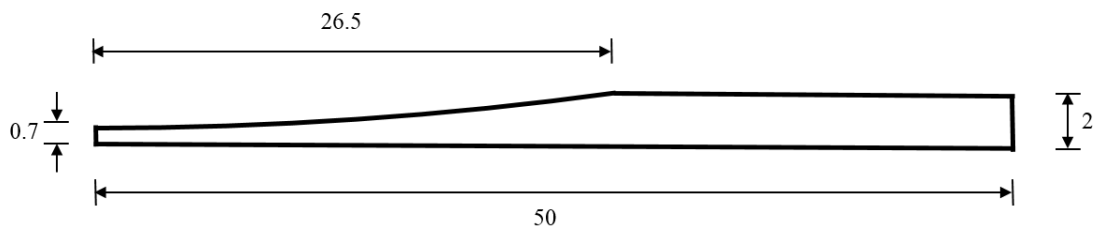


Figure 4.19: Section of the new specimen shape with curved surface

The result of the specimen with a curved surface does not have much improvement on the distribution of each part and the ratio of equivalent plastic strain. The machining of this new specimen still has some challenges, so this dimension is not applied in our future tests.

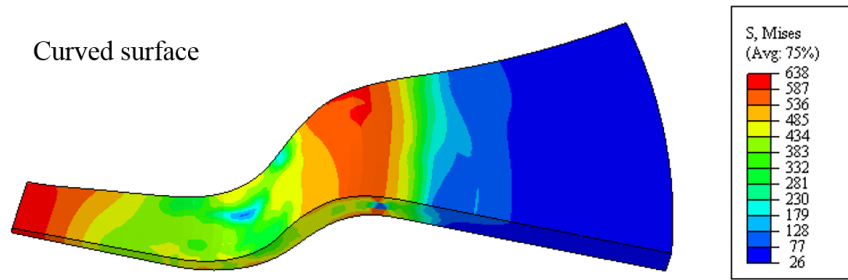


Figure 4.20: Distribution of Mises stress for Ti40 uniaxial specimens with curved surface

4.3.6 Effect of different thicknesses of intermediate part E_i

The intermediate part takes the stress concentration on the contact area and bending area, which makes it vulnerable in the test. The different thicknesses of the intermediate part E_i can change the stress and strain condition and may have different behavior. The original thickness of the intermediate part is 1.5 mm. The 1.2 mm, 1.8 mm and 2.0 mm are investigated and compared. Shell elements are used and distribution of Mises stress at rupture moment, evolution of equivalent plastic strain are plotted and the displacements of the punch (H) when fracture happens are listed for comparison. For all the simulations, the fillet radius of punch is kept as 8 mm and the fillet radius of blank holder is 10 mm.

Figure 4.21 shows the result of the simulation with different thicknesses of intermediate part E_i . The effect of the thickness of intermediate part on center and bending area is not evident. But it affects the contact area of the punch and specimen. With the increase of thickness, the stress concentration at the contact area is increased. This value in this area reaches the ultimate tensile strength of Ti40 when the intermediate thickness is 1.8 mm which is the same value as in the center. The thickness of 2.0 mm shows the extreme case of this change. The rupture happens neither in the center nor bending area, but only at the area where the punch is contacted. A thick intermediate part will reduce the flexibility of the specimen and makes it vulnerable to bending. Considering all these situations, the thickness of the intermediate part is kept the same as the original value.

Figure 4.22 shows the evolution of equivalent plastic strain with different thicknesses of intermediate part E_i . Even though the thicker intermediate part can reduce the evolution of the equivalent plastic strain at bending area, the fracture still can happen due to significant stress concentration.

The effect of the intermediate part on the G value is plotted in Figure 4.23, and G value and the displacement of the punch are presented in Table 4.5. The G value of the thickness of intermediate part E_i of 2.0 mm shows exactly the same conclusion than from stress. The displacement of the punch clearly shows the same

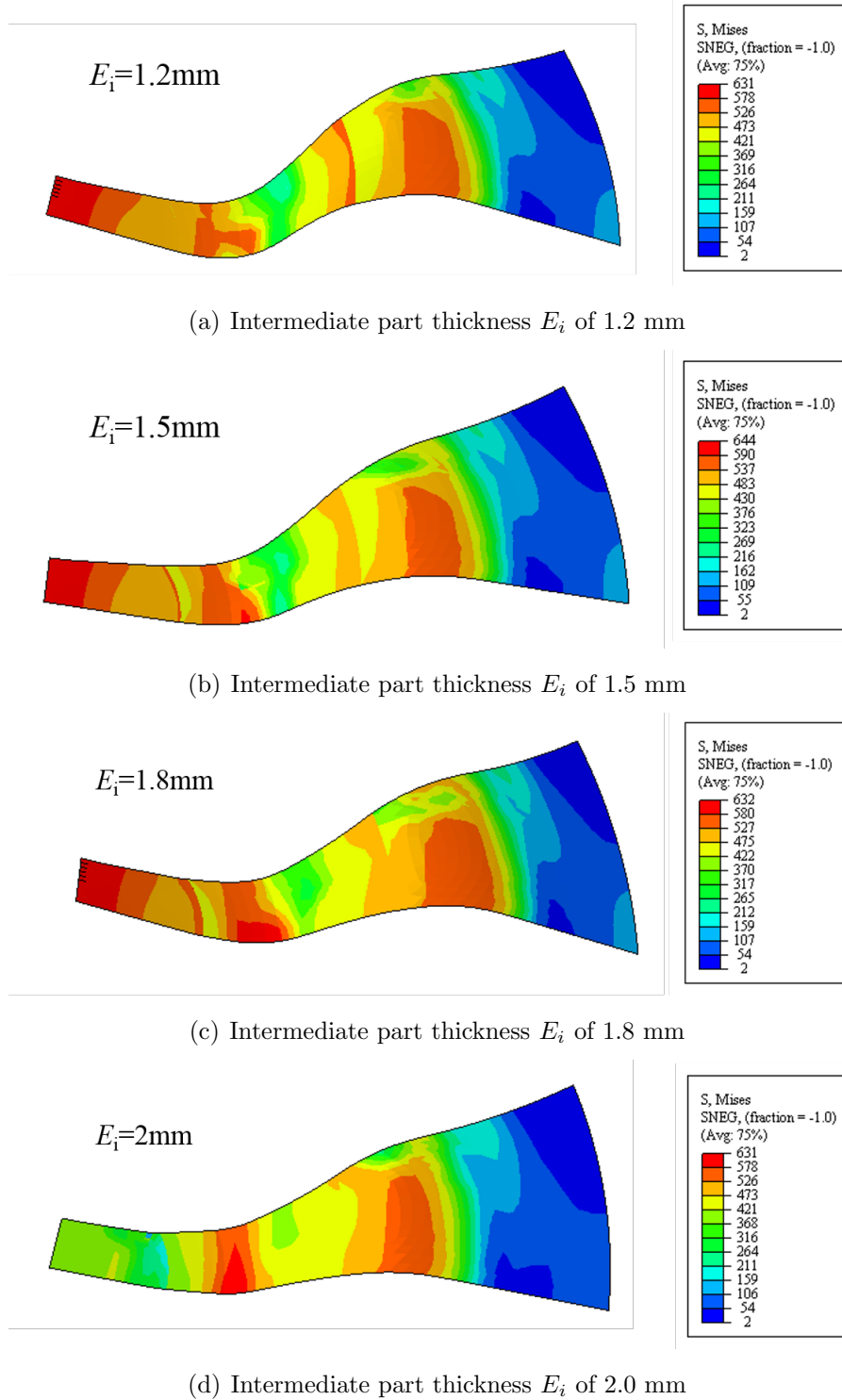


Figure 4.21: Distribution of Mises stress for Ti40 uniaxial specimens with different thicknesses of intermediate part E_i

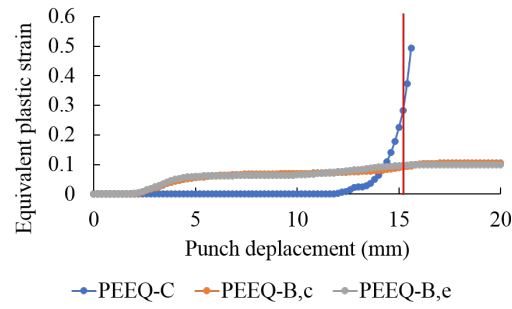
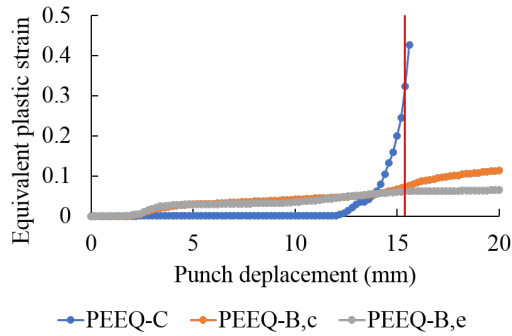
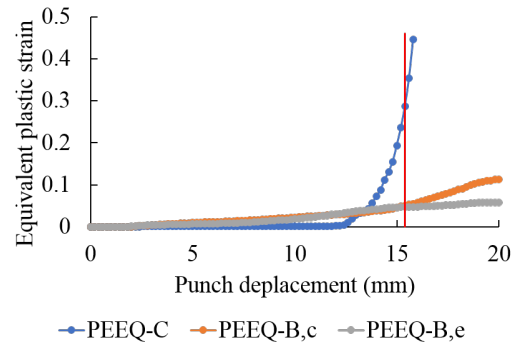
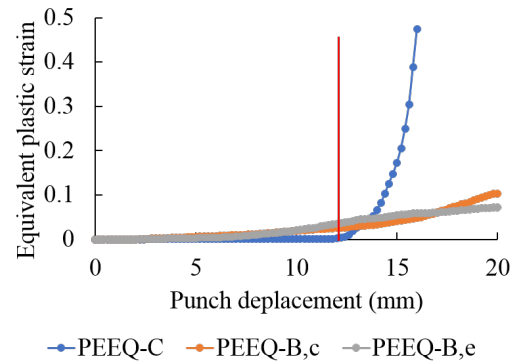
(a) Intermediate part thickness E_i of 1.2 mm(b) Intermediate part thickness E_i of 1.5 mm(c) Intermediate part thickness E_i of 1.8 mm(d) Intermediate part thickness E_i of 2.0 mm

Figure 4.22: Evolution of the equivalent plastic strain (PEEQ) with different thicknesses of intermediate part E_i . Red vertical line indicates the punch displacement when the maximum Mises stress is reached

tendency. When the Mises stress reaches the ultimate tensile strength, the rupture happens neither in the center nor bending area, but at the area where the punch contacted. The thick intermediate part will reduce the flexibility of the specimen and makes it vulnerable to bending. Considering all these situations, the thickness of the intermediate part E_i with a value intermediate to the center and clamping is suitable.

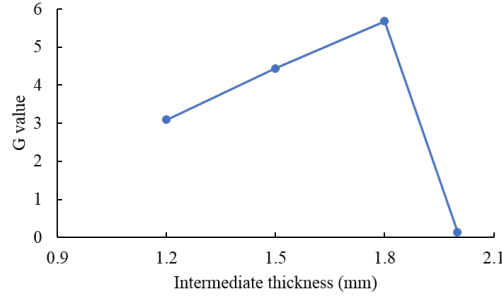


Figure 4.23: Effect of intermediate thickness on the G value

Table 4.5: G value and displacement of the punch (H) when ultimate tensile strength are reached with different thicknesses of intermediate part E_i

E_i (mm)	G value	H (mm)
1.2	3.09	15.2
1.5	4.44	15.4
1.8	5.68	15.4
2.0	0.14	12.2

4.3.7 Conclusions

In order to optimize the Marciniak test to achieve fracture in the center of specimens of titanium alloys, a finite element model of Marciniak test is built. The parametric study on the G value is applied to investigate the effects of fillet radius of blank holder r_b , fillet radius of punch r_p , curved specimen surface and thickness of intermediate part of the specimen E_i .

The results of simulations show that with increasing the fillet radius of blank holder r_b , there is more possibility to have a fracture in the center. The increase of the fillet radius of punch r_p , is beneficial to fracture in the center. But this effect is very limited. Compared to the Marciniak specimen with three steps, the specimen with a curved surface shows no advantage in Marciniak test. The increase of the thickness of intermediate part of the specimen E_i has the effect of first increasing

and then decreasing on G value. Considering all the simulation results and the risks, the modification on enlarging the fillet radius of blank holder r_b from 5 mm to 10 mm is conducted. The fillet radius of punch r_p is kept the same as 8 mm. The dimensions of specimens are kept with E_c , E_i and E_m corresponding to 0.8 mm, 1.5 mm and 2 mm.

4.4 Marciniak test

4.4.1 Experimental characterization of the formability on Ti21S alloy

The original thickness of Ti21S is 0.8 mm. The desired thickness is reduced by proportionality ($E_c=0.32$ mm, $E_i=0.6$ mm and $E_m=0.8$ mm). Because of the limitation of the thickness control on the machining machine with very thin sheets, the final measured thickness of Ti21S Marciniak specimens is about $E_c=0.4$ mm, $E_i=0.5$ mm and $E_m=0.8$ mm. Despite this, such modification can reduce the force needed to complete the whole Marciniak test and do not have other bad effects on the tests.

Marciniak specimens corresponding to uniaxial ($W=10$ mm), plane strain ($W=52$ mm) and equibiaxial ($W=100$ mm) strain paths are performed. All the specimens undergo a solution treatment at 900°C for 30 min, which is the same heat treatment of tensile specimens Ti21S 0. The Marciniak test device is the same as in Figure 4.1 with the only modification of the fillet radius of blank holder to 10 mm. The test procedure and parameters are the same as stated in section 4.2.1. Six specimens are tested in each strain condition (u: uniaxial, p: plane strain, b: equibiaxial). The results of new modified specimens are shown in Figure 4.24. From this figure, only two specimens in plane strain did not fractured. The others are well deformed and fractured. The limited area of the clamping provided limited friction to prevent the specimen from sliding in the blank holder. The force on this high-strength titanium alloy is very high and the fixing axis is ruptured. The sliding reduced the stress in the specimens so that some specimens in plane strain are not fractured.

4.4.2 Difficulty of detecting the forming limit

The method of detecting the forming limit of the Marciniak is ISO 12004-2 is the same as detecting the experimental forming limit point from the tensile test in Chapter 2. The distributions of major strain in one section of each specimen are identified just before the rupture. But there is problem on fitting with the inverse

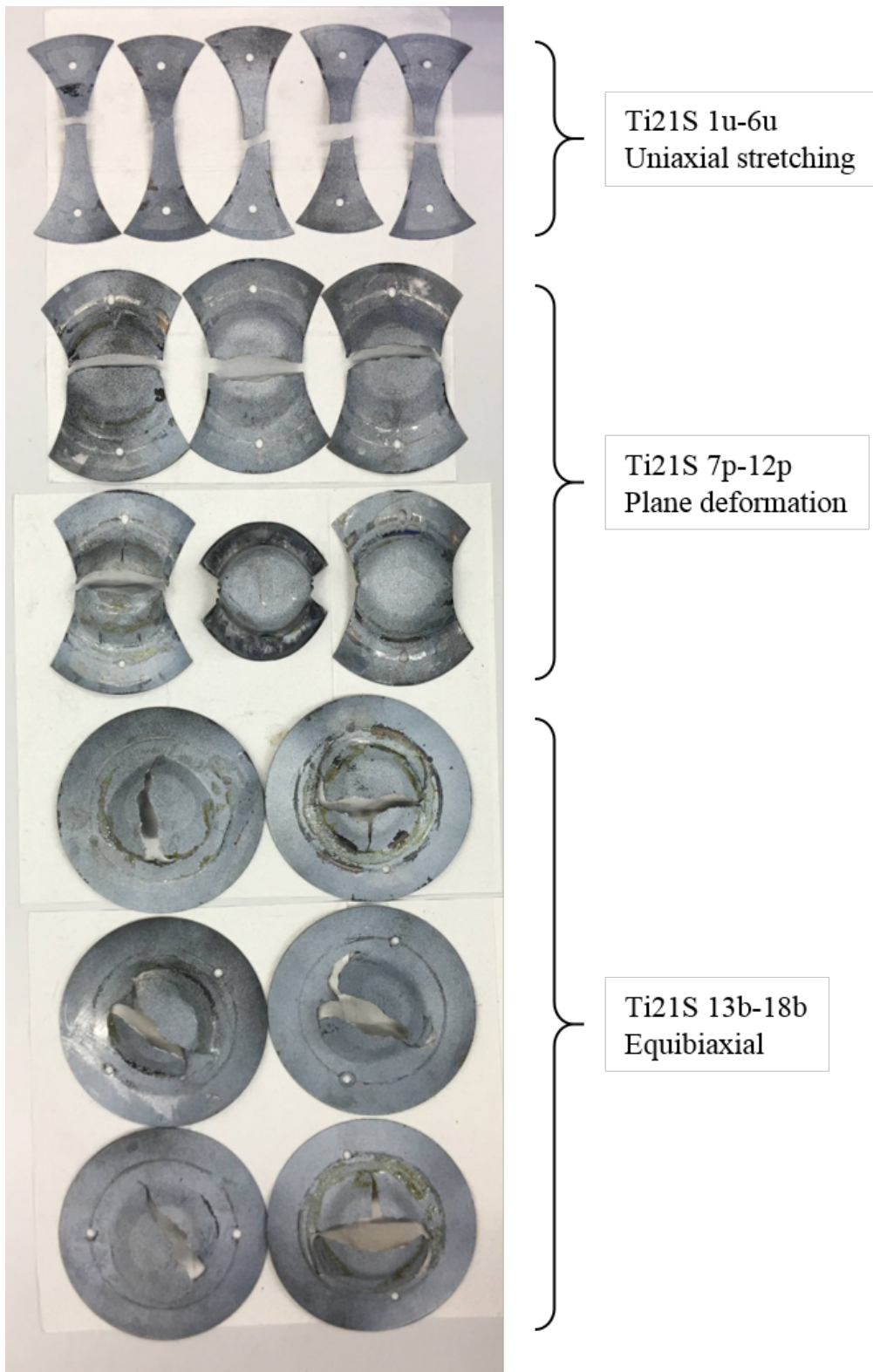
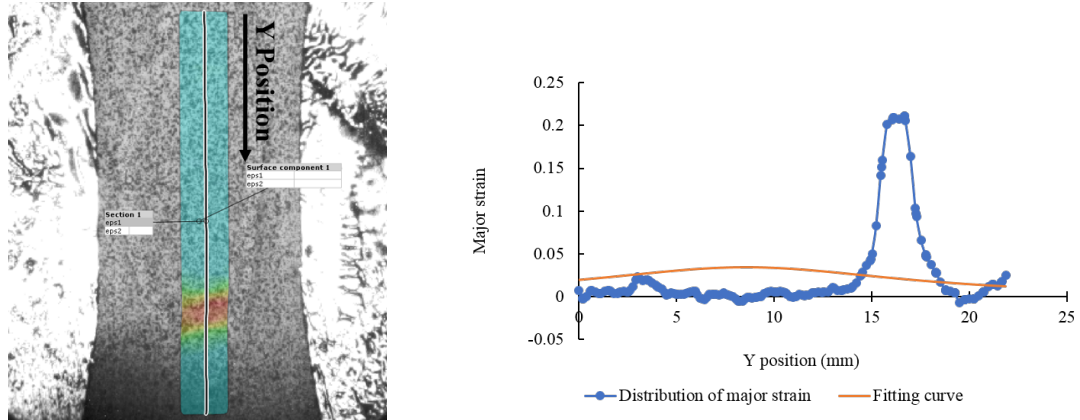


Figure 4.24: Marciniak specimens of Ti21S

parabola $f(x) = 1/(ax^2 + bx + c)$. Figure 4.25 shows the section and the fitting on the Marciniak specimen 3u as an example.



(a) Section of the Marciniak specimen 3u

(b) Distribution of major strain along the section and its fitting curve on the specimen 3u

Figure 4.25: Section and the fitting on the Marciniak specimen 3u

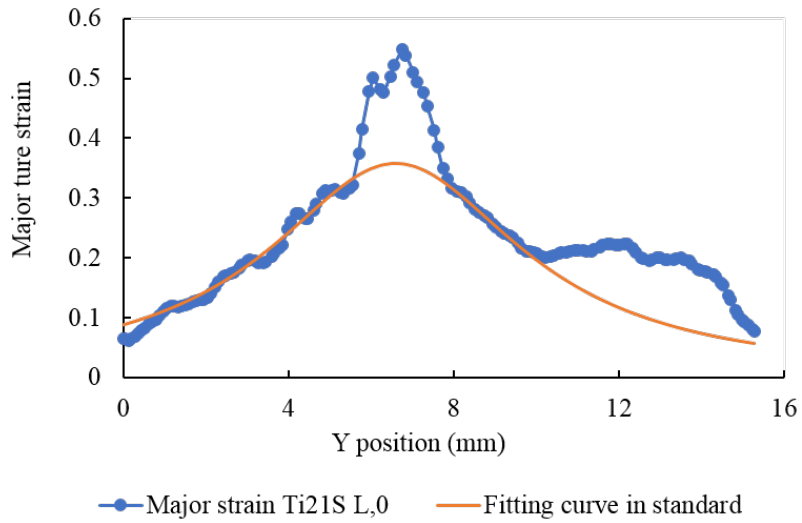
The studies on the fitting method found that the problem is due to the inverse parabola function $f(x) = 1/(ax^2 + bx + c)$ used in the fitting. When the specimen underwent adequate plastic deformation throughout the section before necking, as in aluminium for example, a high level of strain can be found along the section. At this moment, the fitting has no problem correlating the fitting window and obtaining a reasonable forming limit (Figure 4.26 (a)). But when there is inadequate deformation along the section before necking, the fitting window is very narrow. The slope of the fitting window is then high, the distance of these two windows is far. The ideal fitting curve of the function presented in the standard can be seen in Figure 4.26 (b). To fit the strain distribution in this situation, the identified parameters a, b and c exceed the presupposed ranges. And the most important, precise forming limit can not be obtained from the fitting curve in this condition.

4.4.3 Modified fitting method

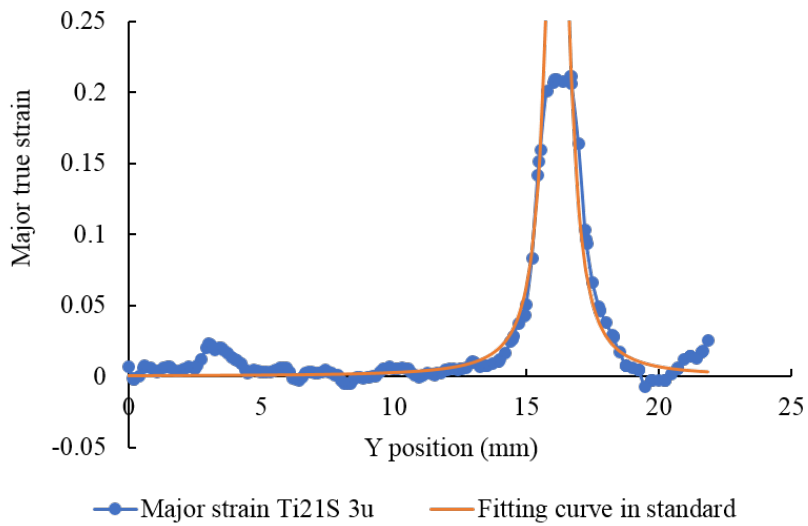
The function of fitting need to be modified to adapt to the new situation. A new parameter d is added at the end of the function. Equation 4.2 shows the modified function for the following fitting.

$$f(x) = \frac{1}{ax^2 + bx + c} + d \quad (4.2)$$

The new parameter d can be justified as the same method of a, b, c , which allows an offset up and down of the inverse parabola curve. It can neglect the effect of the level of strain throughout the section. This function is especially suitable for



(a) Fitting with high level strain distribution



(b) Fitting with low level strain distribution

Figure 4.26: Comparison of the standard fitting curve fitted with the specimens which have high level strain distribution and low level strain distribution along the section

detecting the forming limit of materials with low plasticity. The fitting of the Marciniak specimen 3u with the modified method shows great success (Figure 4.27).

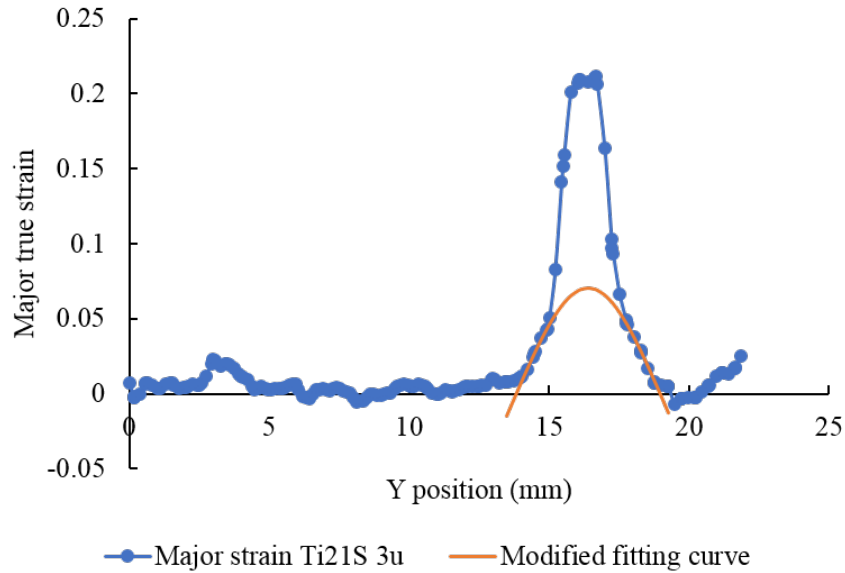


Figure 4.27: Distribution of major strain after Marciniak test (specimen 3u) and its fitting curve with the modified method

4.4.4 Results of Ti21S

The experimental points of all the Marciniak specimens are detected with the modified fitting method (Figure 4.28). The predicted curve from the tensile test of Ti21S L,0 in Figure 3.15 is added in Figure 4.29.

The points of Marciniak test of uniaxial specimens are very close to the predicted curve. But the limit strain is very low and the points are gathered close to the plane strain. The point from the tensile test of T21S L,0 has a huge difference of strain level from the Marciniak test uniaxial specimen (Figure 4.30).

The points of Marciniak test of plane strain have relatively higher limit strain than other conditions. The highest limit major strain is specimen 7p which reaches 0.17 (Figure 4.31). It is much higher than the predicted value of 0.02 at plane strain. The strain path is not exactly the plane strain. It has a deviation to the uniaxial part.

The points of Marciniak test of equibiaxial specimens have a higher forming limit than the predicted curve (Figure 4.32). The dimensions of these specimens are expected to realize the equibiaxial tension. But the results show that the strain path of equibiaxial specimens is nonlinear and they are separated from each other.

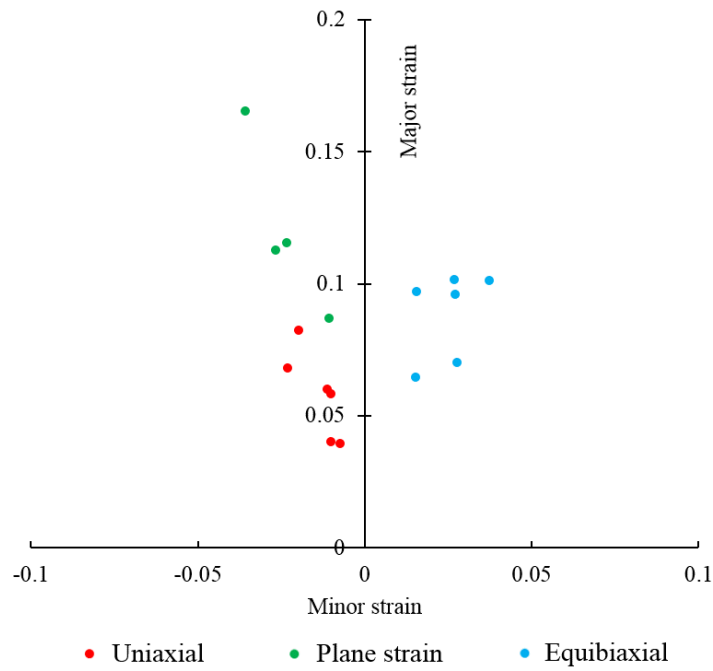


Figure 4.28: Marciniak test results of all experimental points on Ti21S

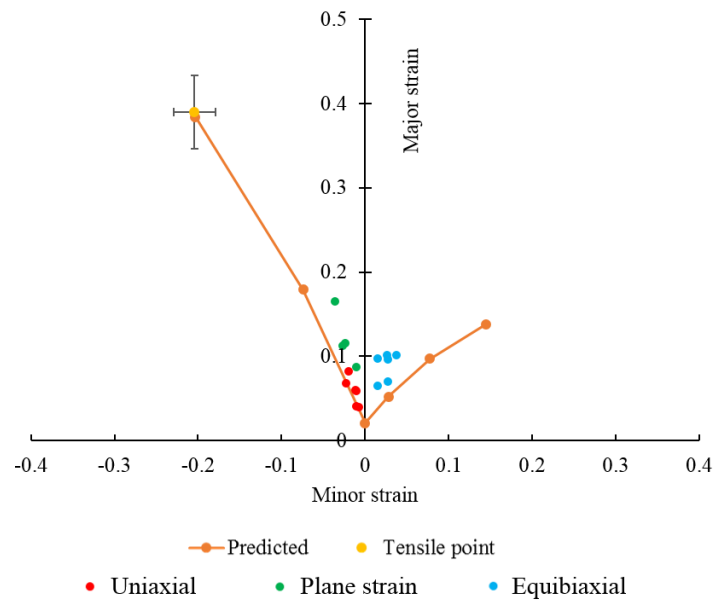


Figure 4.29: Comparison between the predicted FLC and all the points on Ti21S

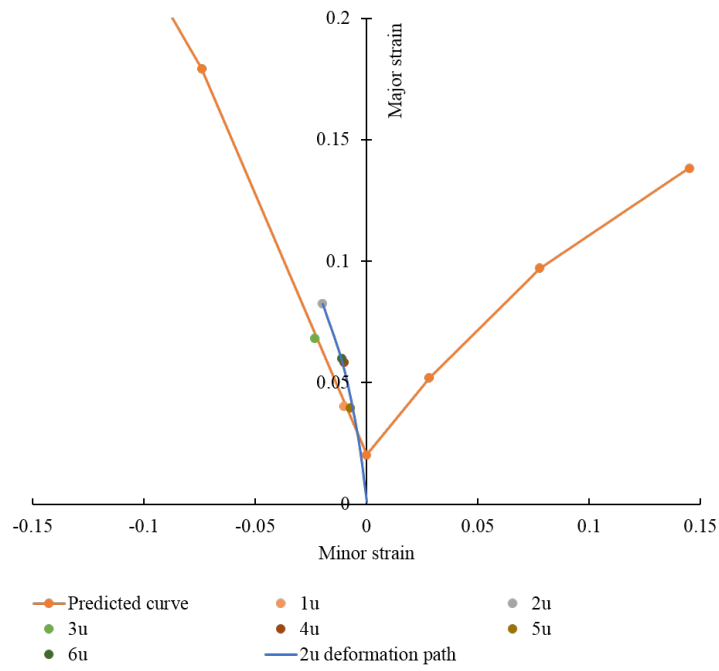


Figure 4.30: Marciniak test of Ti21S uniaxial specimen and its strain path

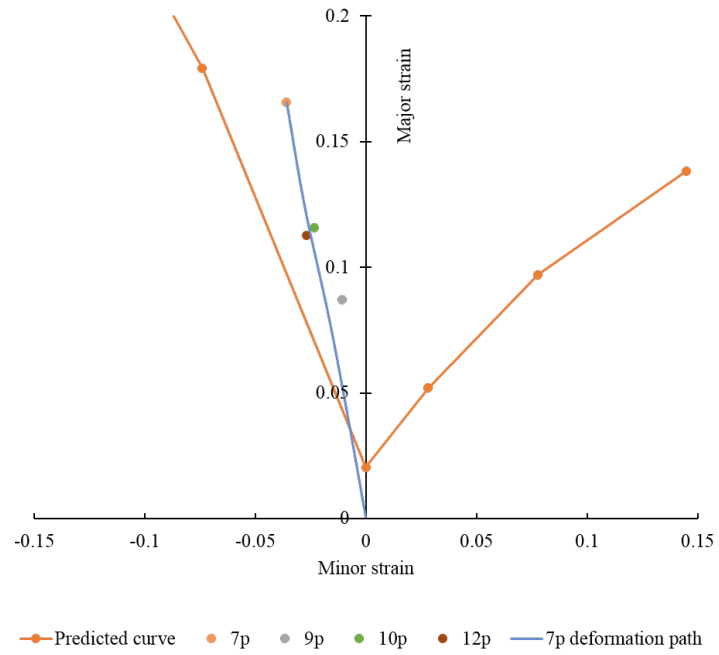


Figure 4.31: Marciniak test of Ti21S plane strain specimen and its strain path

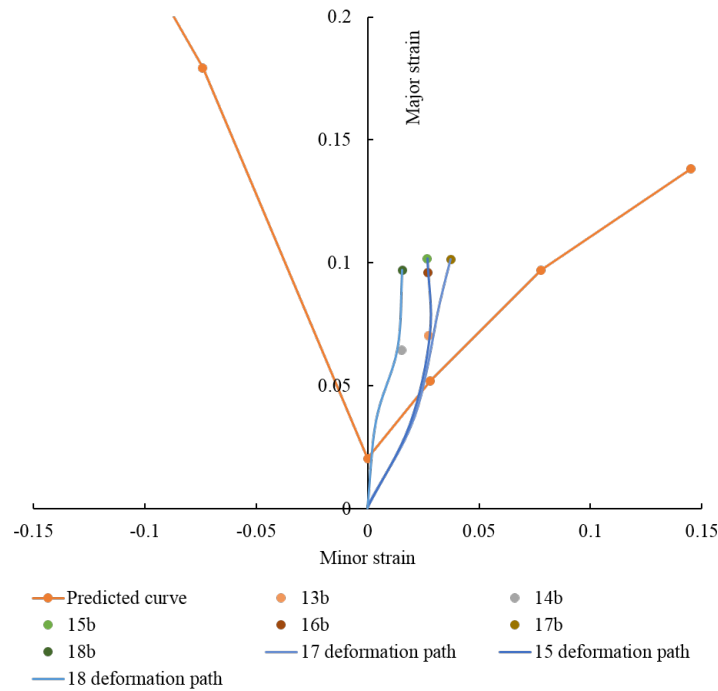


Figure 4.32: Marciniak test of Ti21S equibiaxial specimen and its strain path

4.4.5 Discussion and conclusions

The strain path of experimental points is very similar to the strain path in Figure 1.39 [145]. The points are located close to the plane strain of the predicted FLC and hard to reach ideal path of uniaxial stretching and equibiaxial stretching. The predicted FLC is plotted by the mean of the finite element M-K model calibrated on the point from uniaxial tensile test, but the Marciniak test results can not always cover all the possible strain paths on the predicted FLC.

The strain paths of all specimens are concentrated near the plane strain, making them hard to validate the uniaxial part and equibiaxial part of the predicted FLC. This phenomenon probably is due to the dimensions of Marciniak specimens. Even for the Marciniak uniaxial specimen, the thickness is 0.4 mm and the width is 10 mm. The ratio of the specimen thickness to width is $0.4/10=0.04$. The tension is homogeneous through this blank. The deformation mode is very similar to the plane strain. However, the uniaxial tensile specimen of Ti21S L,0 has a thickness of 0.8 mm and the width is 3 mm. The ratio of the specimen thickness to width ($0.8/3=0.27$) is larger than the Marciniak uniaxial specimen (0.04). This dimension has the advantage to have a strain component along the transverse direction.

The Marciniak specimens of Ti21S alloy show a localize plastic instability. The plastic deformation outside this small area is very low. This phenomenon is different from specimens for the uniaxial tensile test, which is also due to the dimension of the specimens. Despite these disadvantages, the experimental results

are slightly higher compared to the predicted FLC on plane strain. It can be concluded that the predicted FLC on the plane strain is conservative.

There are some strain paths of equibiaxial specimens which are not linear. Because the center part of the equibiaxial specimen is under a biaxial tension, the crack can be in any direction. Sometimes cracks in different directions occur simultaneously, which can be seen in the equibiaxial specimens after the Marciniak test in Figure 4.24. The main crack and sub cracks indicate that there is a competition of the necking in several directions. This may lead to a strain path in a non-linear condition.

All in all, the experimental points of Ti21S from Marciniak test have some discrepancies with the predicted FLC.

4.5 Conclusions

The optimization of the Marciniak test is conducted by simulation. The fillet radius of blank holder has the most evident influence on the Marciniak test. Enlarging this radius can significantly increase the possibility of cracking in the center part of the specimen. Modifying fillet radius of blank holder from 5 mm to 10 mm is adopted.

The formability of Ti21S alloy is characterized by Marciniak test. The experimental points are compared with the predicted FLC. These points are concentrated on the part of the plane strain of the curve. This method validates the predicted FLC of titanium alloys, even though the result is conservative on the plane strain.

It is difficult to validate the uniaxial part and equibiaxial part of the predicted FLC because the Marciniak specimens can not realize the ideal strain path due to their dimensions. This is due to different ratios of specimen thickness to width of the uniaxial tensile test specimen and Marciniak uniaxial specimen. The experimental points are gathered close to the area of plane deformation because the Marciniak specimens are very thin.

Thanks to this predicting method, detecting FLC will be simplified to a tensile test and several finite element simulations, which makes this procedure more economic and convenient.

Conclusions et Perspectives

L'objectif de ce travail est d'étudier l'effet de la microstructure sur la formabilité des alliages de titane. Pour cela, différentes microstructures d'alliages Ti21S et Ti5553 ont été caractérisées et les CLFs ont été tracées par un modèle prédictif ainsi que par l'expérimentation.

À partir d'une campagne expérimentale d'essais de traction, les propriétés mécaniques et la formabilité pour un chemin de déformation de traction uniaxiale ont été obtenues. Les résultats de l'essai de traction montrent que l'augmentation du taux de laminage, conduit à la réduction de la ductilité et la formabilité. La valeur r dans le sens de laminage est plus élevée que dans le sens transversal, ceci explique que les résistances à la traction dans le sens longitudinal sont plus élevées que celles dans le sens transversal. Ces observations peuvent être faites sur toutes les nuances testées à l'exception du Ti21S 75. Les alliages Ti5553 présentent une très faible formabilité, à l'exception du Ti5553 L,0. L'effet de la texture sur les propriétés mécaniques des alliages Ti21S et Ti5553 n'est pas évident. Mais on peut malgré tout conclure que le plan $\{1\ 1\ 2\}$ conduit à une meilleure formabilité tandis que le plan $\{1\ 1\ 0\}$ a un effet négatif sur la formabilité. Les fractographies du Ti21S et du Ti5553 illustrent les différences observées sur les propriétés mécaniques et sur les formabilités. Le mode de rupture fragile devient de plus en plus prépondérant avec l'augmentation du taux de laminage. La précipitation de la phase α conduit à une rupture à modes mixtes qui combine une rupture intergranulaire et une rupture ductile.

Après cette partie expérimentale, un modèle numérique M-K a été mis en place pour prédire les CLFs des alliages Ti21S et Ti5553. La loi d'érouissage de Ludwik a été calibrée pour chaque condition. Les paramètres du critère Hill48 ont été déterminés pour la condition Ti21S 0. Les résultats montrent que l'anisotropie a une influence significative sur les CLF prédites. La précipitation de la phase α après vieillissement conduit à une faible formabilité sur l'alliage Ti21S. On constate que les plus faibles valeurs de défaut f_0 sont calibrées pour le Ti21S 50 et le Ti21S

75. Le taux de laminage a un effet évident sur les limites de formabilité en traction uniaxiale des alliages Ti21S mais un effet moins évident sur les autres chemins de déformation. Contrairement au Ti21S, l'alliage Ti5553 a une très faible formabilité en général, ce qui peut s'expliquer par la plus grande taille de grain et sa plus grande intensité de texture.

Enfin, des tests Marciniak ont été réalisés sur Ti21S. La méthode de calcul des limites de formabilité a été adaptée aux alliages de titane caractérisés par un faible niveau de déformation plastique en dehors de la zone d'instabilité plastique localisée. Les résultats des tests de Marciniak montrent quelques divergences avec la CLF prédite pour le Ti21S. Le modèle prédictif est conservateur pour le chemin de déformation plane.

Malgré ces avancées, plusieurs perspectives peuvent être envisagées pour la suite de cette étude:

1. La caractérisation de la texture des alliages de titane β métastables pourrait être améliorée par la méthode DRX afin d'obtenir une information sur une plus grande échelle.

2. Le dispositif de Marciniak pourrait être redimensionné afin de tester des éprouvettes plus épaisses, ce qui permettrait d'être moins sensible aux dimensions de l'éprouvette (à l'épaisseur notamment) et de réaliser une campagne plus complète en terme de chemins de déformation.

3. Ce travail n'a considéré que la formabilité des alliages de titane β métastables à température ambiante. Il serait intéressant d'évaluer leur formabilité en fonction de la température.

4. Une caractérisation plus complète de l'anisotropie de ces alliages et un critère d'anisotropie plus approprié devraient être envisagés et être mis en œuvre dans le modèle prédictif.

Conclusions and Perspectives

The object of this work is to study the effect of the microstructure on the formability of titanium alloys. For this purpose, different microstructures of Ti21S and Ti5553 alloys have been characterized and FLCs have been plotted by a predictive model as well as by experiment.

From an experimental campaign of tensile tests, the mechanical properties and the formability for the uniaxial strain path of Ti21S and Ti5553 alloys have been obtained. According to the results of the tensile test, with the increase of the rolling reduction rates, ductility and formability are all decreased. r -value in rolling direction is higher than in transverse direction, this explains that tensile strength along the longitudinal direction is higher than those along the transverse direction. These phenomenons are concluded with an exception of Ti21S 75. The Ti5553 alloys show very low formability, except Ti5553 L,0. The effect of texture on the mechanical properties of Ti21S and Ti5553 alloys is not evident. But it still can be concluded that the $\{112\}$ //sheet plane leads to a better formability while the $\{110\}$ //sheet plane has a bad effect on the formability. The fractograph of Ti21S and Ti5553 illustrates the observed differences in mechanical properties and formability. Brittle fracture mode becomes more and more significant with the increasing of the rolling reduction rate. Precipitation of α phase leads to mixed-mode fracture which combined intergranular fracture and ductile fracture.

After this experimental part, a numerical M-K model has been built to predict FLCs of Ti21S and Ti5553 alloys. Ludwik's hardening law has been calibrated for each condition. Parameters of Hill48 criterion have been determined for condition Ti21S 0. Results show that anisotropy has a significant influence on the predicted FLCs. The precipitation of α phase after aging leads to low formability for the Ti21S alloy. It is shown that the smaller f_0 is calibrated for Ti21S 50 and Ti21S 75. The rolling reduction rate has an evident effect on the uniaxial stretching condition of Ti21S alloys but a less evident effect on other strain paths. Unlike Ti21S, Ti5553 alloy has very low formability in general, which can be explained

by its larger grain size and higher texture intensity.

Finally, Marciniak tests have been performed on Ti21S. Standard method for calculating forming limits has been adapted to titanium alloys characterized by a low level of plastic strain outside of the area of localized plastic instability. Results of Marciniak tests show some discrepancies with the predicted FLC of Ti21S which is slightly conservative for the plane strain path.

Despite this progress, there are still several perspectives that can be envisaged for this study:

1. The characterization of texture of metastable β titanium alloys can be optimized by XRD method to obtain the information of grains in a larger scale.
2. The capacity of Marciniak device can be improved to perform tests on the thicker specimens, which would permit to be less sensitive to the dimensions of the specimen and would allow to realize more complete strain paths.
3. This work only considered the formability of metastable β titanium alloys at room temperature. It would be interesting to evaluate their formability of different temperatures.
4. A more complete characterization of the anisotropy of these alloys and the calibration of a more suitable anisotropy criterion should be considered for implementation into the predictive model.

Appendix

The ODF of Ti21S and Ti5553

(*: texture components secondary important)

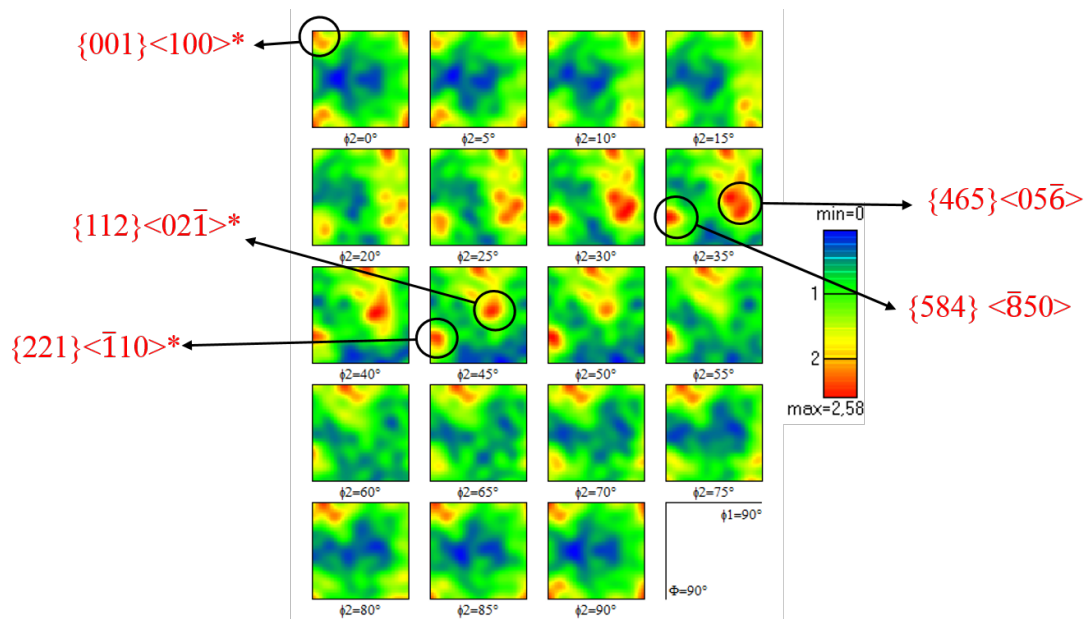


Figure 4.33: ODF of Ti21S 0

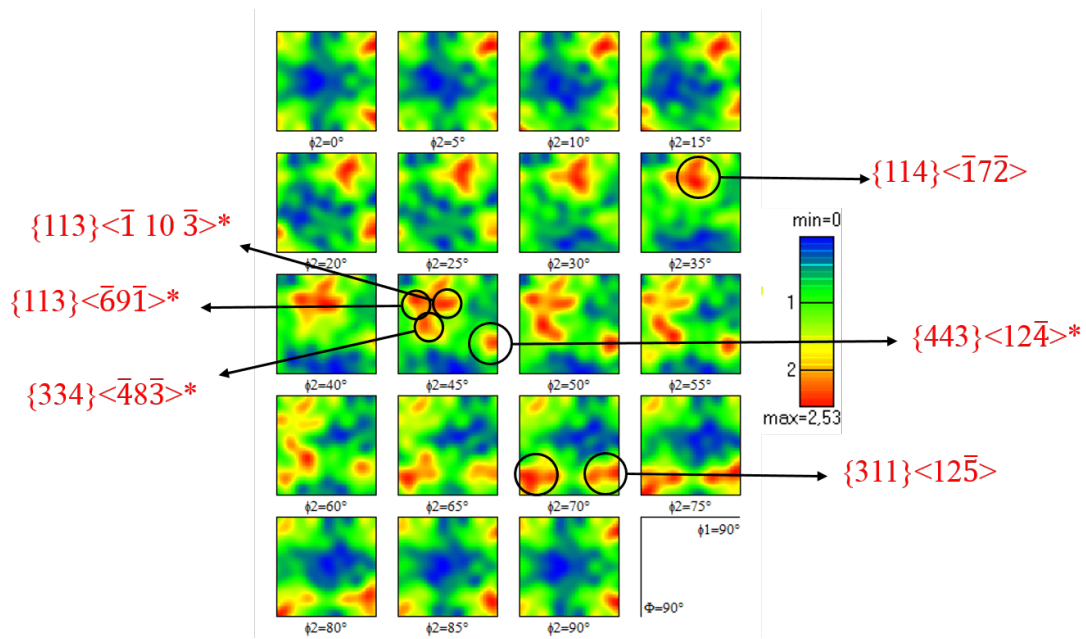


Figure 4.34: ODF of Ti21S 50

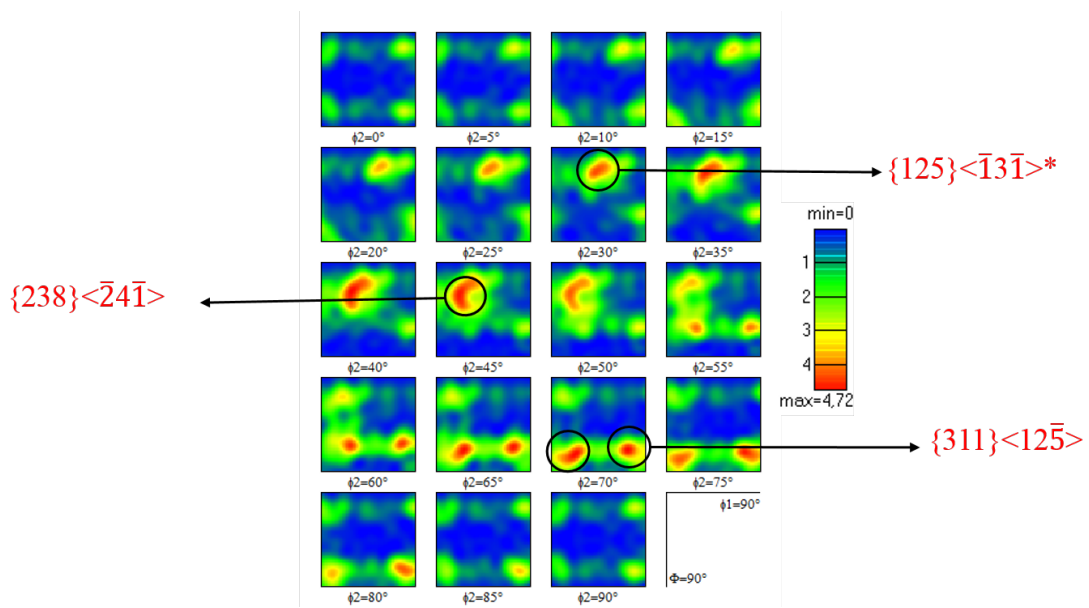


Figure 4.35: ODF of Ti21S 75

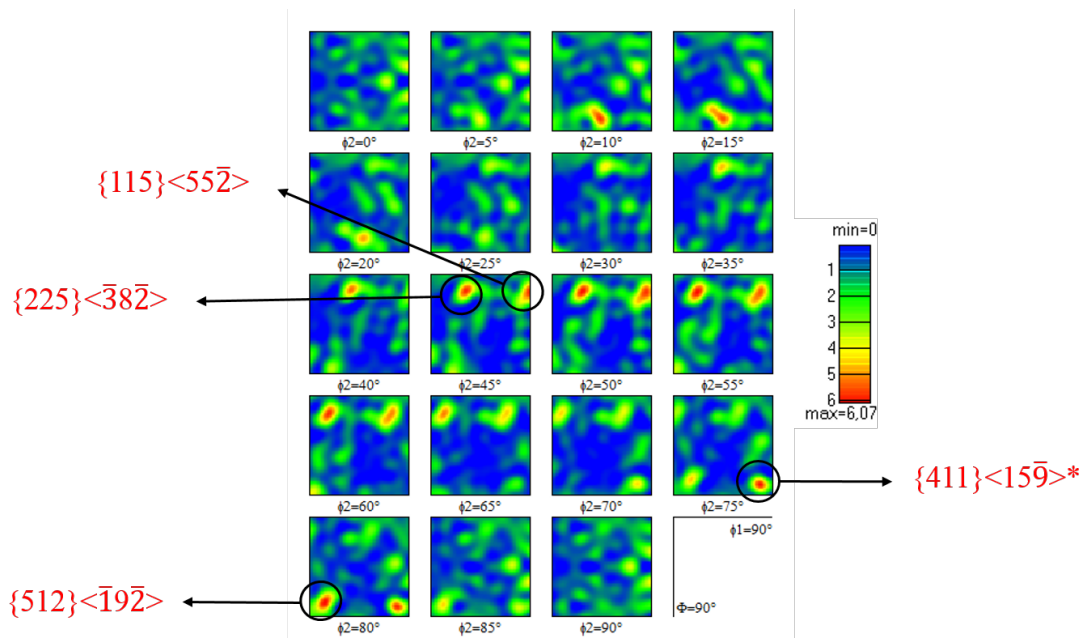


Figure 4.36: ODF of Ti5553 0

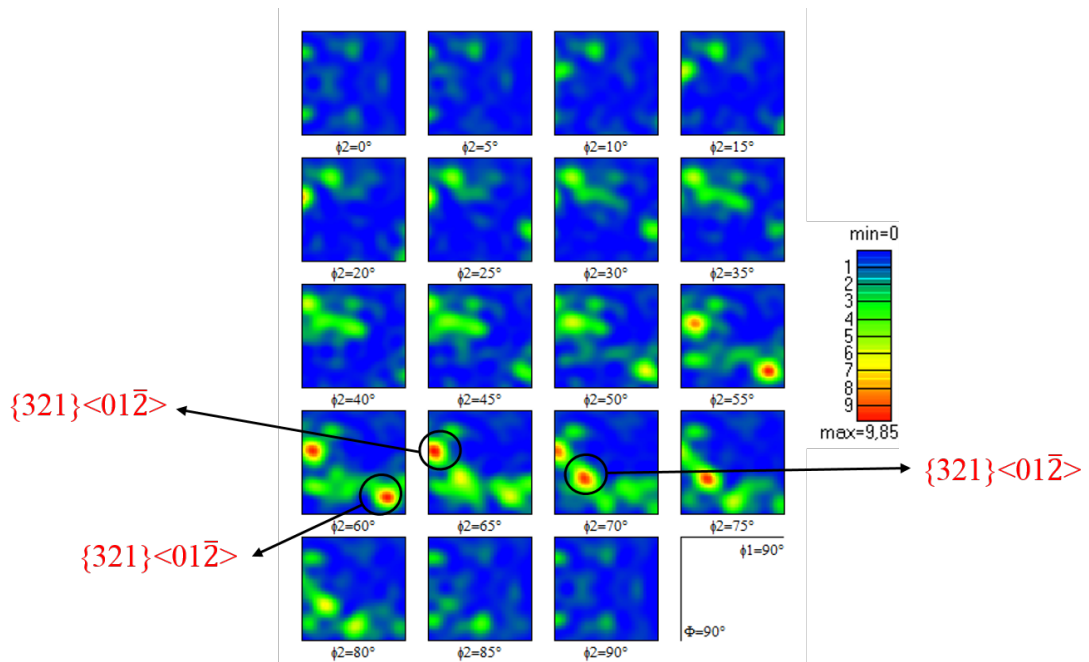


Figure 4.37: ODF of Ti5553 50

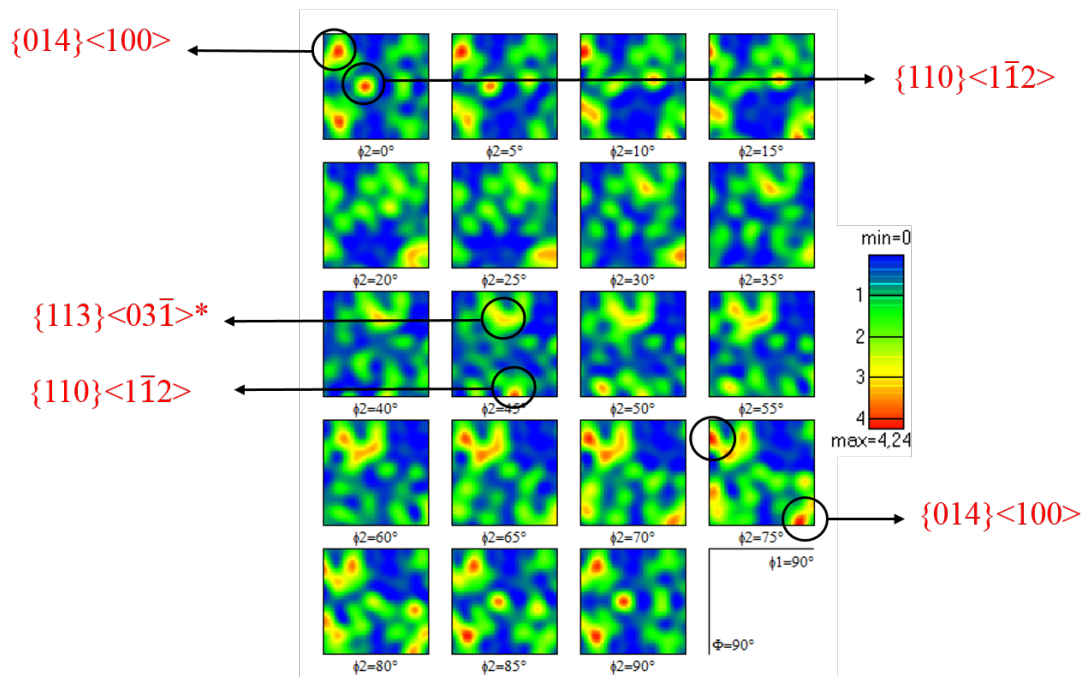


Figure 4.38: ODF of Ti5553 75

Bibliography

- [1] O. Schauerte, “Titanium in automotive production,” *Advanced Engineering Materials*, vol. 5, no. 6, pp. 411–418, 2003.
- [2] V. N. Moiseyev, *Titanium alloys: Russian aircraft and aerospace applications*. CRC press, 2005.
- [3] G. Tomchik and T. G. Dunder, “Overview of titanium applications on advanced commercial transports,” in *AeroMat Conference, unpublished research*, vol. 15, 2006.
- [4] I. Inagaki, T. Takechi, Y. Shirai, and N. Ariyasu, “Application and features of titanium for the aerospace industry,” *Nippon Steel & Sumitomo Metal Technical Report*, vol. 106, pp. 22–27, 2014.
- [5] R. A. Antunes, C. A. F. Salvador, and M. C. L. d. Oliveira, “Materials selection of optimized titanium alloys for aircraft applications,” *Materials Research*, vol. 21, no. 2, 2018.
- [6] G. Harruff, J. VanderVelden, W. Nelson, W. Spurr, and W. Quist, “Titanium 3Al-2.5V CW Hydraulic Tubing Development,” tech. rep., BOEING COMMERCIAL AIRPLANE CO SEATTLE WA, 1972.
- [7] J. C. Williams and R. R. Boyer, “Opportunities and issues in the application of titanium alloys for aerospace components,” *Metals*, vol. 10, no. 6, p. 705, 2020.
- [8] R. Boyer and R. Briggs, “The use of β titanium alloys in the aerospace industry,” *Journal of Materials Engineering and Performance*, vol. 14, no. 6, pp. 681–685, 2005.
- [9] R. R. Boyer, “Design properties of a high-strength titanium alloy, Ti-10V-2Fe-3Al,” *JOM*, vol. 32, no. 3, pp. 61–65, 1980.
- [10] C. Leyens and M. Peters, *Titanium and titanium alloys: fundamentals and applications*. John Wiley & Sons, 2003.

-
- [11] P. Jerome, “Advanced materials and technology for A380 structure,” *FAST Magazine*, vol. 32, no. 6, pp. 3–8, 2003.
- [12] F. Froes, *Titanium: physical metallurgy, processing, and applications*. ASM international, 2015.
- [13] T. RMI, “Titanium alloy guide,” *An RTI International Metals, New Jersey, USA*, 2000.
- [14] J. D. Beal, R. Boyer, and D. Sanders, “Forming of titanium and titanium alloys,” *Metalworking: Sheet Forming(ASM Handbook)*, vol. 14, pp. 656–669, 2006.
- [15] F. Froes and H. Bomberger, “The beta titanium alloys,” *JOM*, vol. 37, no. 7, pp. 28–37, 1985.
- [16] V. A. Joshi, *Titanium alloys: an atlas of structures and fracture features*. Crc Press, 2006.
- [17] K. K. Sankaran and R. S. Mishra, *Metallurgy and Design of Alloys with Hierarchical Microstructures*. Elsevier, 2017.
- [18] O. Ivasishin, P. Markovsky, S. Semiatin, and C. Ward, “Aging response of coarse-and fine-grained β titanium alloys,” *Materials Science and Engineering: A*, vol. 405, no. 1-2, pp. 296–305, 2005.
- [19] I. Weiss and S. Semiatin, “Thermomechanical processing of beta titanium alloys—an overview,” *Materials Science and Engineering: A*, vol. 243, no. 1-2, pp. 46–65, 1998.
- [20] S. Mantri, D. Choudhuri, A. Behera, J. Cotton, N. Kumar, and R. Banerjee, “Influence of fine-scale alpha precipitation on the mechanical properties of the beta titanium alloy beta-21S,” *Metallurgical and Materials Transactions A*, vol. 46, no. 7, pp. 2803–2808, 2015.
- [21] R. R. Boyer, “Aerospace applications of beta titanium alloys,” *JOM*, vol. 46, no. 7, pp. 20–23, 1994.
- [22] J. Fanning, “Military applications for β titanium alloys,” *Journal of materials engineering and performance*, vol. 14, no. 6, pp. 686–690, 2005.
- [23] J. D. Cotton, R. D. Briggs, R. R. Boyer, S. Tamirisakandala, P. Russo, N. Shchetnikov, and J. C. Fanning, “State of the art in beta titanium alloys for airframe applications,” *Jom*, vol. 67, no. 6, pp. 1281–1303, 2015.

- [24] T. Ahmed, M. Long, J. Silvestri, C. Ruiz, and H. Rack, "Titanium 95: Science and Technology," *The Institute of Materials, London*, pp. 1760–1767, 1996.
- [25] S. Malinov, W. Sha, and P. Markovsky, "Experimental study and computer modelling of the $\beta \rightarrow \alpha + \beta$ phase transformation in β 21S alloy at isothermal conditions," *Journal of alloys and compounds*, vol. 348, no. 1-2, pp. 110–118, 2003.
- [26] G. Lütjering and J. C. Williams, *Titanium*. Springer Science & Business Media, 2007.
- [27] Z. Zhishou, Z. Ming, C. Junpeng, W. Qingru, Q. Guiyi, and W. Weiqi, "Heat Treatment and Cold Forming Properties of beta-21S Titanium Sheet," *Rare Metal Materials and Engineering*, vol. 29, no. 1; ISSU 180, pp. 50–52, 2000.
- [28] H. Vigié, A. Soula, and B. Viguier, "Aging of the β 21S Titanium Alloy," in *Solid State Phenomena*, vol. 258, pp. 550–553, Trans Tech Publ, 2017.
- [29] J. Fanning, "Properties of TIMETAL 555 (Ti-5Al-5Mo-5V-3Cr-0.6Fe)," *Journal of Materials Engineering and Performance*, vol. 14, no. 6, pp. 788–791, 2005.
- [30] N. Jones, R. Dashwood, M. Jackson, and D. Dye, " β Phase decomposition in Ti-5Al-5Mo-5V-3Cr," *Acta Materialia*, vol. 57, no. 13, pp. 3830–3839, 2009.
- [31] V. Shevel'kov, "Structural conversions in VT22 titanium alloy during aging," *Metal science and heat treatment*, vol. 34, no. 8, pp. 534–539, 1992.
- [32] J. D. Cotton, R. R. Boyer, R. D. Briggs, R. G. Baggerly, C. A. Meyer, M. D. Carter, W. Wood, G. Tewksbury, V. Li, and X. Yao, "Phase transformations in Ti-5Al-5Mo-5V-3Cr-0.5Fe," *Proceedings of Ti-2007 Science and Technology, The Japan Institute of Metals*, 2007.
- [33] T. Duerig and J. Williams, "Overview: microstructure and properties of beta titanium alloys," *Beta Titanium Alloys in the 1980's*, pp. 19–67, 1983.
- [34] N. Jones, R. Dashwood, D. Dye, and M. Jackson, "Thermomechanical processing of Ti-5Al-5Mo-5V-3Cr," *Materials Science and Engineering: A*, vol. 490, no. 1-2, pp. 369–377, 2008.
- [35] A. Gerday, "Mechanical behavior of Ti-5553 alloy. Modeling of representative cells," *PhD thesis of University of Liège*, 2009.

- [36] W. Burgers, "On the process of transition of the cubic-body-centered modification into the hexagonal-close-packed modification of zirconium," *Physica*, vol. 1, no. 7-12, pp. 561–586, 1934.
- [37] J. Newkirk and A. Geisler, "Crystallographic aspects of the beta to alpha transformation in titanium," *Acta Met.*, vol. 1, 1953.
- [38] H.-J. Bunge, "Zur darstellung allgemeiner texturen," *Zeitschrift fur metallkunde*, vol. 56, no. 12, p. 872, 1965.
- [39] H. Bunge, "Three-dimensional texture analysis," *International Materials Reviews*, vol. 32, no. 1, pp. 265–291, 1987.
- [40] O. Engler and V. Randle, *Introduction to texture analysis: macrotexture, microtexture, and orientation mapping*. CRC press, 2009.
- [41] R. Ray, J. J. Jonas, and R. Hook, "Cold rolling and annealing textures in low carbon and extra low carbon steels," *International materials reviews*, vol. 39, no. 4, pp. 129–172, 1994.
- [42] H. Matsumoto, S. Watanabe, and S. Hanada, "Microstructures and mechanical properties of metastable β TiNbSn alloys cold rolled and heat treated," *Journal of alloys and compounds*, vol. 439, no. 1-2, pp. 146–155, 2007.
- [43] T. Inamura, Y. Fukui, H. Hosoda, K. Wakashima, and S. Miyazaki, "Pseudoelastic properties of cold-rolled TiNbAl alloy," in *Materials Science Forum*, vol. 475, pp. 2323–2328, Trans Tech Publ, 2005.
- [44] E. Fisher and D. Dever, "Relation of the c' elastic modulus to stability of bcc transition metals," *Acta metallurgica*, vol. 18, no. 2, pp. 265–269, 1970.
- [45] H. Inoue, S. Fukushima, and N. Inakazu, "Transformation textures in Ti–15V–3Cr–3Sn–3Al alloy sheets," *Materials Transactions, JIM*, vol. 33, no. 2, pp. 129–137, 1992.
- [46] D. Banerjee, A. L. Pilchak, and J. C. Williams, "Processing, structure, texture and microtexture in titanium alloys," in *Materials Science Forum*, vol. 710, pp. 66–84, Trans Tech Publ, 2012.
- [47] S. Suwas and R. K. Ray, *Crystallographic texture of materials*. Springer, 2014.
- [48] A. Singh, A. Bhattacharjee, and A. Gogia, "Microstructure and texture of rolled and annealed β titanium alloy Ti–10V–4.5 Fe–1.5 Al," *Materials Science and Engineering: A*, vol. 270, no. 2, pp. 225–230, 1999.

- [49] B. Sander and D. Raabe, “Texture inhomogeneity in a Ti–Nb-based β -titanium alloy after warm rolling and recrystallization,” *Materials Science and Engineering: A*, vol. 479, no. 1-2, pp. 236–247, 2008.
- [50] R. Sowerby and W. Johnson, “A review of texture and anisotropy in relation to metal forming,” *Materials Science and Engineering*, vol. 20, pp. 101–111, 1975.
- [51] S. Hémery and P. Villechaise, “Influence of β anisotropy on deformation processes operating in Ti-5Al-5Mo-5V-3Cr at room temperature,” *Acta Materialia*, vol. 141, pp. 285–293, 2017.
- [52] S. K. Jha, C. J. Szczepanski, R. John, and J. M. Larsen, “Deformation heterogeneities and their role in life-limiting fatigue failures in a two-phase titanium alloy,” *Acta Materialia*, vol. 82, pp. 378–395, 2015.
- [53] J.-Y. Kim, V. Yakovlev, and S. Rokhlin, “Line-focus acoustic microscopy of Ti-6242 α/β single colony: determination of elastic constants,” in *AIP Conference Proceedings*, vol. 615, pp. 1118–1125, American Institute of Physics, 2002.
- [54] S. Hémery and P. Villechaise, “Comparison of slip system activation in Ti-6Al-2Sn-4Zr-2Mo and Ti-6Al-2Sn-4Zr-6Mo under tensile, fatigue and dwell-fatigue loadings,” *Materials Science and Engineering: A*, vol. 697, pp. 177–183, 2017.
- [55] X. Zhang, Y. Mei, Y. Lv, C. Chen, and K. Zhou, “Anisotropy of the Microstructure and Tensile Properties in Ti-5Al-5Mo-5V-1Cr-1Fe near β Titanium Alloy during Hot Rolling and Heat Treatment,” *Metals*, vol. 8, no. 11, p. 904, 2018.
- [56] H. Hosoda, Y. Kinoshita, Y. Fukui, T. Inamura, K. Wakashima, H. Kim, and S. Miyazaki, “Effects of short time heat treatment on superelastic properties of a Ti–Nb–Al biomedical shape memory alloy,” *Materials Science and Engineering: A*, vol. 438, pp. 870–874, 2006.
- [57] S. Lhadi, M.-R. Chini, T. Richeton, N. Gey, L. Germain, and S. Berbenni, “Micromechanical Modeling of the Elasto-Viscoplastic Behavior and Incompatibility Stresses of β -Ti Alloys,” *Materials*, vol. 11, no. 7, p. 1227, 2018.
- [58] Q. Zhao, F. Yang, R. Torrens, and L. Bolzoni, “PM versus IM Ti-5Al-5V-5Mo-3Cr Alloy in Mechanical Properties and Fracture Behaviour,” *Materials Research*, vol. 22, 2019.

- [59] K. Mills and J. R. Davis, *ASM Handbook, Volume 12-Fractography*. ASM International, 1987.
- [60] G. Terlinde, T. Duerig, and J. Williams, “Microstructure, tensile deformation, and fracture in aged Ti-10V-2Fe-3Al,” *Metallurgical Transactions A*, vol. 14, no. 10, pp. 2101–2115, 1983.
- [61] C. Sauer and G. Lütjering, “Influence of α layers at β grain boundaries on mechanical properties of Ti-alloys,” *Materials Science and Engineering: A*, vol. 319, pp. 393–397, 2001.
- [62] Z. Du, S. Xiao, L. Xu, J. Tian, F. Kong, and Y. Chen, “Effect of heat treatment on microstructure and mechanical properties of a new β high strength titanium alloy,” *Materials & Design*, vol. 55, pp. 183–190, 2014.
- [63] R. Banoth, R. Sarkar, A. Bhattacharjee, T. Nandy, and G. N. Rao, “Effect of boron and carbon addition on microstructure and mechanical properties of metastable beta titanium alloys,” *Materials & Design*, vol. 67, pp. 50–63, 2015.
- [64] X. Shi, W. Zeng, S. Xue, and Z. Jia, “The crack initiation behavior and the fatigue limit of Ti-5Al-5Mo-5V-1Cr-1Fe titanium alloy with basket-weave microstructure,” *Journal of Alloys and Compounds*, vol. 631, pp. 340–349, 2015.
- [65] J. Huang, Z. Wang, and K. Xue, “Cyclic deformation response and micromechanisms of Ti alloy Ti-5Al-5V-5Mo-3Cr-0.5 Fe,” *Materials Science and Engineering: A*, vol. 528, no. 29-30, pp. 8723–8732, 2011.
- [66] C. Huang, Y. Zhao, S. Xin, C. Tan, W. Zhou, Q. Li, and W. Zeng, “Effect of microstructure on high cycle fatigue behavior of Ti-5Al-5Mo-5V-3Cr-1Zr titanium alloy,” *International Journal of Fatigue*, vol. 94, pp. 30–40, 2017.
- [67] G. Qiang, W. Qing, S. Dong-Li, H. Xiu-Li, and W. Gao-Hui, “Formation of nanostructure and mechanical properties of cold-rolled Ti-15V-3Sn-3Al-3Cr alloy,” *Materials Science and Engineering: A*, vol. 527, no. 16-17, pp. 4229–4232, 2010.
- [68] V. C. Opini, C. A. Salvador, K. N. Campo, E. S. Lopes, R. R. Chaves, and R. Caram, “ α phase precipitation and mechanical properties of Nb-modified Ti-5553 alloy,” *Materials Science and Engineering: A*, vol. 670, pp. 112–121, 2016.

- [69] A. Boyne, D. Wang, R. Shi, Y. Zheng, A. Behera, S. Nag, J. Tiley, H. Fraser, R. Banerjee, and Y. Wang, “Pseudospinodal mechanism for fine α/β microstructures in β -Ti alloys,” *Acta materialia*, vol. 64, pp. 188–197, 2014.
- [70] P. Barriobero-Vila, G. Requena, F. Warchomicka, A. Stark, N. Schell, and T. Buslaps, “Phase transformation kinetics during continuous heating of a β -quenched Ti–10V–2Fe–3Al alloy,” *Journal of materials science*, vol. 50, no. 3, pp. 1412–1426, 2015.
- [71] J. Sieniawski and W. Ziaja, *Titanium Alloys: Advances in Properties Control*. BoD–Books on Demand, 2013.
- [72] J. Williams, F. Froes, J. Chesnutt, C. Rhodes, and R. Berryman, “Toughness and fracture behavior of titanium,” *ASTM STP*, vol. 651, pp. 64–114, 1978.
- [73] O. Izumi and H. Kimura, *Titanium’80, Science and Technology: Proceedings of the Fourth International Conference on Titanium, Kyoto, Japan, May 19–22*. Metallurgical Society of AIME, 1980.
- [74] G. Lütjering, J. Williams, and A. Gysler, “Microstructure and mechanical properties of titanium alloys,” in *Microstructure And Properties Of Materials: (Volume 2)*, pp. 1–77, 2000.
- [75] W. F. Hosford and R. M. Caddell, *Metal forming: mechanics and metallurgy*. Cambridge university press, 2011.
- [76] F. J. Humphreys and M. Hatherly, *Recrystallization and related annealing phenomena*. Elsevier, 2012.
- [77] K. Chan and D. Koss, “Deformation and fracture of strongly textured ti alloy sheets in uniaxial tension,” *Metallurgical Transactions A*, vol. 14, no. 7, pp. 1333–1342, 1983.
- [78] R. Hill, “A theory of the yielding and plastic flow of anisotropic metals,” in *Proceedings of the Royal Society of London A: Mathematical, Physical and Engineering Sciences*, vol. 193, pp. 281–297, The Royal Society, 1948.
- [79] R. Hill, “The Mathematical Theory of Plasticity. Oxford University Press: London, 1950,”
- [80] R. Hill, “Theoretical plasticity of textured aggregates,” in *Mathematical Proceedings of the Cambridge Philosophical Society*, vol. 85, pp. 179–191, Cambridge University Press, 1979.

- [81] R. Hill, “Constitutive modelling of orthotropic plasticity in sheet metals,” *Journal of the Mechanics and Physics of Solids*, vol. 38, no. 3, pp. 405–417, 1990.
- [82] R. Hill, “A user-friendly theory of orthotropic plasticity in sheet metals,” *International Journal of Mechanical Sciences*, vol. 35, no. 1, pp. 19–25, 1993.
- [83] A.-F. Gerday, N. Clément, P. Jacques, T. Pardoen, and A. Habraken, “Finite element simulations of nanoindentation in beta metastable Ti alloys,” in *Proceedings of the 9th International ESAFORM Conference on Material Forming*, pp. 187–190, Akapit, 2006.
- [84] G. Gilles, O. Cazacu, W. Hammami, A. Habraken, and L. Duchene, “Experimental and numerical study of TA6V mechanical behavior in different monotonic loading conditions at room temperature,” *Procedia IUTAM*, vol. 3, pp. 100–114, 2012.
- [85] A. E. Wilson-Heid, S. Qin, and A. M. Beese, “Anisotropic multiaxial plasticity model for laser powder bed fusion additively manufactured Ti-6Al-4V,” *Materials Science and Engineering: A*, vol. 738, pp. 90–97, 2018.
- [86] D. Agius, C. Wallbrink, and K. I. Kourousis, “Efficient modelling of the elastoplastic anisotropy of additively manufactured Ti-6Al-4V,” *Additive Manufacturing*, vol. 38, p. 101826, 2021.
- [87] C. F. Guzmán, V. Tuninetti, G. Gilles, and A. M. Habraken, “Assessment of damage and anisotropic plasticity models to predict Ti-6Al-4V behavior,” in *Key Engineering Materials*, vol. 651, pp. 575–580, Trans Tech Publ, 2015.
- [88] G. Gilles, *Experimental study and modeling of the quasi-static mechanical behavior of Ti6Al4V at room temperature*. PhD thesis, Université de Liège, Liège, Belgique, 2015.
- [89] B. Revil-Baudard and E. Massoni, “Simulation du comportement mécanique des alliages de titane pour les procédés de mise en forme à froid de produits plats,” *Mécanique & industries*, vol. 11, no. 3-4, pp. 265–270, 2010.
- [90] M. Baral, “Experimental investigation of plastic anisotropy of commercially-pure titanium,” *Master thesis of University of New Hampshire*, 2015.
- [91] A. Bramley and P. Mellor, “Plastic anisotropy of titanium and zinc sheet—I,” *International Journal of Mechanical Sciences*, vol. 10, no. 3, pp. 211–219, 1968.

- [92] T. Yamashita, *Analysis of anisotropic material*. PhD thesis, Ohio University, 1996.
- [93] F. Barlat, J. Brem, J. W. Yoon, K. Chung, R. Dick, D. Lege, F. Pourboghrat, S.-H. Choi, and E. Chu, “Plane stress yield function for aluminum alloy sheets—part 1: theory,” *International Journal of Plasticity*, vol. 19, no. 9, pp. 1297–1319, 2003.
- [94] O. M. Badr, F. Barlat, B. Rolfe, M.-G. Lee, P. Hodgson, and M. Weiss, “Constitutive modelling of high strength titanium alloy Ti-6Al-4V for sheet forming applications at room temperature,” *International Journal of Solids and Structures*, vol. 80, pp. 334–347, 2016.
- [95] O. Cazacu, B. Plunkett, and F. Barlat, “Orthotropic yield criterion for hexagonal closed packed metals,” *International Journal of Plasticity*, vol. 22, no. 7, pp. 1171–1194, 2006.
- [96] B. Revil-Baudard and E. Massoni, “Simulation of the anisotropic behavior of titanium alloys during sheet metal forming,” *International Journal of Material Forming*, vol. 2, no. 1, pp. 73–76, 2009.
- [97] J. H. Hollomon, “Tensile deformation,” *Aime Trans*, vol. 12, no. 4, pp. 1–22, 1945.
- [98] H. Swift, “Plastic instability under plane stress,” *Journal of the Mechanics and Physics of Solids*, vol. 1, no. 1, pp. 1–18, 1952.
- [99] E. Voce, “The relationship between stress and strain for homogeneous deformation,” *Journal of the Institute of Metals*, vol. 74, pp. 537–562, 1948.
- [100] P. Ludwik, *Elemente der technologischen Mechanik*. Springer, 1909.
- [101] C. Hartley and R. Srinivasan, “Constitutive equations for large plastic deformation of metals,” *Journal of Engineering Materials and Technology*, vol. 105, no. 3, pp. 162–167, 1983.
- [102] D. Ludwigson, “Modified stress-strain relation for FCC metals and alloys,” *Metallurgical Transactions*, vol. 2, no. 10, pp. 2825–2828, 1971.
- [103] A. Bowen and P. Partridge, “Limitations of the Hollomon strain-hardening equation,” *Journal of Physics D: Applied Physics*, vol. 7, no. 7, p. 969, 1974.
- [104] J. V. Fernandes, D. M. Rodrigues, L. F. Menezes, and M. F. Vieira, “A modified Swift law for prestrained materials,” *International Journal of Plasticity*, vol. 14, no. 6, pp. 537–550, 1998.

- [105] T. dos Santos, P. A. Rosa, S. Maghous, and R. Rossi, “A simple isotropic hardening rule accounting for grain size effects in metal plasticity: modeling from coarse-grained to nanocrystalline materials,”
- [106] R. Harbaoui, O. Daghfes, A. Znaidi, and V. Tuninetti, “Mechanical behavior of materials with a compact hexagonal structure obtained by an advanced identification strategy of hcp material, az31b-h24,” *Frattura ed Integrità Strutturale*, vol. 14, no. 53, pp. 295–305, 2020.
- [107] H. Rym, D. Olfa, and Z. Amna, “Strategy for identification of HCP structure materials: study of Ti–6Al–4V under tensile and compressive load conditions,” *Archive of Applied Mechanics*, pp. 1–19, 2020.
- [108] K. Samuel, “Limitations of Hollomon and Ludwigson stress–strain relations in assessing the strain hardening parameters,” *Journal of Physics D: Applied Physics*, vol. 39, no. 1, p. 203, 2005.
- [109] X. Chu, *Caractérisation expérimentale et prédiction de la formabilité d’un alliage d’aluminium en fonction de la température et de la vitesse de déformation*. PhD thesis, 2013.
- [110] J. Lin, Y. Liu, and T. Dean, “A review on damage mechanisms, models and calibration methods under various deformation conditions,” *International Journal of damage mechanics*, vol. 14, no. 4, pp. 299–319, 2005.
- [111] T. Beier, G. Gula, S. Woestmann, and L. Keßler, “Eine bewertung des umformpotenzials von schnittkanten zur auslegung von formgebungsprozessen mit höherfesten stahlwerkstoffen,” in *Proceedings TB-040 35. EFB-Kolloquium Blechverarbeitung 2015 in Bad Boll*, pp. 139–150, 2015.
- [112] S. P. Keeler and W. A. Backofen, “Plastic instability and fracture in sheets stretched over rigid punches,” *Asm Trans Q*, vol. 56, no. 1, pp. 25–48, 1963.
- [113] J. Hu, Z. Marciniak, and J. Duncan, *Mechanics of sheet metal forming*. Elsevier, 2002.
- [114] M. Goodwin Gorton, “Application of strain analysis to sheet metal forming problems in the press shop,” *SAE Trans*, vol. 680093, pp. 380–387, 1968.
- [115] “Standard test method for determining forming limit curves,” *Astm*, 2008.
- [116] M. Abspoel, M. E. Scholting, and J. M. Droog, “A new method for predicting forming limit curves from mechanical properties,” *Journal of Materials Processing Technology*, vol. 213, no. 5, pp. 759–769, 2013.

- [117] K. Nakazima, T. Kikuma, and K. Hasuka, "Study on the formability of steel sheets," *YAWATA TECH REP, SEPT. 1968,-264-, 8517-8530*, 1968.
- [118] Z. Marciniak, K. Kuczyński, and T. Pokora, "Influence of the plastic properties of a material on the forming limit diagram for sheet metal in tension," *International Journal of Mechanical Sciences*, vol. 15, no. 10, pp. 789–800, 1973.
- [119] I. Standard *et al.*, "Metallic Materials—Sheet And Strip—Determination of Forming Limit Curves—Part 2: Determination of Forming Limit Curves in the Laboratory," *International Organization for Standardization*, vol. 20087, pp. 12004–2, 2008.
- [120] V. Hasek, "Untersuchung und theoretische beschreibung wichtiger einflußgrößen auf das grenzformänderungsschaubild," *Blech Rohre Profile*, vol. 25, no. 10, pp. 493–499, 1978.
- [121] M. Grumbach and G. Sanz, "Influence of various parameters on forming limit curves," *Revue de Metallurgie*, vol. 61, pp. 273–290, 1972.
- [122] T. Kikuma and K. Nakazima, "Effects of deforming conditions and mechanical properties on the stretch-forming limits of steel sheets," in *PROC INTERNAT CONF SCI TECHNOL IRON STEEL, TOKYO, 1971,-II-, 827-831*, 1971.
- [123] R. Bagheriasl, "Formability of aluminum alloy sheet at elevated temperature," *Ph.D thesis of University of Waterloo*, 2012.
- [124] D. Banabic, *Sheet metal forming processes: constitutive modelling and numerical simulation*. Springer Science & Business Media, 2010.
- [125] H. Takuda, K. Mori, and N. Hatta, "The application of some criteria for ductile fracture to the prediction of the forming limit of sheet metals," *Journal of Materials Processing Technology*, vol. 95, no. 1, pp. 116 – 121, 1999.
- [126] L. Wang and T. Lee, "The effect of yield criteria on the forming limit curve prediction and the deep drawing process simulation," *International Journal of Machine Tools and Manufacture*, vol. 46, no. 9, pp. 988 – 995, 2006.
- [127] T. Pepelnjak and K. Kuzman, "Numerical determination of the forming limit diagrams," *Journal of Achievements in Materials and Manufacturing Engineering*, vol. 20, no. 1-2, pp. 375–378, 2007.

-
- [128] Z. Marciniak and K. Kuczyński, “Limit strains in the processes of stretch-forming sheet metal,” *International Journal of Mechanical Sciences*, vol. 9, no. 9, pp. 609 – 620, 1967.
- [129] S. Keeler, “Determination of forming limits in automotive stampings. SAE Technical Paper 650535,” 1965.
- [130] S. Jones and P. Gillis, “A generalized quadratic flow law for sheet metals,” *Metallurgical Transactions A*, vol. 15, no. 1, pp. 129–132, 1984.
- [131] S. Jones and P. Gillis, “An analysis of biaxial stretching of a flat sheet,” *Metallurgical Transactions A*, vol. 15, no. 1, pp. 133–138, 1984.
- [132] S. Jones and P. P. Gillis, “A criterion for plastic instability,” in *Formability, analysis, modeling, and experimentation: proceedings of a symposium held in Chicago, Illinois, October 24 and 25, 1977*, p. 46, Metallurgical Society of AIME, 1978.
- [133] H. Pishbin and P. P. Gillis, “Forming limit diagrams calculated using Hill’s nonquadratic yield criterion,” *Metallurgical Transactions A*, vol. 23, no. 10, pp. 2817–2831, 1992.
- [134] J. Bressan and J. Williams, “The use of a shear instability criterion to predict local necking in sheet metal deformation,” *International Journal of Mechanical Sciences*, vol. 25, no. 3, pp. 155–168, 1983.
- [135] J. Bressan and J. Williams, “Limit strains in the sheet forming of strain and strain-rate sensitive materials,” *Journal of mechanical working technology*, vol. 11, no. 3, pp. 291–317, 1985.
- [136] S. Stören and J. Rice, “Localized necking in thin sheets,” *Journal of the Mechanics and Physics of Solids*, vol. 23, no. 6, pp. 421–441, 1975.
- [137] T. Kuwabara, M. Kuroda, V. Tvergaard, and K. Nomura, “Measurement of subsequent yield surface of prestrained sheet metal,” in *Plastic and Viscoplastic Response of Materials and Metal Forming (Eds.: Khan, AS et al.)*, pp. 531–533, NEAT Press, 2000.
- [138] D. Dudzinski and A. Molinari, “Perturbation analysis of thermoviscoplastic instabilities in biaxial loading,” *International Journal of Solids and Structures*, vol. 27, no. 5, pp. 601–628, 1991.

- [139] L. Toth, D. Dudzinski, and A. Molinari, “Forming limit predictions with the perturbation method using stress potential functions of polycrystal viscoplasticity,” *International journal of mechanical sciences*, vol. 38, no. 8-9, pp. 805–824, 1996.
- [140] P. Wu, K. Neale, E. Van der Giessen, M. Jain, S. MacEwen, and A. Makinde, “Crystal plasticity forming limit diagram analysis of rolled aluminum sheets,” *Metallurgical and Materials transactions A*, vol. 29, no. 2, pp. 527–535, 1998.
- [141] Z. Marciniak, “Stability of plastic shells under tension with kinematic boundary conditions (Stability of plastic shell under tension),” *Archiwum Mechaniki Stosowanej*, vol. 17, no. 4, pp. 577–592, 1965.
- [142] Q.-T. Pham, B.-H. Lee, K.-C. Park, and Y.-S. Kim, “Influence of the post-necking prediction of hardening law on the theoretical forming limit curve of aluminium sheets,” *International Journal of Mechanical Sciences*, vol. 140, pp. 521–536, 2018.
- [143] J. Hutchinson, K. Neale, and A. Needleman, “Mechanics of sheet metal forming,” *Sheet necking*, pp. 127–153, 1978.
- [144] B. Ma, X. Wu, X. Li, M. Wan, and Z. Cai, “Investigation on the hot formability of TA15 titanium alloy sheet,” *Materials & Design*, vol. 94, pp. 9–16, 2016.
- [145] B. S. Liu, W. Wu, and X. Q. Han, “Theoretical and experimental investigation on forming limit for tnw700 titanium alloy,” in *Key Engineering Materials*, vol. 622, pp. 340–346, Trans Tech Publ, 2014.
- [146] Q. T. Pham and Y. S. Kim, “Evaluation of press formability of pure titanium sheets,” in *Key Engineering Materials*, vol. 716, pp. 87–98, Trans Tech Publ, 2016.
- [147] X. Li, G. Guo, J. Xiao, N. Song, and D. Li, “Constitutive modeling and the effects of strain-rate and temperature on the formability of Ti–6Al–4V alloy sheet,” *Materials & Design*, vol. 55, pp. 325–334, 2014.
- [148] K. Narasimhan and R. Wagoner, “Finite element modeling simulation of in-plane forming limit diagrams of sheets containing finite defects,” *Metallurgical Transactions A*, vol. 22, no. 11, pp. 2655–2665, 1991.
- [149] C. Zhang, L. Leotoing, G. Zhao, D. Guines, and E. Ragneau, “A methodology for evaluating sheet formability combining the tensile test with the M-K

- model,” *Materials Science and Engineering: A*, vol. 528, no. 1, pp. 480–485, 2010.
- [150] W. Yuan, M. Wan, X. Wu, C. Cheng, Z. Cai, and B. Ma, “A numerical MK approach for predicting the forming limits of material AA5754-O,” *The International Journal of Advanced Manufacturing Technology*, vol. 98, no. 1, pp. 811–825, 2018.
- [151] F.-K. Chen and K.-H. Chiu, “Stamping formability of pure titanium sheets,” *Journal of materials processing technology*, vol. 170, no. 1-2, pp. 181–186, 2005.
- [152] R. Arrieux, C. Bedrin, and F. Le Maître, “Determination of forming limit diagrams for titanium sheets,” *CIRP Annals-Manufacturing Technology*, vol. 30, no. 1, pp. 189–192, 1981.
- [153] F. Djavanroodi and A. Derogar, “Experimental and numerical evaluation of forming limit diagram for Ti6Al4V titanium and Al6061-T6 aluminum alloys sheets,” *Materials & Design*, vol. 31, no. 10, pp. 4866–4875, 2010.
- [154] K. Chan and D. Koss, “Stretch forming and fracture of strongly textured Ti alloy sheets,” *Metallurgical Transactions A*, vol. 14, no. 7, pp. 1343–1348, 1983.
- [155] A. N. Chamos, G. N. Labeas, and D. Setsika, “Tensile behavior and formability evaluation of titanium-40 material based on the forming limit diagram approach,” *Journal of materials engineering and performance*, vol. 22, no. 8, pp. 2253–2260, 2013.
- [156] S. K. Paul, “Theoretical analysis of strain-and stress-based forming limit diagrams,” *The Journal of Strain Analysis for Engineering Design*, vol. 48, no. 3, pp. 177–188, 2013.
- [157] M. Sutton, W. Wolters, W. Peters, W. Ranson, and S. McNeill, “Determination of displacements using an improved digital correlation method,” *Image and vision computing*, vol. 1, no. 3, pp. 133–139, 1983.
- [158] T. J. Keating, P. Wolf, and F. Scarpace, “An improved method of digital image correlation,” *Photogrammetric Engineering and Remote Sensing*, vol. 41, no. 8, pp. 993–1002, 1975.
- [159] F. Sun, F. Prima, and T. Gloriant, “High-strength nanostructured Ti–12Mo alloy from ductile metastable beta state precursor,” *Materials Science and Engineering: A*, vol. 527, no. 16-17, pp. 4262–4269, 2010.

-
- [160] P. Wu, A. Graf, S. MacEwen, D. Lloyd, M. Jain, and K. Neale, “On forming limit stress diagram analysis,” *International Journal of Solids and Structures*, vol. 42, no. 8, pp. 2225–2241, 2005.
- [161] D. Banabic, S. Comsa, P. Jurco, G. Cosovici, L. Paraiianu, and D. Julean, “Fld theoretical model using a new anisotropic yield criterion,” *Journal of Materials Processing Technology*, vol. 157, pp. 23–27, 2004.
- [162] C. Zhang, *Etude de l’effect de la sensibilité à la vitesse de déformation sur la formabilité de tôle en alliage d’aluminium*. PhD thesis, PhD thesis, Institut National des Sciences Appliquées de Rennes, 2008. Conclusions and perspectives 161, 2008.
- [163] X. Chu, L. Leotoing, D. Guines, and E. Ragneau, “Temperature and strain rate influence on AA5086 Forming Limit Curves: Experimental results and discussion on the validity of the MK model,” *International Journal of Mechanical Sciences*, vol. 78, pp. 27–34, 2014.
- [164] J. Ding, C. Zhang, X. Chu, G. Zhao, L. Leotoing, and D. Guines, “Investigation of the influence of the initial groove angle in the M–K model on limit strains and forming limit curves,” *International Journal of Mechanical Sciences*, vol. 98, pp. 59–69, 2015.
- [165] C. Zhang, X. Chu, D. Guines, L. Leotoing, J. Ding, and G. Zhao, “Dedicated linear–Voce model and its application in investigating temperature and strain rate effects on sheet formability of aluminum alloys,” *Materials & Design*, vol. 67, pp. 522–530, 2015.

AVIS DU JURY SUR LA REPRODUCTION DE LA THESE SOUTENUE

Titre de la thèse:

Effect of microstructure on the formability of β titanium alloys

Nom Prénom de l'auteur : HU CAI

Membres du jury :

- Madame BALLAND Pascale
- Monsieur TANCRET Franck
- Monsieur LEOTOING Lionel
- Madame MÔREAU Laurence
- Monsieur LAURENT Hervé
- Monsieur CASTANY Philippe

Président du jury : *Hervé LAURENT*

Date de la soutenance : 23 Novembre 2021

Reproduction de la these soutenue

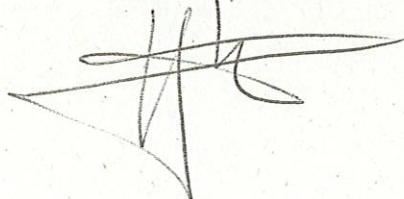
- Thèse pouvant être reproduite en l'état
 Thèse pouvant être reproduite après corrections suggérées

Fait à Rennes, le 23 Novembre 2021

Signature du président de jury

Le Directeur,

Pr. M'Hamed DRISSI



Titre : Effet de la microstructure sur la formabilité des alliages de titane β

Mots clés : Alliages de titane β métastables; microstructure; courbes limites de formage; modèle prédictif M-K

Résumé : Les alliages de titane sont très utilisés dans plusieurs secteurs industriels (aéronautique, biomédical, ...) en raison d'une résistance mécanique spécifique élevée, d'une très bonne résistance à la corrosion et de leurs performances à haute température. Les propriétés mécaniques telles que la ductilité ou encore la formabilité sont largement dépendantes de leur microstructure. Ce travail porte sur l'étude du comportement mécanique des alliages de titane β métastables de plus en plus utilisés dans les applications aéronautiques, en remplacement des alliages de titane $\alpha+\beta$. L'objectif est d'étudier l'influence de la microstructure, en particulier la texture, sur la formabilité de ces matériaux. Les alliages β métastables Ti21S et Ti5553 ont été sélectionnés.

Une caractérisation mécanique (écrouissage et formabilité) de différentes microstructures est tout d'abord effectuée à partir d'une campagne d'essais de traction uniaxiale. Les résultats obtenus montrent que le taux de laminage et la précipitation α affectent la formabilité. Un modèle numérique de type M-K est ensuite proposé afin de prédire des courbes limites de formage complètes pour les différentes microstructures étudiées. Une campagne expérimentale avec un dispositif de mise en forme de type Marciniak est enfin menée pour la nuance Ti21S afin de discuter le caractère prédictif du modèle proposé.

Title : Effect of microstructure on the formability of β titanium alloys

Keywords : Metastable β titanium alloys; microstructure; forming limit curves; predictive M-K model

Abstract: Titanium alloys are widely used in industries (aeronautics, biomedical ...) due to their high specific mechanical strength, very good corrosion resistance and high temperature performances. Mechanical properties such as ductility or formability are largely dependent on their microstructure. This work focuses on the study of the behaviour of β metastable titanium alloys increasingly used in aeronautical applications as a replacement for $\alpha+\beta$ titanium alloys. The objective is to study the influence of microstructure, in particular texture, on the formability of such materials. The metastable alloys Ti21S and Ti5553 are selected for this study.

First, a mechanical characterization (hardening and formability) of different microstructures is carried out thanks to a campaign of uniaxial tensile tests. The results show that both the rolling ratio and the α precipitation impact the formability. A numerical model based on the M-K theory is proposed for the prediction of the whole forming limit curves, for the different studied microstructures. Finally, an experimental campaign on a Marciniak-type set-up permits to follow various strain paths for the Ti21S grade and discuss the predictive character of the proposed model.